CHAPTER 1

Update on Ozone-Depleting Substances (ODSs) and Other Gases of Interest to the Montreal Protocol

About the cover image:
The Jungfraujoch research station in Switzerland is one of many observatories in the Advanced Global Atmospheric Gases Experiment (AGAGE) network from which scientists monitor changes in atmospheric composition that affect both ozone depletion and climate change.

Photo credit: Paedii Luchs via Stocksy

CHAPTER 1

Update on Ozone-Depleting Substances (ODSs) and Other Gases of Interest to the Montreal Protocol

Lead Authors : Johannes C. Laube
Susann Tegtmeier

Coauthors : Rafael P. Fernandez
Jeremy Harrison
Lei Hu
Paul Krummel
Emmanuel Mahieu
Sunyoung Park
Luke Western

Contributing Authors : Elliot Atlas
Peter Bernath
Carlos A. Cuevas
Geoff Dutton
Lucien Froidevaux
Ryan Hossaini
Timo Keber
Theodore K. Koenig
Stephen A. Montzka
Jens Mühle
Simon O'Doherty
David E. Oram
Klaus Pfeilsticker
Maxime Prignon
Birgit Quack
Matthew Rigby
Meike Rotermund
Takuya Saito
Isobel J. Simpson
Dan Smale
Martin K. Vollmer
Dickon Young

Review Editors : Andreas Engel
Bo Yao

CONTENTS

Chapter 1: Update on Ozone-Depleting Substances (ODSs) and Other Gases of Interest to the Montreal Protocol

SCIENTIFIC SUMMARY

This chapter concerns atmospheric changes in ozone-depleting substances (ODSs), such as chlorofluorocarbons (CFCs), halons, chlorinated solvents (e.g., carbon tetrachloride [CCl_4] and methyl chloroform [CH_3CCl_3]) and hydrochlorofluorocarbons (HCFCs), which are controlled under the Montreal Protocol. Furthermore, the chapter updates information about ODSs not controlled under the Protocol, such as methyl chloride (CH_3Cl) and very short-lived substances (VSLSs). In addition to depleting stratospheric ozone, many ODSs are potent greenhouse gases.

Mole fractions of ODSs and other species are primarily measured close to the surface by global or regional monitoring networks. The surface data can be used to approximate a mole fraction representative of the global or hemispheric tropospheric abundance. Changes in the tropospheric abundance of an ODS result from a difference between the rate of emissions into the atmosphere and the rate of removal from it.

- **The total amount of chlorine and bromine from ODSs that were controlled under the original Montreal Protocol is continuing to decline, as the overall emissions are smaller than the rate at which these ODSs are destroyed. Abundances of many of the first-stage replacement compounds, HCFCs, are now increasing very slowly or not at all.**

Tropospheric Chlorine (Cl)

Total tropospheric chlorine is a metric used to quantify the combined globally averaged abundance of chlorine in the troposphere due to the major chlorine-containing ODSs. The contribution of each ODS to total tropospheric chlorine is the product of its global mean tropospheric mole fraction and the number of chlorine atoms it contains.

- **Total tropospheric chlorine from ODSs continued to decrease between 2016 and 2020.** Total tropospheric chlorine in 2020 was 3220 ppt (where ppt refers to parts per trillion as a dry air mole fraction), about 1.8% lower than in 2016 and 12% lower than its peak value in 1993. Of the 2020 total, CFCs accounted for about 60%, CH_3Cl for about 17%, and CCl_4 and HCFCs each for about 10%. The contribution from CH_3CCl_3 has now decreased to 0.1%. Very short-lived source gases (VSL SGs), as measured in the lower troposphere, contributed approximately 3.5%.
    - During the period 2016–2020, the observed rate of decline in tropospheric chlorine due to controlled substances was 15.1 ± 2.4[1] ppt Cl yr^{-1}, which is larger than during the 2012–2016 period (12.8 ± 0.8 ppt Cl yr^{-1}). This rate of decrease was close to the projections in the previous Assessment. The net rate of change was the result of a slightly slower than projected decrease in CFCs and a slower HCFC increase than in the 2018 A1 projection scenario.
    - When substances not controlled under the Montreal Protocol are also included, the overall decrease in tropospheric chlorine was 15.1 ± 3.6 ppt Cl yr^{-1} during 2016–2020. This is larger than the rate of decline during the 2012–2016 period (3.6 ± 4.7 ppt Cl yr^{-1}) and comparable to the rate of decline in controlled substances. Changes in the predominantly anthropogenic dichloromethane (CH_2Cl_2) and the largely natural CH_3Cl largely canceled each other out, resulting in almost no net change in Cl from uncontrolled substances during this period.
- **Starting around 2018, the rate at which the CFC-11 mole fraction was declining in the atmosphere accelerated again, following a slowdown since 2013. These recent changes are largely due to a decrease in emissions originating mostly from northeastern China.** Assuming no impact from changes in atmospheric circulation, global emissions increased from about 57 Gg yr^{-1} (= kt yr^{-1}) in 2012 to around 78 Gg yr^{-1} in 2017; after 2018, they then decreased to approximately 47 Gg yr^{-1} in 2020. Emissions from northeastern China explain 60 ± 40% of the 2012–2018 increase and 60 ± 30% of the subsequent decrease. There is evidence that other recent significant emission regions include the Arabian and Indian subcontinents. If these renewed global emissions are associated with uses that substantially increase the size of the CFC-11 bank, further emissions resulting from this production would be expected in the future.
- **During 2016–2020, mole fractions of CFC-12 decreased by about 2.8%, which is comparable to the decrease during 2012–2016 (~2.3%).** Estimates of global CFC-12 emissions in 2016 and 2020 were similar within uncertainties, at 33 ± 21 Gg yr^{-1} and 25 ± 20 Gg yr^{-1}, respectively. CFC-11 and CFC-12 are often co-produced, and atmospheric observations have confirmed a decrease in CFC-12 emissions from northeastern China from 3.3 ± 1.4 Gg yr^{-1} in 2016 to 0.5 ± 0.5 Gg yr^{-1} in 2019.
- **The CFC-113 global mole fraction has continued to decrease**, but emissions remained constant within uncertainties at around 6 ± 6 Gg yr^{-1} between 2016 and 2020.
- **Mole fractions of CFC-114 remained stable during 2016–2020, whereas those of CFC-13, CFC-113a, and CFC-115 continued to rise, and mole fractions of CFC-112a and CFC-114a exhibited positive growth after previously showing near-zero change.** Total Cl from the latter five CFCs increased from 16.0 ± 0.3 ppt in 2016 to a total of 17.2 ± 0.3 ppt Cl in 2020. These findings likely indicate an increase

[1] Uncertainties in absolute changes of atmospheric abundances were derived using the 1 standard deviation measurement uncertainties (where appropriate combined as the square root of the sum of their squares) and the bootstrap algorithm described in Barreto and Howland (2006). Similar to the procedure described in Leedham Elvidge et al. (2018), and to represent atmospheric variability, data was converted to a dataset comprised of 1) original data, 2) original data minus measurement uncertainty and 3) original data plus measurement uncertainty. This dataset was then resampled (with replacement) 1000 times to derive a standard deviation that is a realistic representation of the uncertainty of the entirety of the original data.

or stabilization of the emissions of these relatively low abundance compounds. While some of these emissions are known to originate from eastern China, the primary processes responsible are unknown.

- **The rate at which CCl_4 has declined in the atmosphere remains slower than expected from its reported use as a feedstock and its removal rate from the atmosphere, which indicates ongoing emissions of around 44 ± 15 Gg yr^{-1}.** This is likely, at least in part, due to feedstock emissions from the production of chloromethanes and perchloroethylene and from chlor-alkali plants. Global CCl_4 emission estimates based on atmospheric observations are now more accurate than in the last Assessment due to an improved lifetime estimate.
- **Emissions of CCl_4 in eastern China over the period 2013–2019 show year-to-year variability likely related to CFC-11 production.** Emissions increased after 2013, reaching 11.3 ± 1.9 Gg yr^{-1} in 2016, and decreasing to 6.3 ± 1.1 Gg yr^{-1} in 2019.
- **Total tropospheric chlorine from HCFCs has continued to increase, reaching 320 ± 3 ppt in 2020.** There is evidence of a slowdown of this increase, as the annual average growth rate of total chlorine from HCFCs decreased from 5.9 ± 1.3 ppt Cl yr^{-1} during 2012–2016 to 2.5 ± 0.4 ppt Cl yr^{-1} during 2016–2020.
- **Combined emissions of the major HCFCs have declined since the previous Assessment.** Emissions of HCFC-22 and HCFC-142b likely declined between 2016 and 2020, while emissions of HCFC-141b, after an initial drop, likely rose year-on-year since 2017, amounting to a total rise of ~4.5 Gg during 2017–2020. These findings are consistent with a sharp drop in reported HCFC consumption after 2012, particularly from Article 5 countries.
- Continued emissions of the compounds HCFC-124, HCFC-31, HCFC-132b, and HCFC-133a have been inferred from atmospheric measurements. HCFC-132b is yet another newly detected HCFC, and its atmospheric mole fractions, while currently small, continue to increase.

Tropospheric Bromine (Br)

Total tropospheric bromine is defined in analogy to total tropospheric chlorine. Even though the abundance of bromine is much smaller than that of chlorine, it has a significant impact on stratospheric ozone because it is around 60–65 times more efficient than chlorine as an ozone-destroying catalyst.

- **Total tropospheric bromine from controlled ODSs (halons and methyl bromide [CH_3Br]) continued to decrease, and was 13.9 ppt by 2020, 3.2 ppt below the peak levels observed in 1999.** From 2012 to 2016, total controlled bromine declined at a rate of 0.15 ± 0.14 ppt Br yr^{-1} (about 1% yr^{-1}). This rate increased to 0.18 ± 0.05 ppt Br yr^{-1} during 2016–2020, with halons contributing about 60% to the overall decline.
- **The mole fractions of halon-1211, halon-2402, and halon-1202 continued to decline between 2016 and 2020. There was no significant change in the mole fraction of halon-1301 between 2016 and 2020. This ODS is, at ~3.3 ppt, now the most abundant halon in the atmosphere.** Emissions of halon-2402, halon-1301, and halon-1211, as derived from atmospheric observations, declined or remained stable between 2016 and 2020.
- **CH_3Br annually averaged mole fractions showed little net change between 2016 and 2020. The small increase (2–3%) observed between 2015 and 2016 was compensated by a small decrease (4%) largely taking place during 2016–2017.** The 2020 mole fraction was around 6.6 ppt, a reduction of 2.6 ppt from peak levels measured between 1996 and 1998. Reported quarantine and pre-shipment (QPS) consumption was relatively stable from 1996 to 2020.

Halogenated Very Short-Lived Substances (VSLs)

VSLs are defined as trace gases whose local lifetimes are shorter than 0.5 years and have non-uniform tropospheric abundances. These local lifetimes typically vary substantially over time and space. Of the very short-lived source gases (VSL SGs) identified in the atmosphere, brominated and iodinated species are predominantly of oceanic origin, while chlorinated species have significant anthropogenic sources. VSLs that reach the stratosphere will release the halogen they contain almost immediately and will thus play an important role for lower-stratospheric ozone in particular. Due to their short lifetimes and their atmospheric variability, the quantification of their contribution is much more difficult and has much larger uncertainties than for long-lived compounds.

- **Total tropospheric chlorine from VSL SGs in the background lower atmosphere is dominated by anthropogenic sources. It continued to increase between 2016 and 2020, but its contribution to total stratospheric chlorine remained small.** Global mean chlorine from VSLs in the troposphere has increased from about 103 ppt in 2016 to about 113 ppt in 2020. The relative contribution of VSLs to the stratospheric chlorine input amounted to 4% in 2020, compared to 3.6% in 2016.
- **Dichloromethane (CH_2Cl_2), with predominantly anthropogenic sources, is the main contributor to total chlorine from VSLs. It accounted for the majority of the change in VSLS chlorine between 2016 and 2020.** The CH_2Cl_2 global mean abundance reached approximately 40–45 ppt in 2020, which is more than a doubling compared to the early part of the century. The rate of increase slowed after 2016 but remained substantial. Regional CH_2Cl_2 emissions from Asia most likely account for most of this increase and more than offset a small decrease in European and North American emissions.
- **Brominated VSLSs contribute 5 ± 2 ppt to stratospheric bromine; this constitutes about 27% of total stratospheric bromine in 2020.** The main sources for brominated VSLSs are natural, and no long-term change is observed. Due to the decline in the abundance of controlled bromine compounds, the relative contribution of VSLSs to total stratospheric bromine increased by about 1% since 2016.
- **New evidence suggests that natural iodinated VSLSs contribute 0.3–0.9 ppt iodine to the stratosphere.** A rapid shift in the partitioning between gas-phase and particulate iodine has been detected in the upper troposphere. This

mechanism can enable iodine entrainment into the stratosphere in particulate form in addition to the entrainment in gas form. No observational trend estimates exist.

Stratospheric chlorine and bromine

In the stratosphere, chlorine and bromine can be released from organic source gases to form inorganic species, which participate in ozone depletion. In addition to estimates of the stratospheric input derived from the tropospheric observations, measurements of inorganic halogen loading in the stratosphere are used to determine trends of stratospheric chlorine and bromine.

- **The total chlorine input to the stratosphere for 2020 was 3240 ppt, which is 11.5% below the 1993 peak value, equivalent to a decline of 420 ± 20 ppt.** This long-term decrease was largely driven by decreasing abundances of CH_3CCl_3 and CFCs. The chlorine input for 2020 is derived from measurements of long-lived ODSs at the surface and estimates of stratospheric entrainment of VSLSs.
- **Hydrogen chloride (HCl) is the major reservoir of inorganic chlorine (Cl_y). Middle-stratosphere profile and total column measurements of HCl show a long-term decrease for the period 1997–2020 of around 0.5 ± 0.2% yr^{-1}.** If the evaluations are constrained to the shorter period 2005–2020 the satellite records show a rate of decrease of around 0.3 ± 0.2% yr^{-1}. This latter rate of decline in stratospheric HCl for the more recent period is in good agreement with expectations from the decline in tropospheric chlorine, which slowed after 2000.
- **Total bromine input to the stratosphere of 18.9 ppt is derived for 2020 by combining 13.9 ppt from long-lived gases and 5 ppt from VSLSs not controlled under the Montreal Protocol.** The total input declined by 14.5% between 1999 peak values and 2020. Anthropogenic emissions of all brominated long-lived gases are controlled, but as CH_3Br also has natural sources, more than 50% of the bromine reaching the stratosphere is now estimated to be from sources not controlled under the Montreal Protocol.
- **Total stratospheric bromine, derived from observations of bromine monoxide (BrO), has decreased at a rate of about 0.8% yr^{-1} since 2003.** This decline is consistent with the decrease in total tropospheric organic bromine, based on measurements of CH_3Br and the halons. There is no indication of a long-term change in natural sources of stratospheric bromine.

Equivalent Effective Stratospheric Chlorine (EESC)

EESC is the chlorine-equivalent sum of chlorine and bromine derived from ODS tropospheric abundances, weighted to reflect their expected depletion of stratospheric ozone. The growth and decline in EESC depend on a given tropospheric abundance propagating to the stratosphere with varying time lags (on the order of years) associated with transport to different regions of the stratosphere. Therefore, the EESC abundance, its peak timing, and its rate of decline are different in different regions of the stratosphere.

- **By 2020, EESC had declined from peak values by about 11% for polar winter conditions and by about 15% for mid-latitude conditions.** This drop to 1607 ppt is 37% of the decrease required for EESC in mid-latitudes to return to the 1980 benchmark level. In polar regions, the drop to 3710 ppt is about 23% of the decrease required to return to the 1980 benchmark level. However, regional estimates have indicated that EESC might be higher in some parts of the stratosphere, with an additional 200–300 ppt predominantly originating from CH_3Cl and CH_3Br. Contributions from the ozone-depleting VSLSs and nitrous oxide (N_2O) are currently not included in EESC calculations.

Tropospheric and Stratospheric Fluorine (F)

While fluorine has no direct impact on stratospheric ozone, many fluorinated gases are strong greenhouse gases, and their emissions are often related to the replacement of chlorinated substances controlled under the Montreal Protocol. For this reason, trends in fluorine are also assessed in this report.

- **The main sources of fluorine in the troposphere and in the stratosphere are CFCs, HCFCs, and HFCs (hydrofluorocarbons). In contrast to total chlorine, total fluorine in the troposphere continued to increase between 2016 and 2020, at a rate of 1.71% yr^{-1}.** This increase shows the decoupling of the temporal trends in fluorine and chlorine due to the increasing emissions of HFCs (see *Chapter 2*). The ODS contribution to the fluorine budget has started to decline, so that the fluorine trend due to ODSs alone became negative after 2016. In contrast, the fluorine trend due to HFCs has constantly increased, causing the total fluorine trend to increase as well. The Northern Hemisphere stratospheric abundance of inorganic fluorine has continued to increase at a rate of about 0.8% yr^{-1} since 2004.

Effect of ODSs on climate

- **The total direct radiative forcing of CFCs continues to be distinctly higher than that of HCFCs, with CFCs contributing around 68% of the total forcing from ODSs.** Radiative forcing from CFCs has dropped by 0.007 W m^{-2} since 2016 to about 0.257 W m^{-2} in 2020, while radiative forcing from HCFCs increased from 0.062 W m^{-2} to 0.064 W m^{-2} from 2016 to 2020. The total direct radiative forcing due to CFCs, HCFCs, halons, CCl_4, and CH_3CCl_3 was 0.337 W m^{-2} in 2020 (approximately 16% that of CO_2).
- **CO_2-equivalent emissions of CFCs and HCFCs were again approximately equal in 2020.** Based on 100-year time horizon global warming potentials (GWPs), the CO_2-equivalent emissions (in Gt CO_2-eq yr^{-1}) in 2020 were, for species where estimates are available, 0.7 ± 0.4 for CFCs, 0.7 ± 0.1 for HCFCs, 0.09 ± 0.03 for CCl_4 and CH_3CCl_3 combined, and 0.02 ± 0.01 for halons. The CO_2-equivalent emissions from the sum of CFCs, HCFCs, halons, CCl_4, and CH_3CCl_3 remained similar to the value reported in the last Assessment at approximately 1.5 Gt CO_2-eq in 2020.

Other gases that affect ozone and climate

- **Mole fractions of many other gases that affect both ozone and climate (including the three major greenhouse gases CH_4, N_2O, and CO_2) have changed since the last Assessment.** The atmospheric abundance of methane (CH_4) has continued to increase following a period of

stagnation in the early 2000s. The drivers of the changing trend are likely largely anthropogenic.

- **Mole fractions of N_2O, which is an ODS, continue to grow in the atmosphere, with growth rates exceeding some of the highest projections.** When expressed as a CFC-11-equivalent, anthropogenic N_2O emissions in 2020 were equal to more than two times the ODP-weighted emissions from all CFCs in that year. When compared to the CFC emission peak from 1987, those 2020 anthropogenic N_2O emissions were equal to more than 20% of the ODP-weighted emissions from CFCs in that year. Almost half of the N_2O emissions in recent years are anthropogenic in origin.
- **The global mole fractions of many non-ODS, non-HFC, highly fluorinated substances have continued to grow** (e.g., sulfur hexafluoride [SF_6], carbon tetrafluoride [CF_4], hexafluoroethane [C_2F_6], sulfuryl fluoride [SO_2F_2], and nitrogen trifluoride [NF_3]). These species contributed 0.014 W m^{-2} to anthropogenic radiative forcing in 2020. In contrast, the abundance of the sulfur-containing compound sulfur dioxide (SO_2) has not changed substantially, while carbonyl sulfide (COS) has shown a small negative trend.
- **Molecular hydrogen (H_2) is included in the Assessment for the first time, due to its potential future effects on stratospheric ozone. The decarbonization of the fossil fuel industry could lead to drastically increasing atmospheric mole fractions of H_2. The resulting future effects on ozone are currently not well understood but are expected to be small.** Atmospheric abundances of H_2 have increased from ~330 ppb during the mid-to-late 1800s to the present levels of 530–550 ppb in the late 20th and early 21st centuries.

1.0 INTRODUCTION

This chapter provides an update on the emissions rates and abundances of ozone depleting substances (ODSs) and other species of interest to the Montreal Protocol. In addition to the brief definitions given in the Scientific Summary, we describe the source of these data and how the metrics used in this chapter are derived. Observations of ODSs and other species of interest to the Montreal Protocol, as well as relevant quantities derived from those observations, are presented not only in this section but throughout *Chapters 1 and 2*. These observations have been carried out over multiple decades by several groups and networks with different sampling and measurement strategies. Independent and regularly compared and improved calibration scales have been derived, as highlighted in **Box 1-1**.

Globally and hemispherically representative abundances are mean dry air mole fractions and are expressed here also, and interchangeably, as mixing ratios (mostly in ppt). These abundances are derived using data from networks with ground-based air sampling stations that are distributed around the world: the Advanced Global Atmospheric Gases Experiment (AGAGE) network, the United States National Oceanic and Atmospheric Administration (NOAA) network, and the University of California, Irvine (UCI) network. For species that are primarily anthropogenic in origin, the difference between Northern and Southern Hemisphere (NH, SH) mole fractions is related to the global emission rate because their sources are concentrated in the Northern Hemisphere.

Further data representative of regional or hemispheric scales are available for some species from the National Institute for Environmental Studies (NIES) and the University of East Anglia/Forschungszentrum Jülich (UEA/FZJ). These networks maintain independent calibration scales and employ different measurement techniques, as well as different sampling locations and frequencies. As such, small differences (typically on the order of a few percent or less) in the burdens and trends estimated from each dataset are often observed. Therefore, for much of this section, global abundance trends and inferred emissions (using an atmospheric transport model, uncertainties of which are explained in **Box 1-2**) are given separately for each network. Data from regionally representative (e.g., Southern Hemisphere) sites are used when independent calibration scales exist (see **Box 1-1**) or global network data are not available. Particularly for species with atmospheric lifetimes of several years or more, these data can be extrapolated to derive global-scale mole fractions or emissions.

In terms of the atmospheric lifetimes of the species covered in this chapter, few manuscripts have been published since the last Assessment (e.g., Orkin et al., 2020; Suntharalingam et al., 2019; Burkholder et al., 2019), and these updates have been incorporated into emissions estimates only if they represent a significant change in understanding. Emission sources for many of the species covered in this chapter (especially the longer-lived ones) have been well known for some time, and the reader is therefore referred to the previous Assessment for a comprehensive overview. In this chapter, sources are covered only if substantial new evidence has been published since the last Assessment or if such coverage is necessary for the narrative of the particular section. Also note that all annually averaged data presented in this chapter are centered around the middle of that year.

As the ozone-depleting efficiency of the different halogen families is different, bromine and iodine "alpha" (scaling) factors are used to quantify the efficiency of ozone loss mediated by a single bromine or iodine atom relative to the loss caused by a single chlorine atom. Although the relative efficiency of these different species in destroying ozone depends on location, height, and season, average alpha factors are usually integrated for the polar and extra-polar (i.e., tropical and mid-latitudes) total column annual mean, with typical values ranging between 60 and 75 for bromine and between 150 and 300 for iodine (Ko, Poulet et al., 2003; Sinnhuber et al., 2009; Engel, Rigby et al., 2018; Klobas et al., 2021). Consistent with the last Assessment, we here use a bromine alpha factor of 60 for mid-latitudes and 65 for polar latitudes.

The number of observed species relevant for this chapter has been growing with each Assessment. Here, species with an average equivalent chlorine (ECl, using an alpha factor of 60 for bromine) contribution of less than 1 ppt near the surface in 2020 have been excluded from tables and figures. These species will be mentioned in the text only briefly in order to help maintain a focus on the more abundant ODSs and VSLSs. For species that do not directly affect stratospheric ozone, their relevance is largely determined by their impact on global warming. Therefore, compounds with a radiative forcing (RF) of less than 0.1 mW m^{-2} in 2020 are also excluded from tables and figures, with two exceptions: Carbonyl sulfide (COS) is included due to its relevance for stratospheric aerosol, and molecular hydrogen (H_2) is included due to its potential future relevance. To ensure that a consistent list of species is used for calculations of total F, Cl, and Br we have also included HCFC-124 throughout as the only species that does not fulfill the ECl criterion but contributes more than 0.1 mW m^{-2} to RF. The full list of species used in tables and figures is therefore as follows: CFCs: 11, 12, 13, 112, 113, 113a, 114, 114a, and 115; HCFCs: 22, 141b, 142b; halons: 1202, 1211, 1301, and 2402; solvents and methyl halides: CCl_4, CH_3CCl_3, CH_3Cl, and CH_3Br, VSLSs: CH_2Cl_2, $CHCl_3$, C_2Cl_4, all Br-VSLSs, and CH_3I; other fluorinated species: CF_4, C_2F_6, C_3F_8, *c*-C_4F_8, *n*-C_6F_{14}, SF_6, NF_3, SO_2F_2, and desflurane.

Total column and upper-tropospheric and stratospheric abundance observations are available for some species based on ground-based or satellite-based remote sensing methods.

Emissions, along with global and hemispheric mean mole fractions, are estimated using a 12-box model of atmospheric transport and chemistry, constrained using baseline atmospheric data and following a Bayesian inverse method described in Rigby et al. (2011; 2014). The model parameterizes the advection and eddy diffusion of trace gases between four zonal-mean boxes (separated at the equator and 30° N and S) for three vertical levels (separated at 500 and 200 hPa; e.g., Cunnold et al., 1983; Rigby et al., 2013). Trace gas lifetimes in the 12-box model are calculated based on rate constants for the reaction with the hydroxyl radical given in Burkholder et al. (2019), hydroxyl radical abundances described in Rigby et al. (2013), and steady-state stratospheric lifetimes as described in the *Annex* unless a different reference is given. The box model has undergone some minor changes since the previous Assessment, most notably the removal of some smoothing constraints on the emissions. Consequently, emissions and global mole fractions reported here may differ slightly from those reported in previous Assessments or in previously published literature. Similarly, other small differences primarily resulted from updated calibrations and usage of different datasets

Box 1-1. Methods for Determining Atmospheric Abundances

As noted by Hall et al. (2014), "there are many factors that can lead to differences in the data records collected by different groups…. Perhaps the most fundamental of these is the calibration scale upon which the measurements are based." The purpose of this box is to highlight the importance of calibration methods and to give insight into some of the basic principles. For the observational data presented in this chapter, there are two principal calibration approaches, depending on whether these observations are based on in situ (including flask collection-based) or remote sensing measurements (**Box 1-1 Figure 1**).

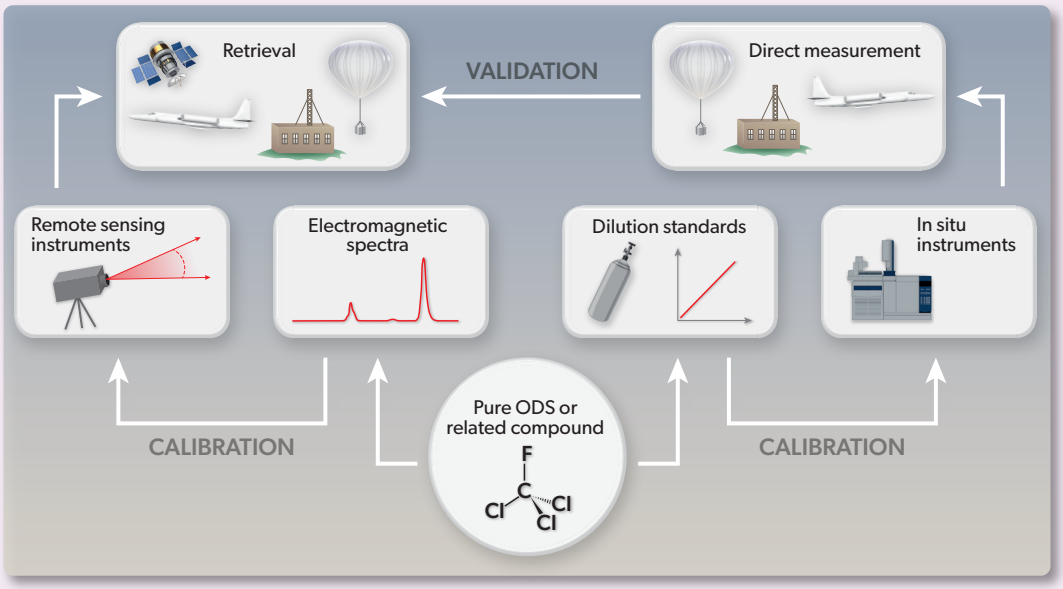

Box 1-1 Figure 1. Schematic of the processes used to calibrate global observations.

In situ measurement calibrations (e.g., Prinn et al., 2000; Laube et al., 2010) are typically based on the dilution of pure chemicals with gases containing virtually no trace species, such as oxygen-free nitrogen or synthetic air mixtures. Such a dilution can be static (i.e., mixing in canisters or other enclosures) or dynamic (i.e., in a continuous gas stream), the latter often being the preferred option for more reactive species, as these can be unstable when stored in canisters over longer periods. Due to the very low abundances of many of the ODSs and related species in the atmosphere, most dilutions have to take place over 10 to 13 orders of magnitude in order to reach a relevant concentration range. The determination of the amount of the to-be-calibrated species that is present initially is therefore of utmost importance. This includes ensuring and, if necessary, improving the purity of said substance (e.g., through freeze-drying cycles), as well as very accurate and precise methods of quantifying weight or volume (the latter being an approximation to mass-calibrated measurements after considerations of molar volume and ideal gas behavior). Often, one or several species with well-established calibration scales are also added as an "internal reference." Once diluted, the mixture is then analyzed with common measurement techniques such as cryogenic extraction from the main air components, followed by gas chromatographic separation and, for instance, detection with a mass spectrometer or an electron capture detector.

These calibration scales can then be transferred onto so-called "secondary standards," which are measured close in time and often consist of compressed tropospheric air samples in 30–50 L metal cylinders with passivated internal surfaces. For the long-term operation of global networks, it can be necessary to transfer the calibration scales further onto tertiary and even quaternary standards to ensure that results from all instruments on each field station are consistent with each other.

Remote sensing techniques use quantitative molecular spectroscopy to convert the strength of an absorption or emission feature in an atmospheric spectrum into abundances or concentrations, in line with the Beer-Lambert law. Concentrations of the halogenated species measured by remote sensing techniques (in **Table 1-2**) were derived using reference spectroscopy recorded in the laboratory, in particular air-broadened measurements of the target gas over a range of appropriate atmospheric temperatures and pressures. Spectroscopic parameters are made available in databases such as HITRAN (Gordon et al., 2021) or GEISA (Delahaye et al., 2022), which include uncertainty estimates on these reported parameters. Further work involves direct comparisons of in situ and remote sensing time series of trace gas abundances in ambient air, but the intercalibration of the respective scales is often complicated by the fact that these techniques give access to different quantities, e.g., surface concentrations in comparison to vertical profiles in the upper troposphere/lower stratosphere (UTLS), or to partial or total column abundances. However, advances have been made more recently for approaching these comparisons, as reported, e.g., in Prignon et al. (2019) for HCFC-22.

The enormous efforts that have gone into comparing, harmonizing, and improving calibration scales and quantifying and resolving potential differences between networks and groups (e.g., Jones et al., 2011; Hall et al., 2014; and the work of WMO Global Atmosphere Watch Calibration Centres) have been vital for ensuring the quality and comparability of the data underlying this and previous Assessments (**Figures 1-1** and **1-2**). The existence of several independent calibration scales for a given species is an essential part of the independent verification approach that is a key component of advancing scientific understanding, especially for monitoring the impacts of the Montreal Protocol and its subsequent Amendments. Some recent examples that also highlight the continued importance of these efforts are the comparison of long-term trends in the upper troposphere and stratosphere based on the ACE-FTS (Atmospheric Chemistry Experiment - Fourier Transform Spectrometer) satellite instrument (Steffen et al., 2019; Bernath et al., 2020; Bernath et al., 2021) with ground-based observations, the reevaluation and concentration range expansion of known species' calibrations such as CFC-11 or *c*-C_4F_8 (Montzka et al., 2018; Mühle et al., 2019), the quantification of isomeric impurities in more abundant species (Laube et al., 2016; Droste et al., 2020), and the detection of new species (Vollmer et al., 2019, 2021).

for calculation of hemispheric and global annual mole fractions. There are also small differences in global steady-state lifetimes, compared to the values reported in the *Annex*, due to differences in the model hydroxyl radical concentration and model transport.

For the long-lived species that are primarily of anthropogenic origin, we can use these global mole fraction and emissions estimates, as well as ozone depletion potentials (ODPs) as summarized in the *Annex*, to estimate radiative forcing, CO_2-equivalent emissions, and, for ODSs, CFC-11-equivalent emissions. As explained in detail in **Box 5-1**, we use the term "radiative forcing" to mean "stratosphere-adjusted radiative forcing" throughout this Assessment. For *Chapters 1* and *2*, estimates of the global radiative forcing due to most trace gases are derived as the global mean lower-tropospheric mole fraction multiplied by the radiative efficiency for each gas, using, for consistency with previous Assessments, stratosphere-adjusted radiative forcing values from the *Annex*. For methane (CH_4), nitrous oxide (N_2O), and CF_4 (for the latter we assume a preindustrial mole fraction of 40 ppt) we use the expression for radiative forcing from Ramaswamy et al. (2001). CO_2-equivalent emissions are calculated as the product of the emissions of each trace gas and its global warming potential (GWP) over a 100-year time horizon (also taken from the *Annex*). While other metrics are available to compare the climate impact of the emissions of different HFC species (e.g., Forster et al., 2021, we have used 100-year GWPs here because they are widely used, including in the Kigali Amendment. Uncertainties in radiative forcing and CO_2-equivalent emissions are due to the uncertainty in the atmospheric observations and trace gas lifetimes. They do not include uncertainties in radiative efficiencies or GWPs. Note that we use the recently updated radiative efficiencies from Hodnebrog et al. (2020) and Andersen et al. (2021) based on improved stratospheric estimates by Shine and Myhre (2020); this has resulted in higher GWPs for many species.

The production and emission of ODSs are closely linked to so-called "banks" of these compounds, a term that refers to an existing quantity of an ODSs that is contained in, e.g., equipment or stockpiles, and will eventually be released to the atmosphere if no action to the contrary is taken. Banks are only briefly mentioned here; for a more extensive discussion, we point the reader to *Chapter 7*. Finally, we are not aware of any peer-reviewed literature quantifying the impact of the COVID-19 pandemic on global or regional ODS abundances or emissions.

1.1 SUMMARY OF FINDINGS FROM THE PREVIOUS OZONE ASSESSMENT

Chapter 1 of the 2018 Assessment (Engel, Rigby et al., 2018) provided updates on ozone-depleting substances (ODSs) and other gases of interest to the Montreal Protocol, except for hydrofluorocarbons (HFCs), which were covered in Chapter 2.

During the five-year period 2012–2016, total tropospheric chlorine from substances controlled under the Montreal Protocol was declining at a rate of 12.7 ± 0.9 ppt yr^{-1}, with a slower-than-projected decrease in chlorofluorocarbon (CFC) concentrations and a slower-than-projected increase in first-stage replacement compounds (i.e., HCFCs) as compared to the 2014 A1 scenario. An increase in global CFC-11 emissions after 2012 was documented, suggesting new production not reported to the United Nations Environment Programme (UNEP). Stable or even increasing emissions of some of the low-abundance CFCs were also noted. The growth rate of chlorine from HCFCs declined relative to previous years and was comparable to values observed in the early 2000s.

The decrease of chlorine from controlled substances between 2012 and 2016 was partly offset by increases in the mainly natural CH_3Cl and mainly anthropogenic very short-lived gases (VSLSs), which are not controlled under the Montreal Protocol. Dichloromethane (CH_2Cl_2) was found to account for most of the rise in total tropospheric chlorine from VSLSs, and a substantial fraction of its global emissions were attributed to southern and eastern Asia.

Total chlorine entering the stratosphere from long-lived ODSs was reported to have declined by 405 ppt (12%) between the 1993 peak and 2016. While the VSLS contributions increased over the 2012–2016 period, their contribution to total chlorine remained below 4%. Hydrogen chloride (HCl), the major chlorine component in the upper stratosphere, decreased by about 6% between 2005 and 2016, consistent with the decline in total chlorine entering the stratosphere.

Total tropospheric bromine from controlled substances was reported to decline at a rate of 0.15 ± 0.04 ppt yr^{-1} between 2012 and 2016, primarily driven by a decline in atmospheric halons, with a smaller contribution from a decrease in methyl bromide (CH_3Br) abundance. Despite its overall decreasing trend, CH_3Br increased during 2015–2016 for the first time in a decade, most

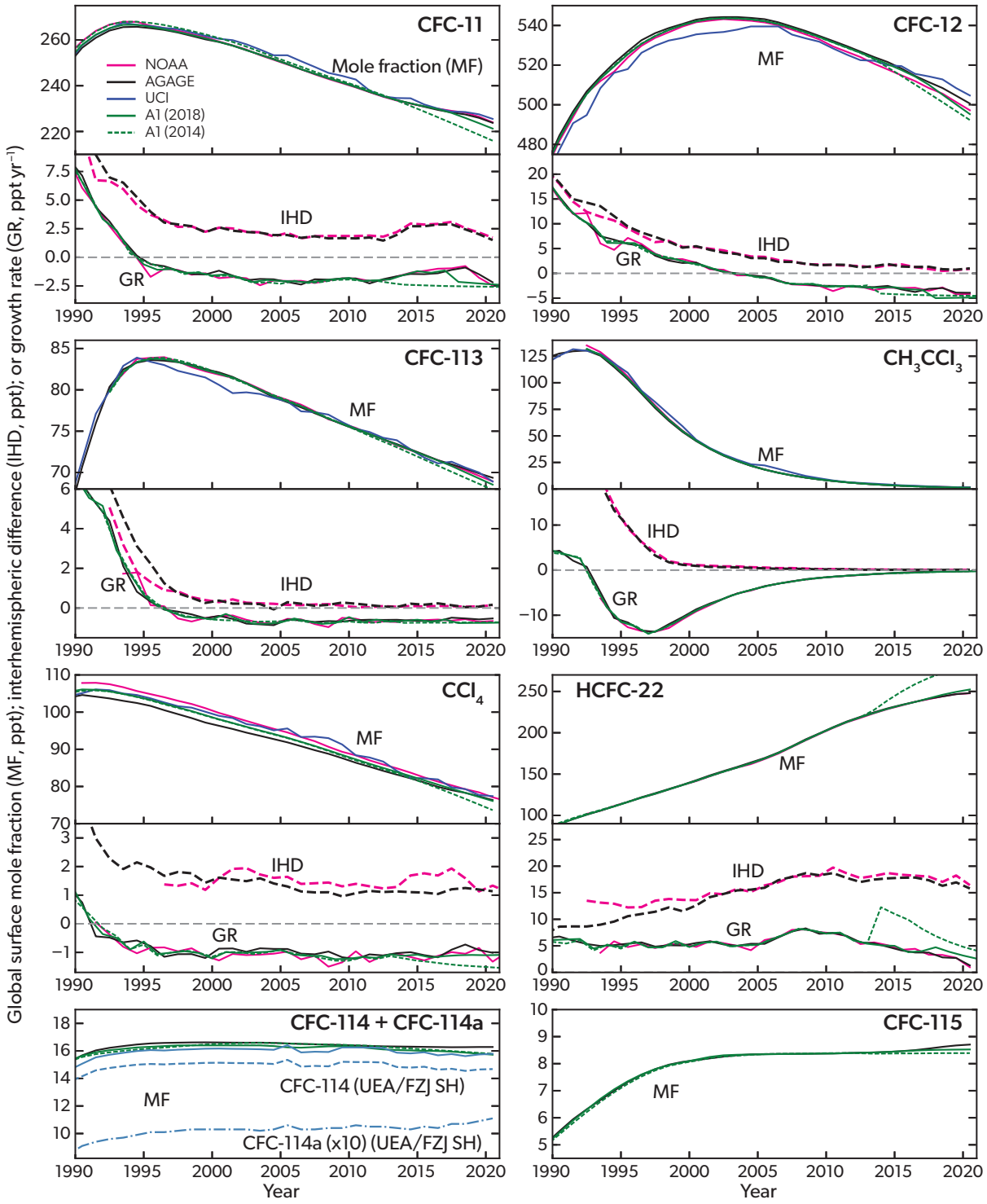

Figure 1-1. Annual mean mole fractions (MF) between 1990 and 2020 of ozone-depleting substances (except minor species; see *Introduction*), as measured from ground-based sampling networks and as simulated from the A1 scenarios of the previous two Ozone Assessments (dashed green line, Harris, Wuebbles et al., 2014; solid green line, Carpenter, Daniel et al., 2018). Mole fractions from the NOAA (red), AGAGE (black), and UCI (blue) networks were calculated as mid-year-centered global annual mole fractions. Annual mole fractions from UEA/FZJ (steel blue) represent mid-year-centered annual mole fractions observed in unpolluted whole-air flask samples collected at Cape Grim, Australia. Annual mean mole fractions from the A1 scenarios are interpolations from the simulated January-centered annual mole fractions. For some gases, we also show inter-hemispheric differences (IHD; defined as NH minus SH mole fraction; dashed lines) and growth rates (GR; ppt yr^{-1}; solid lines) in the lower panels, using the same color scheme as in the corresponding upper panels. Note that, compared to values reported in the last Assessment,

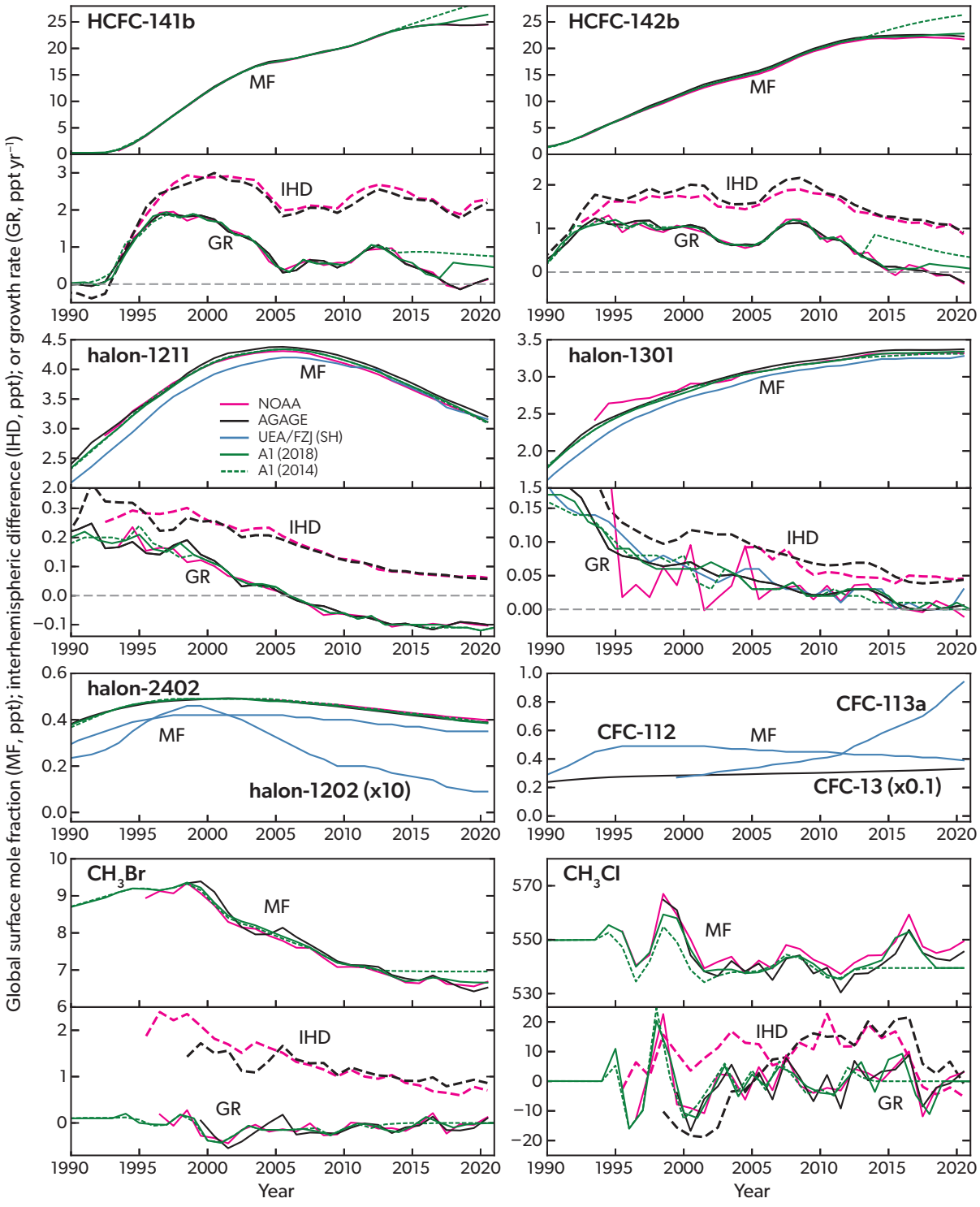

there were several changes in the NOAA reported global annual mean mole fractions associated with termination or changing instrumentations and updates in calibrations: The global annual mean mole fractions for CCl_4 were calculated from NOAA in situ measurements in this Assessment, whereas NOAA flask and in situ measurements were included for the calculation for the previous Assessments; the calibration of NOAA in situ measurements of CFC-12 were reassessed since the last Assessment, and the reported mole fractions of halon-1301 were scaled by a factor of 1.015 to be consistent with measurements from a new instrument. AGAGE CFC-113 data prior to approximately 2011 were measured by GC-ECD and likely contain a small fraction (0.2–0.4 ppt) of CFC-113a. Global GRs and IHDs derived from UCI data are not plotted because they show much higher variability, likely related to more regional influence on this sampling network.

likely not related to anthropogenic sources. Total bromine entering the stratosphere from well-mixed ODSs also continued to decline, with a total decrease of 2.4 ppt (15%) between the 1998 peak and 2016. Brominated VSLSs, of primarily natural origin, were found to contribute about 25% to total bromine in 2016 and showed no long-term changes. Total stratospheric bromine derived from bromine monoxide (BrO) observations decreased by about 8% from 2004 to 2014, which is again consistent with the decline in total bromine entering the stratosphere.

Equivalent effective stratospheric chlorine (EESC) was assessed to have declined from its maximum value in polar regions by about 9% and in mid-latitudes by about 13–17%. The rate at which EESC was decreasing had slowed, in accordance with a slowdown of the decrease in tropospheric chlorine. A new and improved methodology for estimating EESC was found to result in smaller recovery rates of stratospheric halogen loading with respect to their maximum peak, especially in mid-latitudes.

The influence of CFC and HCFC emissions on climate was assessed in terms of their equivalent in gigatonnes of carbon dioxide (CO_2-equivalent emissions) using 100-year GWPs. While the direct radiative forcing of CFCs continued to be much higher than for HCFCs, the CO_2-equivalent emissions of CFCs and HCFCs were roughly equal in 2016.

1.2 ABUNDANCES, TRENDS, LIFETIMES, AND EMISSIONS OF LONGER-LIVED HALOGENATED SOURCE GASES

1.2.1 Chlorofluorocarbons (CFCs)

Observations of Atmospheric Abundance. Global mole fractions of the two most abundant CFCs, i.e., CFC-12 (CCl_2F_2) and CFC-11 (CCl_3F), continued to decline since 2016, reaching approximately 499 ppt and 224 ppt, respectively, in 2020 (**Figure 1-1**). The atmospheric abundance of CFC-12 has fallen increasingly rapidly throughout this period, with the rate of decline increasing from 3.3 ppt yr^{-1} in 2015–2016 to around 4.0 ppt yr^{-1} in 2019–2020 (**Figure 1-1** and **Table 1-1**). For CFC-11, a slowdown in the rate at which the global abundance was falling after 2012 had been reported in the last Assessment (Engel, Rigby et al., 2018; Montzka et al., 2018). A major driver of this slowdown from around 2 ppt yr^{-1} to around 1.3 ppt yr^{-1} has now been identified as renewed emissions from eastern China (Rigby et al., 2019; Adcock et al., 2020), with satellite-based evidence also indicating CFC-11 sources in the vicinity of the Indian and Arabian peninsulas adding to the slowdown over 2013–2018 (Chen et al., 2020). More recently, Park et al. (2021) and Montzka et al. (2021) reported another turnaround, i.e., an increase in the rate of decline in CFC-11 abundance since 2018 that is equivalent to a return to pre-2012 values. A thorough and detailed overview on all recent findings related to atmospheric CFC-11 can be found in the *"Report on the Unexpected Emissions of CFC-11"* (WMO, 2021). As an update to the findings of that report, global CFC-11 mole fractions decreased from 2019 to 2020 even faster than from 2018 to 2019, by an unprecedentedly large amount of 2.3 ppt yr^{-1}. In addition, several observation-based publications have since confirmed unusually high abundances of various CFCs, most notably CFC-11 and CFC-12, in different parts of China during 2009–2019 (Zeng et al., 2020; Yang et al., 2021; Benish et al., 2021; Huang et al., 2021; Lin et al., 2021). However, it should be noted that quantitative conclusions from these latter studies are limited due to one or more factors, such as scarcity of the data, lack of regional background mole fractions, higher uncertainties, and potential calibration or measurement biases indicated by reported CFC mole fractions lower than their global background levels in the same time intervals. The inter-hemispheric differences (IHDs) derived for the two main CFCs are consistent with the

Table 1-1. Annual mean mole fractions, mole fraction changes, global emissions, and CO_2-equivalent emissions (based on 100-year GWPs) of ozone-depleting gases measured from ground-based sampling networks (except minor species; see *Introduction*). Emission uncertainties are given as 1 standard deviation (1-sigma) and more specific details can be found in the footnote.

General footnote: Mole fractions in this table represent independent estimates based on air sampling at Earth's surface from different research groups for the years indicated. Results in bold text are estimates of globally averaged annual mole fractions. Regional data from relatively unpolluted sites are shown (in italics) where global estimates are not available, where global estimates are available from only one network, or where data from global networks do not represent independent calibration scales. Absolute changes (ppt yr^{-1}) are calculated by subtracting the 2019 annual mole fractions from the 2020 annual mole fractions; relative changes (% yr^{-1}) are this difference relative to the 2019 value. Annual mole fractions reported by AGAGE were calculated based on the simulated surface mole fractions using a 12-box inverse model (e.g., Cunnold et al., 1983; Rigby et al., 2013) that were optimized to represent the AGAGE in situ observations made at remote locations. Annual mole fractions reported by NOAA are weighted annual averages from the measured monthly mole fractions from whole-air flask measurements made at remote locations, except for CFC-11, CFC-12, and CFC-113, which include both NOAA in situ and flask measurements at those remote locations, and CCl_4, which includes only NOAA in situ measurements. Differences to the 2016 values reported in the last Assessment primarily result from either minor box model changes (AGAGE data: <0.2 ppt for all species except CFC-12 and CH_3Cl <1.6 ppt) or updated calibrations and usage of different datasets for the calculation of hemispheric and global annual mole fractions (NOAA data: <0.3 ppt); i.e., the calibration of NOAA in situ CFC-12 measurements was adjusted to improve the overall consistency among the six sampling and measurement locations. Mole fractions reported by UEA/FZJ are annual averages of measured mole fractions from whole-air flask samples collected at Cape Grim, Australia, and are based on volumetric calibration scales, except for halon-1211 and halon-1301 (NOAA-based). Mole fractions reported by NIES are annual average mole fractions from in situ measurements made in Japan and are based on a gravimetric calibration scale. Mole fractions reported by UCI are based on flask air samples in the Pacific region spanning both hemispheres and are based on volumetric calibration scales. Reported global annual emissions were calculated based on the AGAGE and NOAA observations using the 12-box model mentioned above; "n.a." indicates that emissions were not available. These observations are updated from the following sources: Butler et al. (1998); Laube et al. (2014); Laube et al. (2016); Miller et al. (2008); Montzka et al. (2003); Montzka et al. (2015); Montzka et al. (2021); Newland et al. (2013); O'Doherty et al. (2004); Prinn et al. (2018); Rigby et al. (2014); Simmonds et al. (2017); Simpson et al. (2007); Vollmer et al. (2016); Vollmer et al. (2018); Yokouchi et al. (2006); AGAGE (agage.eas.gatech.edu); NOAA (gml.noaa.gov/dv/site); UCI (data.ess-dive.lbl.gov/view/doi:10.3334/CDIAC/ATG.002).

Notes:
[1] AGAGE calibrations were specified in Prinn et al. (2018).
[2] The NOAA data used the same calibrations as those published in the previous Assessment, except for H-1301 (see caption of **Figure 1-1**).
[3] Measurements of CFC-114 from AGAGE are a combination of CFC-114 and the CFC-114a isomer.
[4] CFC-114 and CFC-114a are quantified separately by UEA/FZJ.

Table 1-1. *See caption on facing page.*

Chemical	Mole Fraction (ppt)		Change (2019–2020)		Emissions (Gg yr^{-1})		CO_2-eq. Emissions (Tg yr^{-1})	Network
	2016	2020	(ppt yr^{-1})	(% yr^{-1})	2016	2020	2020	
CFCs								
CCl_3F (CFC-11)	**229.4**	**223.8**	**–2.2**	**–1.0**	**67 ± 10**	**48 ± 10**	**310 ± 64**	AGAGE[1]
	230.0	**224.0**	**–2.5**	**–1.1**	**77 ± 10**	**46 ± 10**	**298 ± 62**	NOAA[2]
	230.0	**225.5**	**–2.0**	**–0.9**	**n.a.**	**n.a.**	**n.a.**	UCI
CCl_2F_2 (CFC-12)	**514.5**	**500.7**	**–3.9**	**–0.8**	**30 ± 21**	**27 ± 21**	**334 ± 268**	AGAGE
	511.9	**497.2**	**–4.2**	**–0.8**	**36 ± 21**	**23 ± 20**	**282 ± 252**	NOAA
	515.6	**504.7**	**–3.7**	**–0.7**	**n.a.**	**n.a.**	**n.a.**	UCI
$CClF_3$ (CFC-13)	**3.18**	**3.32**	**0.04**	**1.1**	**0.5 ± 0.2**	**0.6 ± 0.2**	**10 ± 3**	AGAGE
CCl_2FCCl_2F (CFC-112)	*0.42*	*0.39*	*–0.01*	*–1.8*	*n.a.*	*n.a.*	*n.a.*	UEA/FZJ
CCl_2FCClF_2 (CFC-113)	**71.5**	**69.4**	**–0.5**	**–0.7**	**6.5 ± 6.4**	**6.9 ± 6.0**	**45 ± 39**	AGAGE
	71.5	**68.9**	**–0.7**	**–1.0**	**5.5 ± 5.0**	**6.4 ± 4.8**	**42 ± 32**	NOAA
	71.1	**70.0**	**–1.1**	**–1.6**	**n.a.**	**n.a.**	**n.a.**	UCI
CCl_3CF_3 (CFC-113a)	*0.66*	*0.94*	*0.09*	*10*	*n.a.*	*n.a.*	*n.a.*	UEA/FZJ
$CClF_2CClF_2$ (CFC-114)	**16.28**	**16.28**	**–0.01**	**–0.03**	**2.3 ± 0.9**	**2.6 ± 0.9**	**24 ± 8**	AGAGE[3]
	14.64	*14.68*	*0.03*	*0.2*	*n.a.*	*n.a.*	*n.a.*	UEA/FZJ[4]
CCl_2FCF_3 (CFC-114a)	*1.04*	*1.11*	*0.02*	*1.7*	*n.a.*	*n.a.*	*n.a.*	UEA/FZJ[4]
$CClF_2CF_3$ (CFC-115)	**8.50**	**8.71**	**0.03**	**0.4**	**1.5 ± 0.5**	**1.0 ± 0.6**	**10 ± 5**	AGAGE
	8.62	*8.86*	*–0.02*	*–0.2*	*n.a.*	*n.a.*	*n.a.*	NIES
HCFCs								
$CHClF_2$ (HCFC-22)	**237.5**	**248.0**	**1.3**	**0.5**	**375 ± 53**	**348 ± 55**	**664 ± 104**	AGAGE
	237.4	**247.8**	**1.0**	**0.4**	**373 ± 51**	**337 ± 53**	**643 ± 102**	NOAA
	242.3	**256.1**	**3.3**	**3.1**	**n.a.**	**n.a.**	**n.a.**	UCI
CH_3CCl_2F (HCFC-141b)	**24.49**	**24.52**	**0.14**	**0.58**	**60 ± 9**	**58 ± 9**	**47 ± 7**	AGAGE
	24.53	**24.50**	**0.12**	**0.5**	**62 ± 8**	**56 ± 8**	**45 ± 7**	NOAA
	24.6	**25.8**	**–0.2**	**–0.8**	**n.a.**	**n.a.**	**n.a.**	UCI
CH_3CClF_2 (HCFC-142b)	**22.54**	**22.23**	**–0.23**	**–1.0**	**24 ± 4**	**19 ± 4**	**41 ± 10**	AGAGE
	22.02	**21.69**	**–0.26**	**–1.2**	**25 ± 4**	**19 ± 4**	**41 ± 10**	NOAA
	23.2	**22.8**	**0.00**	**0.0**	**n.a.**	**n.a.**	**n.a.**	UCI
Halons								
CBr_2F_2 (halon-1202)	*0.014*	*0.009*	*–0.000*	*0.0*	*n.a.*	*n.a.*	*n.a.*	UEA/FZJ
$CBrClF_2$ (halon-1211)	**3.59**	**3.21**	**–0.10**	**–3.0**	**3.2 ± 1.8**	**2.9 ± 1.6**	**6 ± 3**	AGAGE
	3.51	**3.11**	**–0.10**	**–3.2**	**3.4 ± 1.8**	**2.9 ± 1.6**	**6 ± 3**	NOAA
	3.70	**3.36**	**–0.09**	**–2.6**	**n.a.**	**n.a.**	**n.a.**	UCI
	3.53	*3.16*	*–0.07*	*–2.3*	*n.a.*	*n.a.*	*n.a.*	UEA/FZJ
$CBrF_3$ (halon-1301)	**3.36**	**3.37**	**0.01**	**0.18**	**1.2 ± 0.6**	**1.4 ± 0.6**	**10 ± 4**	AGAGE
	3.31	**3.32**	**–0.01**	**–0.3**	**1.3 ± 0.3**	**1.1 ± 0.5**	**9 ± 3**	NOAA
	3.25	*3.28*	*0.03*	*0.8*	*n.a.*	*n.a.*	*n.a.*	UEA/FZJ
$CBrF_2CBrF_2$ (halon-2402)	**0.41**	**0.39**	**0.00**	**–1.0**	**0.4 ± 0.1**	**0.5 ± 0.1**	**1.1 ± 0.3**	AGAGE
	0.42	**0.40**	**–0.01**	**–1.5**	**0.4 ± 0.1**	**0.4 ± 0.1**	**0.9 ± 0.3**	NOAA
	0.36	*0.35*	*–0.00*	*0.0*	*n.a.*	*n.a.*	*n.a.*	UEA/FZJ
Chlorocarbons								
CH_3Cl (methyl chloride)	**553.6**	**545.5**	**3.3**	**0.6**	**4699 ± 960**	**4720 ± 946**	**28 ± 6**	AGAGE
	559.3	**549.4**	**3.0**	**0.6**	**4756 ± 975**	**4718 ± 959**	**28 ± 6**	NOAA
CCl_4 (carbon tetrachloride)	**79.92**	**76.34**	**–1.01**	**–1.3**	**42 ± 15**	**41 ± 14**	**89 ± 30**	AGAGE
	81.31	**77.10**	**–1.32**	**–1.7**	**45 ± 15**	**46 ± 14**	**99 ± 31**	NOAA
	81.9	**77.4**	**–0.3**	**–0.4**	**n.a.**	**n.a.**	**n.a.**	UCI
CH_3CCl_3 (methyl chloroform)	**2.62**	**1.42**	**–0.23**	**–14**	**2.2 ± 2.0**	**2.3 ± 1.1**	**0.4 ± 0.2**	AGAGE
	2.60	**1.40**	**–0.22**	**–14**	**2.9 ± 1.8**	**2.2 ± 1.0**	**0.4 ± 0.2**	NOAA
	3.05	**1.47**	**–0.26**	**–15**	**n.a.**	**n.a.**	**n.a.**	UCI
Bromocarbons								
CH_3Br (methyl bromide)	**6.85**	**6.52**	**0.10**	**1.6**	**135 ± 21**	**131 ± 20**	**0.26 ± 0.04**	AGAGE
	6.85	**6.68**	**0.12**	**1.9**	**136 ± 20**	**134 ± 20**	**0.27 ± 0.04**	NOAA

aforementioned accelerated mole fraction changes, as they have also been decreasing after 2018 (**Figure 1-1**).

Measurements of the 2014–2020 trends in northern hemisphere (NH) CFC-11 and CFC-12 abundances made using ground-based Fourier transform infrared (FTIR) spectroscopy at Jungfraujoch, Switzerland, agree within uncertainties with those derived using surface-based in situ observations (**Table 1-2** and **Figure 1-2**). Upper-tropospheric NH trends derived from ACE-FTS measurements are slightly less negative than their ground-based counterparts (**Table 1-2**). The causes for these differences are not entirely clear; however, it should be noted that due to the irregularity of the ACE-FTS sampling, trends tend to be more robust over longer time periods. Recently it has been shown that long-term CFC-11 near-surface abundances can be extracted from the nadir-viewing AIRS (Atmospheric InfraRed Sounder) instrument; the retrieved trends agree with those derived from ground observations within their 95% confidence intervals (Chen et al., 2020). This approach opens up the possibility of monitoring CFC-11 via other nadir sounders such as the Cross-track Infrared Sounder (CrIS) and the Infrared Atmospheric Sounding Interferometer (IASI), both of which offer a greater density of global coverage relative to ACE-FTS.

CFC-113 (CCl_2FCClF_2) near-surface global mole fractions also have continued to decline, from 72 ppt in 2016 to 69 ppt in 2020. The rate of decline in CFC-113 has remained relatively constant at around 0.6 ppt yr^{-1}, and its IHD has remained approximately stable (**Figure 1-1**). The 2014–2020 trends in NH CFC-113 from the ACE-FTS retrievals do not agree well with surface measurement–derived values (**Table 1-2**). The ACE-FTS retrieval of CFC-113 has a number of artifacts that contribute toward this trend bias; in Bernath et al. (2021), the ACE-FTS trend is ~70% more negative than that derived from near-surface observations.

The previous Assessment reported a slowdown in the decline of the combined mole fraction of the CFC-114 ($CClF_2CClF_2$) and CFC-114a (CCl_2FCF_3) isomers. This has continued, such that there has been virtually no change in global abundance between 2016 and 2020 (**Figure 1-1** and **Table 1-1**; update from Vollmer et al., 2018). In 2020, the global mean mole fraction of combined CFC-114 and CFC-114a was still approximately 16 ppt, while the mole fraction of CFC-114a (only available from measurements in the Southern Hemisphere) increased slightly from 1.0 ppt to 1.1 ppt since 2016 (update of Laube et al., 2016). On a regional scale, enhanced mole fractions of CFC-114 have been observed in air masses above China (Zeng et al., 2020; Yang et al., 2021; Benish et al., 2021), though the portions of these signals caused by its hard-to-separate isomer CFC-114a are not quantified.

In the 2018 Assessment, it was reported that the mole fraction of CFC-115 ($CClF_2CF_3$) had grown since 2012, reaching 8.5 ppt in 2016 (update from Vollmer et al., 2018). This trend has continued, with CFC-115 reaching 8.7 ppt in 2020. For CFC-13 ($CClF_3$), the previously reported slow growth has also continued, and the global mole fraction increased from 3.18 ppt in 2016 to 3.32 ppt in 2020 (update from Vollmer et al., 2018).

Since the last Assessment, CFC-112 (CCl_2FCCl_2F), which had a southern hemisphere (SH) mole fraction of 0.42 ppt in 2016, has continued to decline in the atmosphere, to 0.39 ppt in 2020. The abundance of its isomer CFC-112a ($CClF_2CCl_3$) has, however, started to increase recently in the SH, from 0.07 to 0.08 ppt between 2016 and 2020 (update of Laube et al., 2014). In addition, CFC-113a (CCl_3CF_3) mole fraction increases have accelerated for a second time in the Southern Hemisphere (first around 2012, and then again after 2016), reaching 0.95 ppt in 2020 (compared to 0.66 ppt in 2016) (update from Adcock et al., 2018; **Table 1-1**).

For CFC-216ba ($CClF_2CClFCF_3$), no significant change in SH abundance was observed since the last Assessment (0.04 ppt, update from Kloss et al., 2014), and there is no update available for CFC-216ca ($CClF_2CF_2CClF_2$; 2016: 0.02 ppt).

Emissions, Lifetimes, and Radiative Forcings. Atmospheric lifetimes of CFCs have not been reevaluated since the 2014 Assessment, although one recent publication has assessed the influence of the oceanic reservoir to be currently of no significant importance to the CFC-11 lifetime (Wang et al., 2021). Therefore, the lifetime estimates used here—which underpin all emission estimates—are again still largely based on SPARC (2013), with small

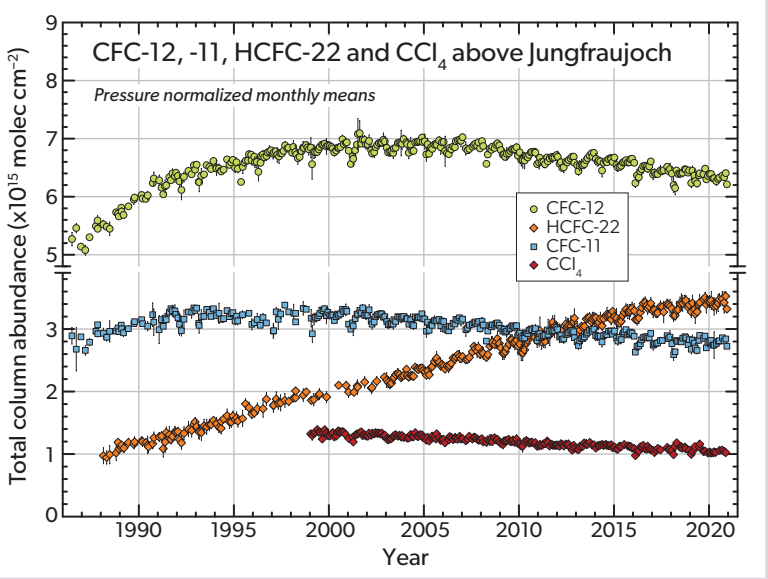

Figure 1-2. Monthly mean total vertical column abundance time series of CFC-12, CFC-11, HCFC-22, and CCl_4 derived from the long-term FTIR monitoring program conducted at the Jungfraujoch station, Switzerland (46.5°N), from 1986 to 2021 (updated from Zander et al., 2008; Gardiner et al., 2008; Rinsland et al., 2012; and Prignon et al., 2019). Note the discontinuity in the vertical scale.

Table 1-2. Annual trends of selected ODSs, CF_4, and SF_6 for the 2014–2020 time period derived from surface measurements as well as ground-based and satellite remote sensing observations. Trends derived from in situ measurements were based on linear regression of the hemispheric annual mole fractions calculated from the NOAA and AGAGE observations for 30–90°N. Their associated uncertainties were calculated from uncertainties in the slopes and the differences in the relative trends derived from NOAA and AGAGE observations. For CF_4, only AGAGE data were used. For ground-based remote sensing observations, relative annual rates of change were computed from FTIR observations at Jungfraujoch station, Switzerland, with the bootstrap resampling tool described in Gardiner et al. (2008). All uncertainties are estimated at 2-sigma. For satellite remote sensing observations, the ACE-FTS trends were determined for 0–60°N, from the least-squares linear regression of averaged mixing ratios in molecule-dependent upper-tropospheric altitude ranges (updated from Bernath et al., 2021). For CF_4, the trend was calculated over the altitude range 25.5–40.5 km due to problems with the retrieval in the troposphere. Trend uncertainties were calculated from uncertainties in the slopes and intercepts of the regression lines. As opposed to the in situ-based mole fractions, those derived from ACE-FTS and FTIR are volume-based and not dry air, which may account for part of the differences.

Annual Trend 2014 – 2020 (% yr^{-1} relative to 2017)			
Substance	**In situ (surface)**	**Remote sensing ground-based (total column)[1,2]**	**Remote sensing satellite (upper troposphere)[3,4]**
CFC-11	–0.61 ± 0.10	–0.72 ± 0.19	–0.46 ± 0.04
CFC-12	–0.69 ± 0.02	–0.72 ± 0.09	–0.59 ± 0.04
CFC-113	–0.84 ± 0.04	N/A	–1.58 ± 0.05
CCl_4	–1.24 ± 0.12	–1.31 ± 0.22	–1.14 ± 0.05
HCFC-22	1.19 ± 0.19	1.36 ± 0.13	1.43 ± 0.15
HCFC-141b	0.23 ± 0.24	N/A	–0.82 ± 0.29
HCFC-142b	–0.24 ± 0.22	0.50 ± 0.73	0.61 ± 0.34
CF_4	1.07 ± 0.02	0.93 ± 0.07	1.07 ± 0.06
SF_6	3.56 ± 0.11	3.86 ± 0.14	3.73 ± 0.15

Notes:
[1] The Jungfraujoch FTIR trends are based on observations of CFC-11, CFC-12 (updated from Zander et al., 2008), CCl_4 (updated from Rinsland et al., 2012), HCFC-22 (updated from Prignon et al., 2019), HCFC-142b (updated from Mahieu et al., 2017), CF_4 (updated from Mahieu et al., 2014b), SF_6 (updated from Zander et al., 2008). Note that the HCFC-142b trend is not significant at 2-sigma uncertainty.
[2] The methods used for the determination of the uncertainties affecting the retrieved trends for remote sensing–based observations benefited from recent research developments that account for the autocorrelation and heteroskedasticity (i.e., changing variance with time) that are often present in such geophysical time series. Previous statistical tools used random permutations of the residuals (differences between the fitted function and the observations) in order to assess the trend distribution and associated uncertainty (Gardiner et al., 2008). This approach has the disadvantage of failing to preserve the possible autocorrelation and heteroskedasticity of the residuals, since they are randomly resampled. More recent studies (Friedrich et al., 2020a, 2020b) present improved statistical tools based on the autoregressive wild bootstrap method that do not involve any permutation of the residuals. They are therefore more appropriate for geophysical time series and are expected to provide a more reliable estimate of the uncertainties associated with the trends. This is particularly important when dealing with small rates of change.
[3] Uncertainties are also 2-sigma but currently not derived in a way that is comparable to the other data shown in this table.
[4] Remote sensing satellite trends are taken solely from ACE-FTS measurements (updated from Bernath et al., 2021).

changes due to reaction rate updates (Burkholder et al., 2019), and are given in the *Annex*.

CFC emissions to the atmosphere have for several years been expected to be due only to leakage from banks and therefore to decline with time as the size of the banks decreases. This appears to be qualitatively the case for CFC-12, as its emissions have continued to decrease since the previous Assessment. The aforementioned *"Report on the Unexpected Emissions of CFC-11"* (WMO, 2021) also included research on CFC-12, as the two species are often co-produced. Similar to CFC-11, a slowdown in the decline of emissions was also observed for CFC-12 between 2010 and 2017, followed by a small but not significant emission reduction between 2017 and 2019. In 2020, the fall in CFC-12 emissions continued, reaching a new all-time minimum of approximately 25 Gg yr^{-1} (**Table 1-1**, **Figure 1-3**).

Concurrent with the recent accelerated decrease in CFC-11 atmospheric abundances, CFC-11 emissions have declined markedly in recent years: from 72 Gg yr^{-1} in 2016 to 47 Gg yr^{-1} in both 2019 and 2020 (**Table 1-1**), corresponding to a drop of more than 30%. Importantly, the research carried out after the renewed increases in emissions of CFC-11 were observed (Montzka et al., 2018) highlighted several factors that currently limit the ability to accurately estimate when emissions of CFCs and other long-lived controlled species diverge from expectations. Among these factors are uncertainties in emissions from banks (e.g., Lickley et al., 2020; see also *Chapter 7*) and variability in air transport to and from their main sink region in the stratosphere (Montzka et al., 2018; Ray et al., 2020; Laube et al., 2020; Lickley et al., 2021; Ruiz et al., 2021). Also challenging, in terms of pinpointing the sources of such emissions, is the lack of precise, accurate, frequent, and regular measurements in many regions of the world (Rigby et al., 2019). Emission uncertainties are highlighted in **Box 1-2**.

Emissions of CFC-113 are estimated at 6.0 Gg yr^{-1} in 2016 and 6.6 Gg yr^{-1} in 2020. However, since these annual estimates have relatively large uncertainties of around 5–6 Gg yr^{-1}, this is not a significant change. Importantly, CFC-113 emissions remain much lower than in the 1990s; nevertheless, a significant further decrease should be detectable over longer timescales, and its absence has been notable for some time (Lickley et al., 2020; **Figure 1-3**).

Of the less abundant CFCs, CFC-13 emissions plateaued at around 0.5 ± 0.2 Gg yr^{-1} in the decade leading up to the last

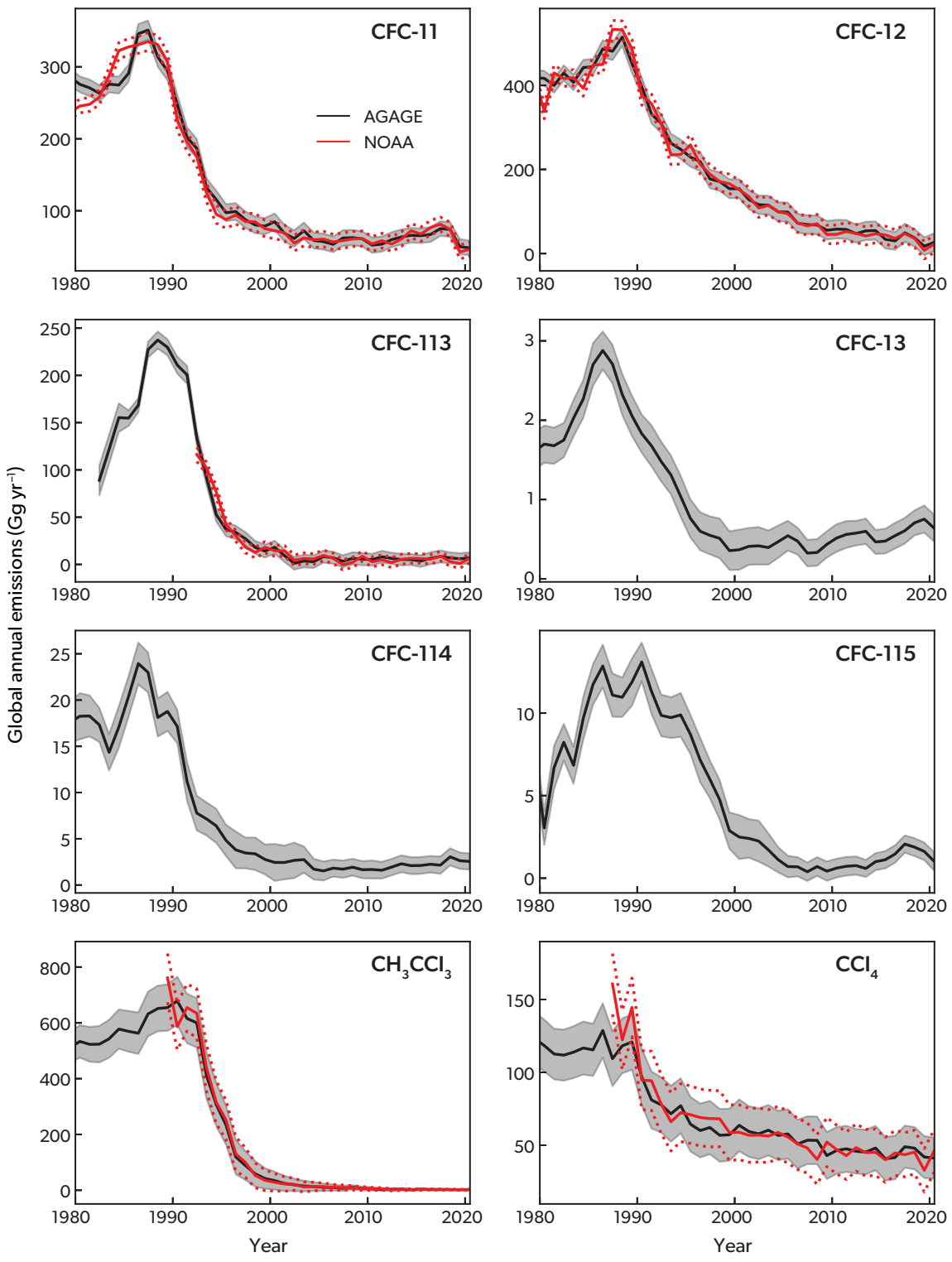

Figure 1-3. *Continued on next page.*

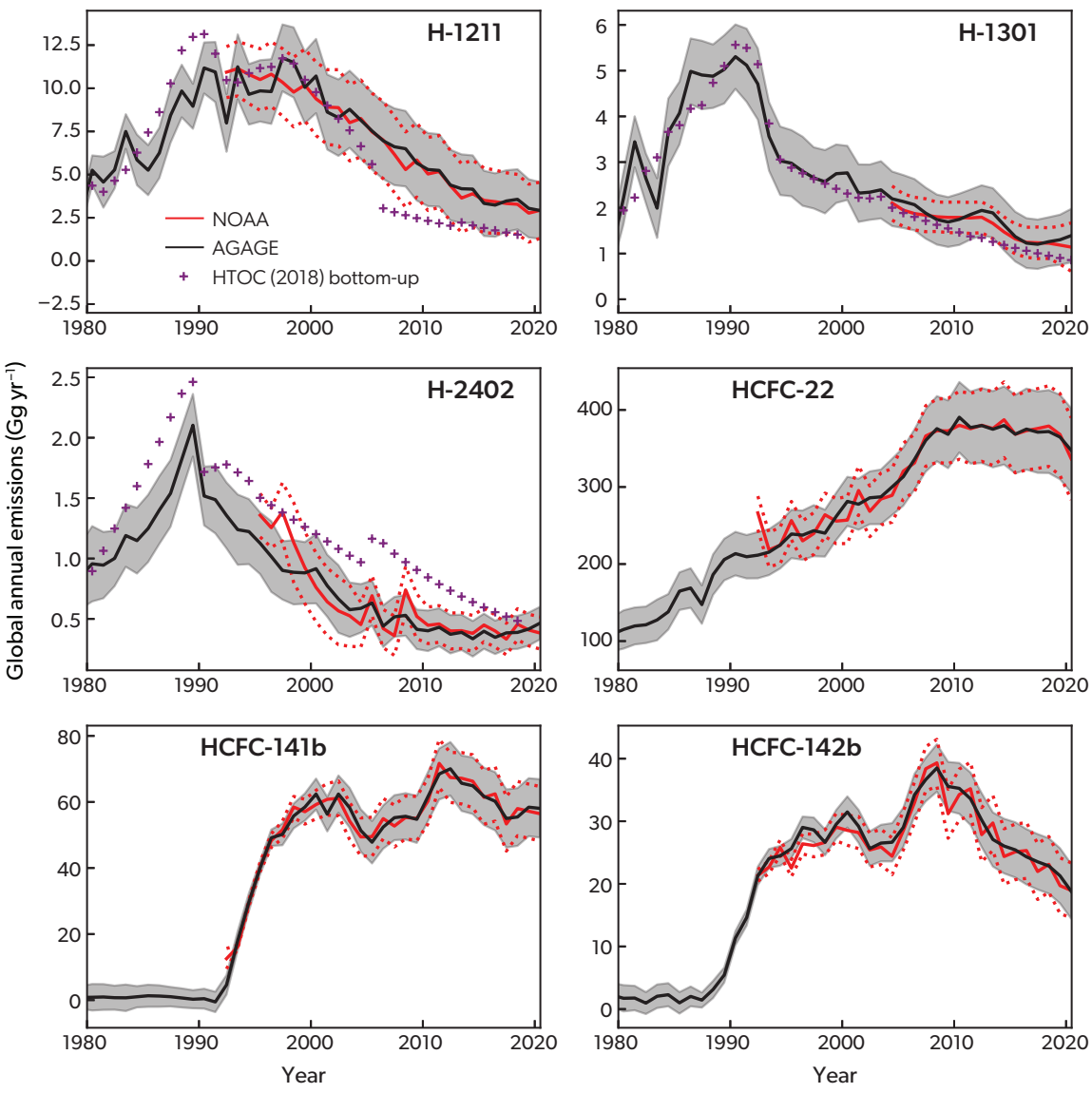

Figure 1-3. *Continued from previous page.*
Atmospheric observation-based "top-down" global emission estimates (Gg yr^{-1}) for long-lived ozone-depleting substances with equivalent chlorine at the surface greater than 1 ppt in 2020, and emission inventory-based "bottom-up" global emissions estimates for H-1211, H-1301, and H-2402. Top-down emissions were calculated using a global 12-box model and a Bayesian inverse modeling framework (Cunnold et al., 1983; Rigby et al., 2013) using atmospheric data from AGAGE (black) and NOAA (red) measurement networks. For top-down estimates, losses for CFCs were assumed to occur only in the stratosphere (but no dynamical correction to account for changes in stratosphere-troposphere fluxes, as in Montzka et al., 2021, is included here), and total lifetimes were taken from the *Annex*. For other gases, OH rate constants were taken from Burkholder et al. (2019), and stratospheric lifetimes were taken from the *Annex*, with the exception of CCl_4, which was taken from SPARC (2016) but using the oceanic lifetime from Suntharalingham et al. (2019). Global steady-state lifetimes for each species (in years) were as follows: CFC-11 (55), CFC-12 (103), CFC-113 (95), CFC-13 (640), CFC-114 (191), CFC-115 (664), CH_3CCl_3 (4.8), CCl_4 (29.9), H-1211 (16.0), H-1301 (71.8), H-2402 (28.0), HCFC-22 (11.3), HCFC-141b (8.7) and HCFC-142b (17.1). Small differences may appear between global lifetimes presented in the *Annex* and those calculated by the 12-box model due to assumed OH and model transport. The gray shading and dotted red lines show the 1-standard deviation uncertainties. The Bayesian approach uses bottom-up emissions estimates as an a priori constraint. Details of the a priori constraints used are detailed in Rigby et al. (2013), Rigby et al. (2014), Simmonds et al. (2017), Vollmer et al. (2016), and Vollmer et al. (2018), where the year-to-year prior constraint on emissions was assumed to be 20% of the maximum emissions. Uncertainties in the lifetimes are taken from SPARC (2013) and applied using the method presented in Rigby et al. (2014). Bottom-up estimates have been updated for the halons using data from HTOC (2018) and are shown as purple crosses.

Assessment, and this has continued with an estimate of 0.6 ± 0.2 Gg yr^{-1} for 2020 (update of Vollmer et al., 2018). This is contrary to the expectation of CFC-13 bank-related emissions decreasing with time.

Emissions from the combination of the CFC-114/CFC-114a isomers also plateaued in the decade leading up to 2016. Estimates for 2016 have been adjusted upwards, from 1.9 Gg yr^{-1} to 2.2 Gg yr^{-1}, which is well within the uncertainty range of ±0.9 Gg yr^{-1} and also not significantly different from the 2020 emissions of 2.6 Gg yr^{-1} (**Table 1-1**; update from Vollmer et al., 2018). Emission estimates from the independent record of Laube et al. (2016), in which the two isomers were separated, have not been updated. It should be noted, though, that the observed increases in CFC-114a abundance imply an emission increase, thus highlighting further that the sources of the two isomers are not identical.

For CFC-113a, in addition to the emission increase observed between 2009 and 2012 (to 1.7 Gg yr^{-1} in 2012–2016; Adcock et al., 2018), observations indicate that emissions have increased again since 2018, although no quantitative estimate is currently available.

An increase in the global emissions of CFC-115 to 1.14 ± 0.5 Gg yr^{-1} for 2015–2016 was reported in the previous Assessment (Vollmer et al., 2018; **Figure 1-3**). More recently, these emissions have varied within uncertainties and are estimated at 1.0 Gg yr^{-1} for 2020. As for several other CFCs, the cause of these persisting emissions remains uncertain.

Recent regional studies examining CFC emissions using atmospheric observations (i.e., top-down estimates) have focused largely on CFC-11 and CFC-12, and the reader is again referred to the *"Report on the Unexpected Emissions of CFC-11"* (WMO, 2021) for more detail. Briefly, individual studies have found that Indian and Australian emissions are thought to be negligible in comparison to the global total (Say et al., 2019; Fraser et al., 2020). In contrast, emissions of CFC-11 (and, to a lesser degree, CFC-12) from within China were found to have been substantially enhanced from 2012 to 2018, after which they declined very rapidly (Montzka et al., 2021; Park et al., 2021; Yi et al., 2021). The decline of CFC-11 emissions from eastern China, however, explain only 60 ± 30% (10 ± 3 Gg yr^{-1}) of the observed global emission decrease (Park et al., 2021). In addition to the aforementioned CFC-11 Report, Hu et al. (2022) recently examined continental-scale contributions to the increase in global CFC-11 emissions between 2012 and 2017 by inferring emissions from campaign-based observations during the HIAPER Pole-to-Pole Observation (HIPPO), the Atmospheric Tomography Mission (ATom), and NOAA's global CFC-11 measurements. They found that Asia, including temperate eastern Asia, temperate western Asia, and tropical Asia, accounted for 86 (59–115) % of the global CFC-11 emission rise between 2012 and 2017. Rust et al. (2022) also reported regional emissions of 28 halocarbons for Switzerland, but all of these are very minor in a global context (e.g., around 0.05 Gg yr^{-1} for CFC-11 in 2019), which is why we do not specifically mention this study in any of the following sections. In terms of regional emissions of CFC-12, atmospheric observations have confirmed a decrease in emissions from northeastern China from 3.3 ± 1.4 Gg yr^{-1} in 2016 to 0.5 ± 0.5 Gg yr^{-1} in 2019 (Park et al., 2021).

In summary, global emissions of most CFCs remain well below their peak levels (**Figure 1-3**), with CFC-11 (and to a lesser degree CFC-12) accelerating its decline substantially since the last Assessment and now being much closer to previous baseline scenarios. This is largely due to a recent reduction in Chinese emissions. Of note are the continuing and, in some cases, increasing emissions of several of the more minor CFCs (as evidenced by an increase in chlorine from the five increasing CFCs, from 16.0 ± 0.3 ppt in 2016 to 17.2 ± 0.3 ppt Cl in 2020), for which the only known emission regions are in eastern Asia (updates from Laube et al., 2016; Adcock et al., 2018; Vollmer et al., 2018). Total ODP-weighted emissions for all CFCs dropped from 98 ± 33 Gg yr^{-1} CFC-11-equivalent in 2016 to 77 ± 32 Gg yr^{-1} in 2020 (**Figure 1-4**).

With respect to their influence on climate, in 2020 CFCs contributed 76% of the total direct radiative forcing due to ODSs controlled under the Montreal Protocol, with a combined radiative forcing of 257 mW m^{-2} in 2020 (**Figure 1-5**). The radiative forcing due to CFCs declined by 2.6% between 2016 and 2020, driven primarily by the reduction in abundance of CFC-11 and CFC-12;

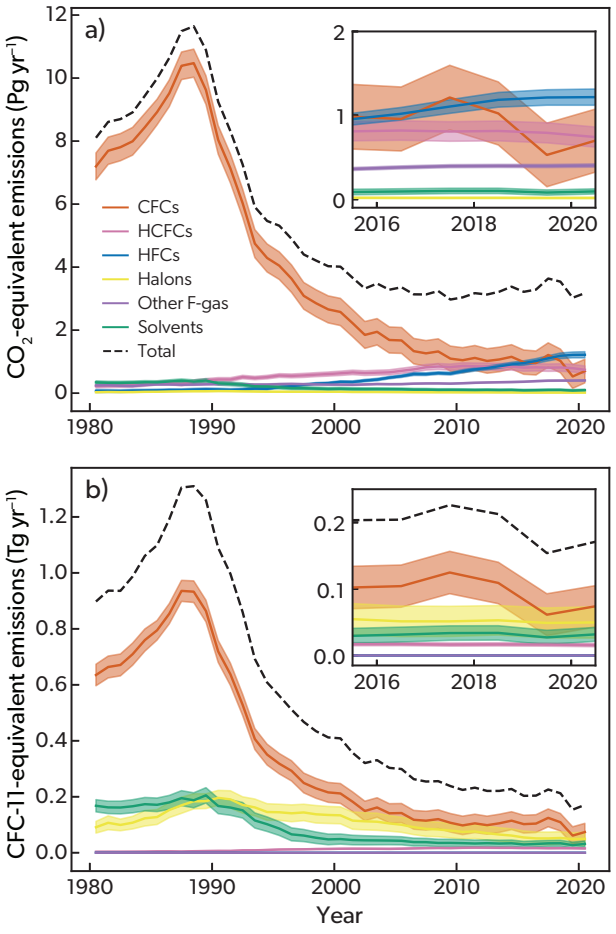

Figure 1-4. (a) 100-year GWP-weighted (CO_2-equivalent) emissions and (b) ODP-weighted (CFC-11-equivalent) emissions. CO_2- and CFC-11-equivalents are taken from the *Annex*. Solvents are defined as CCl_4 and CH_3CCl_3, and other F-gases include SF_6, CF_4, C_2F_6, C_3F_8, *c*-C_4F_8, *n*-C_6F_{14}, NF_3, and SO_2F_2 (minor species not included; see *Introduction*). Shading shows the 1-standard deviation uncertainty.

over this five-year period, the radiative forcing due to these two gases declined by 6 mW m^{-2}. Consequently, when the combined emissions of all CFCs are expressed as CO_2-equivalent, a decline has again been observed since the last Assessment (**Figure 1-4**). CO_2-equivalent emissions of CFCs were 0.9 ± 0.4 Pg yr^{-1} and 0.7 ± 0.4 Pg yr^{-1} in 2016 and 2020, respectively. This means that HFCs, which contributed 1.25 ± 0.10 Pg yr^{-1} in 2020, are now the highest contributor among the halogenated species in terms of CO_2-equivalent emissions in 2020 (see also *Chapter 2*). Where available, CO_2-equivalent emissions of individual species for 2020 can be found in **Table 1-1**.

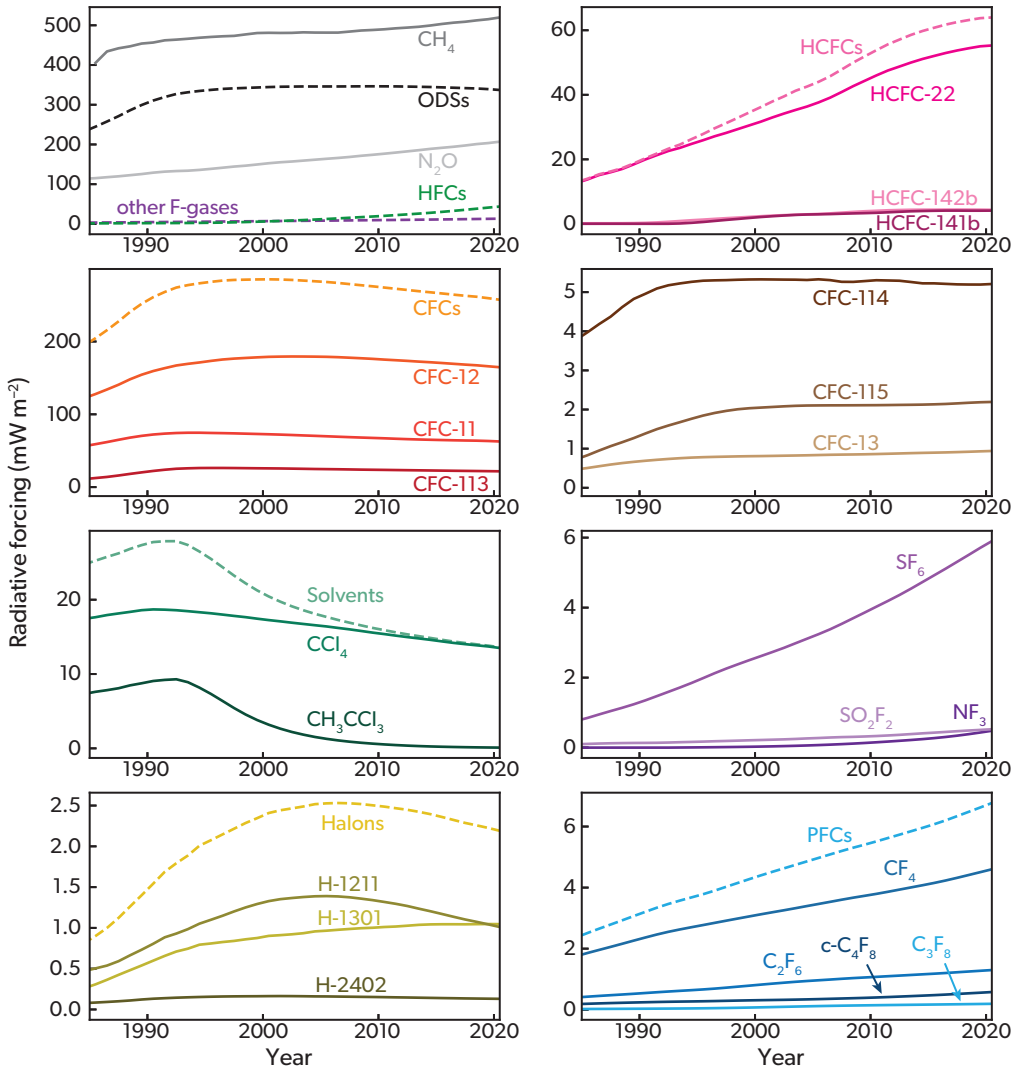

Figure 1-5. Direct radiative forcing based on the lower-tropospheric atmospheric mole fractions of ODSs and selected greenhouse gases, if their radiative forcing in 2020 was 0.1 mW m^{-2} or higher. Groupings of gases are shown with dashed lines, and selected compounds are shown with solid lines. The ODS group here refers to combined CFCs, HCFCs, halons, and solvents (minor species not included; see *Introduction*). HFCs include the species HFC-23, HFC-32, HFC-134a, HFC-143a, HFC-125, HFC-152a, HFC-4310mee, HFC-227ea, HFC-365mfc, HFC-236fa, and HFC-245fa. Other F-gases are defined as the sum of PFCs, SF_6, SO_2F_2, and NF_3. Radiative forcings for individual HFCs are not shown as these can be found in *Chapter 2*. Individual lines for HCFC-124 and *n*-C_6F_{14} have been omitted for clarity. The radiative forcing for CH_3CCl_3 in 2020 is less than 0.1 mW m^{-2} but has been included due to historical significance. Lower tropospheric annual mean mole fractions were taken from merged NOAA, AGAGE, and UEA/FZJ data. Radiative forcings are calculated following the approach of Ramaswamy et al. (2001) using the radiative efficiencies from the *Annex*. Preindustrial (in 1750) mole fractions are assumed to be zero for all gases except for CH_4 (722 ppb), N_2O (270 ppb), and CF_4 (40 ppt). For comparison, the radiative forcing due to CO_2 was approximately 2111 mW m^{-2} in 2020 (Butler and Montzka, 2021).

Box 1-2. Uncertainties in Atmospheric Observation-Based Emission Estimates

Uncertainties in atmospheric observation-based global emission estimates

Global emissions of a trace gas can be derived from the annual rate of change in its atmospheric burden and its atmospheric lifetime, as described in detail in the last Assessment. Uncertainties in such estimates are often dominated by uncertainties of the atmospheric lifetime of the trace gas. Atmospheric lifetimes for the majority of trace gases considered in this Assessment were inferred from satellite observations, in situ measurements of tracer-tracer correlations, photochemical model simulations, and estimates of oceanic and terrestrial fluxes. Uncertainties in atmospheric lifetimes for many trace gases considered here are on the order of ±10% to ±30%.

In addition to atmospheric lifetimes, uncertainties of atmospheric burdens (B) also contribute to the overall uncertainty of such global emission estimates. B is generally estimated from the NOAA and AGAGE atmospheric mole fraction measurements made near Earth's surface in locations that are far away from emissive sources, so that the measured mole fractions are deemed as good representations of zonal average tropospheric mole fractions at measurement locations. However, the representativeness of those surface measurements for zonal averages is an additional factor that can augment inaccuracies in global means derived from a small number of remote surface sites. Furthermore, the Quasi-Biennial Oscillation (QBO) of tropical zonal winds, previously known as a climate phenomenon that strongly affects the variability of trace gas concentrations in the stratosphere, can also influence trace gas levels at Earth's surface (Ray et al., 2020; Montzka et al., 2021; Ruiz et al., 2021). This influence is on one- to five-year timescales and can impact global annual emission estimates. However, when averaging global annual emissions over five years or more, the impact of QBO on the multiyear global average emission estimate is reduced.

In this Assessment, global emissions of ODSs (and of HFCs, discussed in *Chapter 2*) are derived from the AGAGE 12-box model (Cunnold et al., 1994; Rigby et al., 2013) rather than a one-box model. Because the transport in the 12-box model relies on parameterized mixing and advection between boxes, additional uncertainties of global emissions from this approach arise from uncertainties in the parameterized transport in the 12-box model.

Uncertainties in atmospheric observation-based regional emission estimates

Atmospheric observation-based regional emission estimates compiled in this Assessment are mostly derived from Bayesian inverse modeling of regional atmospheric trace gas mole fraction measurements. The fundamental assumption in this modeling technique is that there is a linear relationship between regional emissions (s) and enhancements (z) in mole fractions measured within or closely downwind of this region. This linear operator, or the sensitivity of these atmospheric observations to upwind emissions (H), is often computed from atmospheric transport models. The Bayesian technique requires an initial guess on regional emissions (a priori, s_p). It assumes errors between the prior guess and the unknown "true" emissions (or prior emission errors) and errors between observed mole fraction enhancements and simulated mole fraction enhancements with the chosen transport model (or model-observation mismatch errors) follow Gaussian distributions. The Bayesian solution of regional emissions was obtained by minimizing the following cost function (L), such that it reflects the most likely magnitudes and distributions of regional emissions, given the observed mole fraction enhancements in space and time, prior emission assumptions, and atmospheric transport simulations.

$$L = \frac{1}{2}(z - Hs)^T R^{-1}(z - Hs) + \frac{1}{2}(s - s_p)^T Q^{-1}(s - s_p)$$

Here, R and Q represent the covariance matrices of model-observation mismatch errors and prior emission errors.

The first order of uncertainties in such estimates originate from biases in atmospheric transport simulations, assumptions in prior emissions, and the estimated upwind boundary values that were subtracted from atmospheric observations to derive regional mole fraction enhancements. To incorporate such uncertainties into regional emission estimates, some atmospheric inversion analyses implement an ensemble approach, where multiple transport simulations, prior emissions, and boundary value estimates are considered (e.g., Hu et al., 2017; Rigby et al., 2019; Park et al., 2021). The range of emissions derived from these multiple inversion runs are used for calculating the final mean and uncertainties of regional emissions.

The locations, density, and frequency of atmospheric trace gas measurements used for deriving regional emissions also contribute to the overall uncertainties of regional emission estimates. In general, more measurements within and closely downwind of emissive regions will enable a more accurate inference of regional emissions that have less dependence on prior assumptions. For example, the current atmospheric sampling network has a good sensitivity for emissions from North America, western Europe, and eastern Asia (**Box 1-2 Figure 1**), enabling robust estimates of regional emissions from such an approach (Graziosi et al., 2015; Hu et al., 2015, 2016, 2017; Maione et al., 2014; Park et al., 2021; Rigby et al., 2019; Simmonds et al., 2020). In contrast, huge gaps exist in many developing countries (Weiss et al., 2021), resulting in challenges in understanding their contributions to global emissions of important controlled substances and their compliance to the Montreal Protocol.

Besides the factors mentioned above, assumptions about error covariances in prior emissions and model–observation mismatch errors (Q and R in the equation above) also influence the final Bayesian solution of emissions. This is because these assumptions determine the relative weights between atmospheric observations and prior emission assumptions in the final solution. In the early

Bayesian regional inversion studies, scientists often used "expert judgment" to arbitrarily assign error covariance matrices, whereas recent techniques (Ganesan et al., 2014; Hu et al., 2015; Lickley et al., 2021) allow direct quantification of error covariances from atmospheric observations, enabling a more objective derivation of regional emissions.

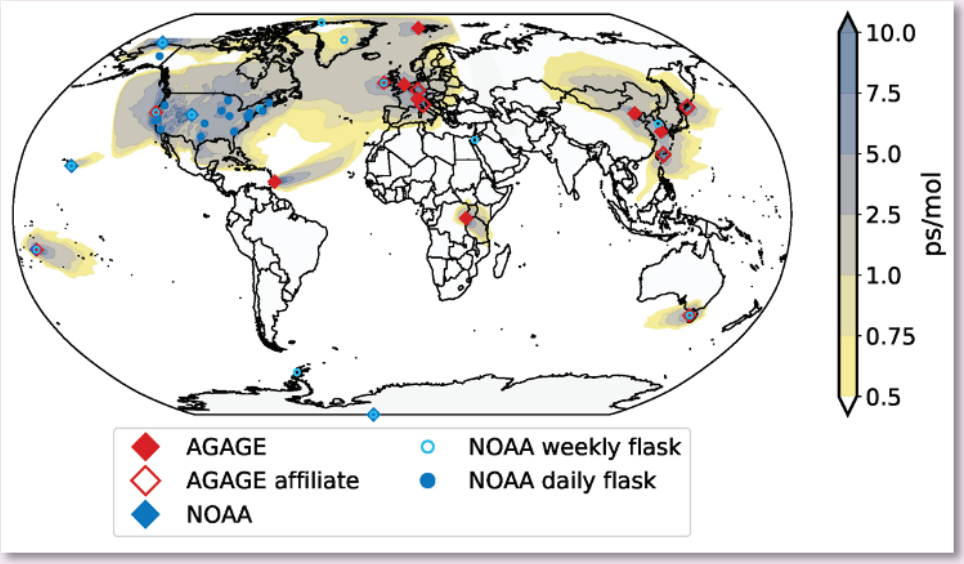

Box 1-2 Figure 1. Current atmospheric sampling for measurements of ozone-depleting substances and their substitutes from the NOAA and AGAGE networks. Displayed in color shading are mean footprints, which are a measure of the contribution to the above-baseline mole fraction made by a unit emission. [Figure from WMO, 2021.]

1.2.2 Halons

Observations of Atmospheric Abundance. Halon-1211 ($CBrClF_2$), halon-2402 ($CBrF_2CBrF_2$), and halon-1202 (CBr_2F_2) abundances continued to decline from their peak values, which were observed in the early and mid-2000s. Global surface mean mole fractions of approximately 3.2 ppt and 0.40 ppt were observed for halon-1211 and halon-2402, respectively, in 2020, and SH mole fractions of approximately 0.009 ppt were recorded for halon-1202 (**Table 1-1** and **Figure 1-1**; updates from Newland et al., 2013; Vollmer et al., 2016). Halon-1301 ($CBrF_3$) growth rates, which were reported as <0.01 ppt yr^{-1} in 2016, remained close to zero. A 2020 global mean mole fraction of 3.37 ppt and 3.32 ppt was derived from AGAGE and NOAA, respectively, which means that halon-1301 has now become the most abundant halon in the atmosphere. Abundances of halon-2311 ($CF_3CHBrCl$) remained below 0.01 ppt.

Emissions, Lifetimes, and Radiative Forcings. Emissions of halon-1211 estimated from observed atmospheric abundances show signs of a continuing decline since the last Assessment, from 3.3 ± 1.8 Gg yr^{-1} in 2016 to 2.9 ± 1.6 Gg yr^{-1} in 2020. These top-down estimates continue to be higher than the bottom-up emission estimates in the *Halons Technical Options Committee 2018 Assessment Report* (HTOC, 2018; **Figure 1-3**). For halon-2402, emissions remain low at around 0.4 Gg yr^{-1}, with no indications of a change since 2016. There is now good agreement with HTOC-based bottom-up estimates for this ODS, as the latter declined substantially between 2016 and 2020. Halon-1301 emissions have also remained stable at around 1.3 Gg yr^{-1} during 2016–2020, with HTOC estimates slightly lower than those based on atmospheric observations. No update is available for halon-1202 and halon-2311, although the most recently reported mole fractions (<0.01 ppt in both cases) indicate that the contributions from these two species are likely small.

Halons have high ODPs, so as a group their ODP-weighted emissions still make the second-highest contribution to CFC-11-equivalent emissions relative to those of other ODS groups (**Figure 1-4**). Due to their low GWPs, the direct contribution of halons to global radiative forcing is small. At 2.2 mW m^{-2} in 2020, halons contribute only 0.6% of the radiative forcing of CFCs (**Figure 1-4**). When their influence on ozone depletion is also considered, net radiative forcing due to halons is negative (Daniel et al., 1995).

1.2.3 Carbon Tetrachloride (CCl_4) and Methyl Chloroform (CH_3CCl_3)

Observations of Atmospheric Abundance. The abundance of carbon tetrachloride (CCl_4) has continued to decline at a rate similar to that reported in the previous Assessment. AGAGE observations showed a mole fraction of 79.9 ppt in 2016 and 76.3 ppt in 2020, while NOAA reported a mole fraction of 81.3 ppt in 2016 and 77.1 ppt in 2020 (**Table 1-1** and **Figure 1-1**). These differences are likely related to known calibration-scale differences, although a higher discrepancy between inter-hemispheric differences derived from observations by the two networks has emerged since around 2018 (**Figure 1-1**). Data from UCI show a similar decline, from 81.9 ppt to 77.4 ppt, between these years. Ground-based remote sensing observations of CCl_4 from Jungfraujoch also show a very similar rate of decline between

2014 and 2020 as compared to the average of the global surface-based measurements from the AGAGE and NOAA networks (**Table 1-2**).

Methyl chloroform (1,1,1-trichloroethane, CH_3CCl_3) global mean mole fractions decreased from 2.6 ± 0.7 ppt in 2016 to 1.4 ppt in 2020 (**Table 1-1**), i.e., reaching 1% of its maximum value. This is reflected also in long-term atmospheric CH_3CCl_3 measurements at seven background stations in China and confirmed by a record of 12 years showing a continuous decline (Yu et al., 2020).

Emissions, Lifetimes, and Radiative Forcings. Since the last Assessment, Suntharalingam et al. (2019) reevaluated the partial lifetime of CCl_4 with respect to the ocean sink and derived an estimate of 124 (110–150) years. This is shorter than the previously used estimate of 183 (147–241) years (Butler et al., 2016) and implies higher emissions of 5–7 Gg yr^{-1}. Given the numerous improvements in the methodology of the new study, the revised partial lifetime has been incorporated into emission estimates in this Assessment. One further study examined the atmospheric lifetime of CH_3CCl_3 (Orkin et al., 2020), but its main focus was on improving estimations of the atmospheric lifetimes of other species using an improved scaling method in combination with modeling and kinetic data. They derive a partial lifetime of 6.0 years with respect to loss from reaction with the OH radical, but this is only slightly lower than, and not significantly different from, the currently used 6.1 years (Engel, Rigby et al., 2018).

Global emissions of CCl_4 are estimated at 44 ± 14 Gg yr^{-1} in 2020, virtually unchanged from the estimate of 43 ± 15 Gg yr^{-1} during 2016. As noted by Liang et al. (2016) and in the previous Assessment, there are still indications for a gap between bottom-up (based on emissions reporting) and atmospheric observation–derived emissions. This gap is discussed further in *Chapter 7*, although it should also be noted that the uncertainty ranges of the two emission estimates currently overlap (**Table 1-1**). As for regional estimates, emissions of CCl_4 in eastern China over the period 2013–2019 show year-to-year variability likely related to CFC-11 production (which is not surprising as CCl_4 is a feedstock for CFC-11 production). Emissions were found to have increased after 2013, reaching 11.3 ± 1.9 kt yr^{-1} in 2016, and to have then decreased to 6.3 ± 1.1 kt yr^{-1} in 2019 (Park et al., 2021).

CH_3CCl_3 emissions are stable at about 2.3 Gg yr^{-1} in 2020, although there are differences in the emissions reported for 2016 between the AGAGE (2.2 Gg yr^{-1}) and NOAA networks (2.9 Gg yr^{-1}). However, when considering the uncertainty ranges, the 2016 and 2020 emission estimates are indistinguishable (**Table 1-1**). In terms of regional studies, Say et al. (2019) derived CCl_4 emissions of 2.3 (1.5–3.4) Gg yr^{-1} and CH_3CCl_3 emissions of 0.07 (0.04–0.10) Gg yr^{-1} for northern and central India during an aircraft campaign in June and July 2016. The studies focusing on China report a temporal evolution of CCl_4 emissions similar to those of CFC-11 and CFC-12, with an increase from about 2012 onwards, followed by a decrease that started approximately during 2016–2017, and 2019 emissions being comparable to those in 2011 (Lunt et al., 2018; Park et al., 2021).

Radiative forcing due to CCl_4 declined to 13 mW m^{-2} in 2020, equivalent to 5% of the radiative forcing due to CFCs. The radiative forcing due to CH_3CCl_3 remains negligible (**Figure 1-4**).

1.2.4 Hydrochlorofluorocarbons (HCFCs)

Observations of Atmospheric Abundance. The global surface mean mole fraction of HCFC-22 ($CHClF_2$) has continued to increase, from around 237 ppt in 2016 to around 248 ppt in 2020 (**Figure 1-1** and **Table 1-1**). However, its annual growth rate has decreased even further and is now about 0.5% (2019–2020) as compared to 1.8% in 2015–2016. In contrast, growth rates of HCFC-141b (CH_3CCl_2F) and HCFC-142b (CH_3CClF_2) have not continued their decline since 2016 (**Figure 1-1**). Their global abundances were 24.5 ppt and 22 ppt in 2016, respectively; i.e., within uncertainties they are identical to the 2020 values. Nevertheless, higher growth rates of these three HCFCs had been projected in the previous two Assessments, which is reflected in the higher abundances in the A1-2014 and A1-2018 scenarios (**Figure 1-1**). These near-surface observations of abundances are in excellent agreement with FTIR-based abundances and trends (**Figure 1-2** and **Table 1-2**; Prignon et al., 2019), whereas upper-tropospheric trends derived from the ACE-FTS satellite instrument are lower (HCFC-141b) or higher (HCFC-142b) than the other available trend estimates. It should be noted, however, that no comprehensive uncertainty analysis has been carried out for these satellite-based trends.

Of the less abundant HCFCs, mole fractions of HCFC-124 ($CHClFCF_3$) were not reported in the last Assessment. These have since become available, changing from 1.1 ppt in 2016 to 0.9 ppt in 2020 (update from Simmonds et al., 2017). Vollmer et al. (2021) reported in situ observations of the newly detected HCFC-132b ($CH_2ClCClF_2$), which included a reconstruction of its historical atmospheric trends and abundances. This ODS first appeared in the atmosphere during the late 1990s, exhibiting a growth period until 2013, reaching 0.15 ppt in the NH. A brief period of decline was followed by another increase from around 2016 onwards to arrive at a global mole fraction of 0.14 ppt in 2020.

HCFC-133a (CF_3CH_2Cl) SH mole fractions remained stable at around 0.39 ppt between 2016 and 2020 (update from Laube et al., 2014) and globally were at 0.45 ppt in 2020. The abundances of HCFC-31 (CH_2ClF) increased slightly from 0.09 ppt in 2016 to 0.11 ppt in 2020 (update from Vollmer et al., 2021). No update is available for HCFC-225ca ($CF_3CF_2CHCl_2$), which in 2012 was reported at 0.02 ppt.

Emissions, Lifetimes, and Radiative Forcings. Global emissions of HCFC-22 may have started to decline in 2020 after a period of relatively constant emissions, with 2020 emissions of 348 ± 53 Gg yr^{-1} and 337 ± 53 Gg yr^{-1} inferred using AGAGE and NOAA measurements, respectively, compared to 2016 emissions of 375 ± 50 Gg yr^{-1} and 373 ± 51 Gg yr^{-1}, respectively. HCFC-142b emissions show indications of a decline by a total of 5–6 Gg (22–25%) between 2016 and 2020, though the uncertainties of the estimates for these two years overlap. HCFC-142b emissions in 2020 were around 19 Gg yr^{-1}. Global emissions of HCFC-141b of 58.1 ± 8.8 Gg yr^{-1} and 56.4 ± 8.2 Gg yr^{-1} from AGAGE and NOAA respectively in 2020 were smaller than in 2016, although, after an initial drop, emissions rose year on year since 2017, amounting to a total rise of ~4.5 Gg. Again, this is not a significant increase when considering the uncertainties (**Table 1-1**). However, the emission changes for those three HCFCs are consistent with a sharp drop in reported HCFC consumption after 2012, particularly from Article 5 countries. Emissions of HCFC-124 have continued to decline since 2016, with 2020 emissions of 3.0 ± 0.7 Gg yr^{-1}. The 2020 emissions were, however, slightly larger (up to ~0.4 Gg yr^{-1}) than those in the three preceding years.

A number of HCFCs with no known purposeful end use

Table 1-3. Regional emissions estimates for HCFCs (mainly focusing on new estimates published since the last Assessment) for years where data are available. Uncertainties are given as the 68% uncertainty range or 1 standard deviation where available. Note that some estimates of HCFC-22, HCFC-141b, HCFC-142b, and HCFC-124 emissions are derived using a bottom-up method, while other estimates use a top-down approach. Estimates for India use measurements made only during June and July.

Region	Year									
	2011	2012	2013	2014	2015	2016	2017	2018	2019	2020
HCFC-22 (Gg yr^{-1})										
China[a]	139 ± 35	154 ± 51	172 ± 37	159 ± 34	146 ± 44	147 ± 36	147 ± 26			
China[b*]	107 (79–129)	116 (87–142)	112 (91–153)	127 (95–161)	130 (124–131)	134 (127–135)	131 (124–135)	126 (116–132)	121 (108–131)	116 (100–130)
Europe[c*]	18.6	16.1								
Europe[c]	15.2 ± 3.1	12.1 ± 2.0								
India[d]						7.8 (6.0–9.9)				
South Africa[e]							3.0 (1.6 – 4.4)			
USA[f]	48.8 ± 9.4	42.8 ± 3.1	41.1 ± 4.4	40.0 ± 5.9						
USA[g*]	80	76	73	69	58	54	51	47	43	
HCFC-141b (Gg yr^{-1})										
China[a]	24 ± 5	22 ± 6	18 ± 6	16 ± 7	15 ± 6	15 ± 3	15 ± 2			
China[h]	13.1	14.3	14.2	15.7	15.5	10.3	10.6	11.6	10.9	
China[i*]	15.3	16.4	15.8	15.7	17.4	18.4	20.0	23.1	23.6	24.0
India[d]						1.0 (0.7–1.5)				
HCFC-142b (Gg yr^{-1})										
China[a]	11 ± 3	11 ± 4	11 ± 4	11 ± 3	9 ± 3	8 ± 2	6 ± 1			
China[h]	10.8	13.4	12.8	11.4	8.1	7.2	6.5	5.8	6.0	
China[i*]	12.7	14.6	12.3	12.1	12.6	12.6	12.5	12.2	11.9	11.7
India[d]						0.10 (0.06–0.14)				

*Bottom-up; [a] Fang et al. (2019c); [b] Li et al. (2016); [c] Graziozi et al. (2015); [d] Kuyper et al. (2019) [e] Say et al. (2019); [f] Hu et al. (2017); [g] US EPA (2021); [h] Yi et al. (2021); [i] Wang et al. (2015); [j] Han et al. (2014)

continue to be emitted. Emissions of HCFC-133a remained at around 2 Gg yr^{-1} between 2017 and 2020 (update from Vollmer et al., 2021), which follows emissions of 2.8 ± 0.4 Gg yr^{-1} in 2016. HCFC-31 emissions between 2018 and 2020 were around 1 Gg yr^{-1}, following a rise from 0.9 ± 0.2 Gg yr^{-1} to 1.3 ± 0.2 Gg yr^{-1} between 2016 and 2017. The newly discovered HCFC-132b reached an all-time high in emissions in 2020 of 1.2 ± 0.5 Gg yr^{-1}, up from 0.8 ± 0.3 Gg yr^{-1} in 2016.

Regional emission estimates of the three most abundant HCFCs are summarized in **Table 1-3**. A top-down study of India's HCFC emissions was carried out using measurements made during an aircraft campaign in June and July 2016 (Say et al., 2019). Measurements included HCFC-22, HCFC-141b, and HCFC-142b. The derived emissions were extrapolated to the whole of 2016, and show that India was reportedly responsible for 2.1% (1.6–2.7%, one standard deviation) of global HCFC-22 emissions. In contrast, India was estimated to be responsible for 7% of global HCFC-22 production in 2017 (Stanley et al., 2020), making it one of the primary global HCFC-22 manufacturers at the time. The relative contribution of India to global emissions is smaller for the other two HCFCs, at 1.8 (1.2–2.6) % of HCFC-141b and 0.4 (0.2–0.6) % of HCFC-142b.

The first top-down HCFC-22 emission estimates from Africa, using the first high-frequency halocarbon measurements made on the continent, show that South African emissions in 2017 were 3.0 (1.6–4.4) Gg yr^{-1} (Kuyper et al., 2019), around 40% of those estimated from India in the previous year.

Recently published top-down emissions estimates for China show that HCFC-22 emissions peaked at 172 ± 37 Gg yr^{-1} in 2013, although there was no statistically significant increase or decrease in emissions over the period 2011–2017 (Fang et al., 2019c). These estimates are generally in agreement with bottom-up emission estimates for China (Li et al., 2016), although uncertainties are comparably large. A reported rise in global HFC-23 emissions (Stanley et al., 2020; see *Chapter 2* for more details) has been linked to HCFC-22 production (as a by-product) in developing countries. There was previously a reported discrepancy (of ~23 Gg yr^{-1} in 2014, Hu et al., 2017) between top-down and bottom-up derived emissions in the United States; it is currently not known whether this persisted after 2014.

Top-down emission estimates of HCFC-141b in China declined from 24 ± 5 Gg yr^{-1} in 2011 to 15 ± 2 Gg yr^{-1} in 2017, and emissions of HCFC-142b declined from 11 ± 3 Gg yr^{-1} in 2011 to 6 ± 1 Gg yr^{-1} in 2017 (Fang et al., 2019c). A separate study, using an interspecies-correlation method (Yi et al., 2021, correlated to HCFC-22), also shows a decline in China's HCFC-141b emissions from 13.1 Gg yr^{-1} in 2011 to 10.9 Gg yr^{-1} in 2019 (peaking at 15.7 Gg yr^{-1} in 2015), and a decline in emissions of HCFC-142b from 10.8 Gg yr^{-1} in 2011 to 6.0 Gg yr^{-1} in 2019 (peaking at 13.4 Gg yr^{-1} in 2012), though not all of China's industrial centers are covered. From 2016 onwards, top-down estimates of HCFC-142b are significantly smaller than those projected using bottom-up methods (i.e., in Han et al., 2014, by around 50%), whereas prior to 2016 the top-down and bottom-up estimates were all in good

agreement. The top-down estimates for HCFC-141b in China generally show a decline in emissions. However, a bottom-up estimate projected that those emissions should increase by 6.6 Gg yr^{-1} between 2015 and 2020 (Wang et al., 2015).

HCFC-124 emissions in China are estimated to have remained largely constant between 2011 and 2017 at around 0.8 Gg yr^{-1} (Fang et al., 2019c), with no statistically significant year-to-year variation. Emissions of two minor HCFCs, HCFC-133a and HCFC-132b, were shown to originate almost entirely from East Asia, and since 2016 the majority of these have been emitted from eastern China (Vollmer et al., 2021).

Emissions of all HCFCs, in terms of their combined CFC-11-equivalent, have continued to decline since 2016, supporting the previous Assessment's suggestion that the 2007 adjustment to the Montreal Protocol has been effective in limiting HCFC emissions. The 2020 CFC-11-equivalent emissions of HCFCs (16 ± 3 Gg CFC-11 yr^{-1}) are only around 21% of those from CFCs.

A similar decline has continued for the HCFCs in terms of their combined CO_2-equivalence. HCFC emissions were 0.7 Pg CO_2-equivalent yr^{-1} in 2020, similar to those from CFCs. Radiative forcing for all HCFCs remains dominated by HCFC-22, which contributed 86% of HCFC radiative forcing in 2020. Overall radiative forcing for HCFCs has risen by 4% since 2016 and is, at 64.0 mW m^{-2}, equivalent to 25% of the forcing of CFCs in 2020.

1.2.5 Methyl Chloride (CH_3Cl)

Observations of Atmospheric Abundance. CH_3Cl is not controlled under the Montreal Protocol and is largely natural in origin, although some direct (feedstock, coal combustion; e.g., Li et al., 2017) and indirect (biomass burning; e.g., Mead et al., 2008) anthropogenic sources are known. The 2020 global mean mole fraction determined from the AGAGE and NOAA global networks was 546 and 549 ppt, respectively (**Table 1-1**). These values are around 1–2% lower than the 2016 values reported in the previous Assessment, and changes of this magnitude are well within historically observed variability since ongoing measurements commenced in the 1990s (**Figure 1-1**). It should be noted, though, that observations of CH_3Cl abundances in the upper troposphere have repeatedly shown that the global values from ground-based networks may represent an underestimation by approximately 50–100 ppt of the amount of CH_3Cl entering the stratosphere (Umezawa et al., 2014, 2015; Adcock et al., 2021). This may be related to the nature of some of its sources (and also its terrestrial sink), as biomass burning tends to lift air rapidly, and many emissions in the tropics and in the source regions near the Asian monsoon (i.e., two main input regions for air to the stratosphere) are not well captured due to the locations of the network stations (see also **Box 1-2**).

Emissions, Lifetime, and Radiative Forcing. Global emissions of CH_3Cl are estimated at around 4.7 Tg yr^{-1} both in 2016 and 2020. In terms of regional emission estimates, anthropogenic emissions from China were previously estimated to average 363 ± 85 Gg yr^{-1} between 2008 and 2012 (Li et al., 2017), equivalent to about 7% of current global emissions. More recent evidence linked some of these emissions directly to iron and steel industrial processes, as unexpectedly high concentrations were found to be emitted in the sintering processes (Ding et al., 2020). Another study reported that based on new kinetic isotope measurements of the main sink reactions of CH_3Cl in combination with modeling, the tropical rainforest source of this gas might be much smaller than previously believed, i.e., 670 ± 200 Gg yr^{-1} instead of around 2 Tg yr^{-1} (Bahlmann et al., 2019). This would in turn mean that a major CH_3Cl source is missing.

In terms of regional emissions, southwest South African emissions were estimated for the first time by an observation-based study at 9.7 (6.0–13.5) Gg yr^{-1} during 2017 by Say et al. (2020). In a more process-oriented study, Macdonald et al. (2020) reported consumption of CH_3Cl from the forefield of a retreating Arctic glacier, although this is unlikely to be a significant sink, given the relatively small fluxes and surface area. This could, however, be of future importance as the Arctic is one of the most rapidly warming regions of the Earth, and this additional sink process might become more significant. Other recently reported minor

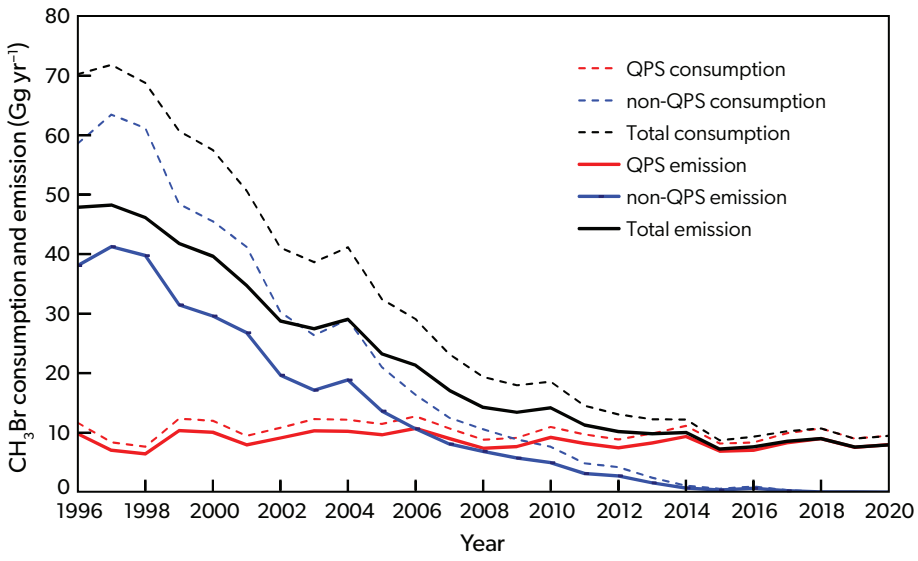

Figure 1-6. CH_3Br consumption (dashed lines), as reported in the UNEP database (UNEP, 2022), for non-QPS uses (blue) and QPS uses (red), and emissions (solid lines) from non-QPS uses (blue) and QPS uses (red). Total consumption and emissions are shown as black dashed and solid lines, respectively. As in previous Assessments, soil fumigation emission rates are estimated as 65% of reported consumption, and QPS emission rates are estimated as 84% of reported consumption (based on UNEP, 2006, where uses are weighted averages with mean emission factors and the smallest non-QPS source, i.e., soil injection without a tarp, is removed from the calculation).

or unquantified sources of CH_3Cl include tropical mangroves (4–7 Gg yr^{-1}; Koluso et al., 2018), rapeseed crops (~5 Gg yr^{-1}; Jiao et al., 2020), advancing saltmarsh due to sea level rise (with the nearby degraded forest wetland acting as a net sink; Jiao et al., 2018), animal excrements on coastal Antarctic tundra soils (with those soils otherwise acting as a sink; Zhang et al., 2020), and copper-based chemical usage (2.5 ± 0.7 Gg yr^{-1}; Jiao et al., 2022).

With regard to its direct influence on anthropogenic-induced global warming, the effect from CH_3Cl emissions on climate is small relative to other long-lived halogenated gases due to its very low radiative impact (GWP-100 of 5.54; Smith et al., 2021) and large natural emissions contributing to its current abundance.

1.2.6 Methyl Bromide (CH_3Br)

Observations of Atmospheric Abundance. CH_3Br has the shortest atmospheric lifetime of all the controlled ODSs in this chapter (*Annex*), and its 2020 global mean surface mole fractions from the AGAGE and NOAA networks, respectively, were 6.52 ppt and 6.68 ppt (**Figure 1-1** and **Table 1-1**). This is about 30% lower than the peak observed between 1996 and 1998 and around 20% higher than the preindustrial SH mole fraction of 5.5 ± 0.2 ppt derived from ice core measurements (Carpenter, Reimann et al., 2014). The global mean mole fraction had briefly grown around 2015–2016, but subsequently reverted to a slow decrease until about 2017, followed by a period with little overall change. The 2020 global CH_3Br abundances were 0.33 ppt (AGAGE) or 0.17 ppt (NOAA) lower than the 2016 value of 6.85 ppt. The cause of these difference between the networks is unclear, but it could arise from the various source and sink processes of this ODS and the partly different locations of the observing sites for these networks, in combination with its relatively short atmospheric lifetime causing a less even distribution throughout the global troposphere. It should also be noted that a comparison with 2016 global mole fractions is somewhat misleading, as abundances in 2014 and 2015 were considerably lower (between 6.5 and 6.6 ppt, respectively), resulting in, e.g., no significant decrease when comparing abundances in 2015 and 2020.

Emissions, Lifetime, and Radiative Forcing. Global CH_3Br emissions were relatively unchanged between 2016 (135 ± 21 Gg yr^{-1}) and 2020 (131 ± 20 Gg yr^{-1}; **Table 1-1**). This ODS is emitted by both natural and anthropogenic sources, including biomass and biofuel burning, oceanic emissions, fumigation, crops, and other vegetation (e.g., Montzka et al., 2003; Deventer et al., 2018; Jiao et al., 2020; Nicewonger et al., 2022). Among the anthropogenic sources, the fumigation of soils, post-harvest storage of commodities, and the fumigation of structures are controlled under the Montreal Protocol. Production of CH_3Br for use in quarantine and pre-shipment (QPS) for pest control in the transport of agricultural products, on the other hand, is exempt from the phaseout. The non-QPS consumption (i.e., other usage) dropped to 0.01 Gg in 2019, around 0.03% of its peak value (UNEP, 2022; **Figure 1-6**).

The reported consumption for QPS had been relatively stable for about two decades, from 1996 to 2016, as discussed in the previous Assessment. The temporal evolution between 2016 and 2020 was similar, with increases from about 8.2 Gg yr^{-1} in 2015 to about 10.7 Gg yr^{-1} in 2018, followed by a slight drop to 9.5 Gg in 2020 (**Figure 1-6**). These relatively small fluctuations in reported consumption cannot explain the observed slowdown in the decline rates of both atmospheric mole fraction and IHD as observed by both the AGAGE and NOAA networks (**Figure 1-1**).

In terms of regional emissions, CH_3Br from eastern China has been reported to have remained relatively constant at 4.1 ± 1.3 Gg yr^{-1} for the period 2008–2019 (Choi et al., 2022). The estimated emissions peaked in 2010 at 7.1 ± 1.3 Gg yr^{-1} and then decreased to 2.4 ± 1.3 Gg yr^{-1} in 2012, followed by a small positive trend in later years. This slight increase from 2014 to 2018 seems to reflect the impact of increased QPS use in traded commodities as reported to UNEP. There was, however, a significant discrepancy of 2.9 ± 1.3 Gg yr^{-1} on average between the observation-inferred estimates and bottom-up emission estimates based on the consumption data reported to UNEP in 2008–2019. After the potential contributions of the rapeseed industry and biomass burning were assessed, the remaining discrepancy of about 1.4 Gg yr^{-1} is likely due to fumigation use that was not reported and/or inaccurately reported, or to emissions from unknown sources in eastern China.

As for recent vegetation-focused emission studies, several smaller sources have been investigated or revisited. Deventer et al. (2018) estimated the global salt marsh source to be 1.0 to 7.8 Gg yr^{-1}, based on a latitudinal examination of all the published salt marsh studies, while Jiao et al. (2020) reassessed the global source from rapeseed, downscaling the prior estimate of 5.2 Gg yr^{-1} to 2.8 ± 0.7 Gg yr^{-1}. Advancing salt marshes due to sea level rise do not seem to change CH_3Br emissions (Jiao et al., 2018), which is in contrast to emissions of CH_3Cl. In addition, Jiao et al. (2022) reported CH_3Br production induced by Cu(II)-based chemical usage, with a preliminary estimate of the global emissions from that process of 4.1 ± 1.9 Gg yr^{-1}.

After accounting for the decline due to anthropogenic emissions, changes in the interannual variability of the global mean atmospheric CH_3Br have been found to be largely driven by El Niño-Southern Oscillation (ENSO)-related changes in fire emissions, suggesting that climate variability may affect the future CH_3Br budget (Nicewonger et al., 2022). The imbalance between CH_3Br sources and sink terms of more than 30 Gg yr^{-1} reported for the late 1990s (e.g., Yvon-Lewis and Butler, 2002; Yvon-Lewis et al., 2009) has declined to 20 Gg yr^{-1} from unknown sources, based on NOAA observations and a 6-box ocean-atmosphere model (Saltzman et al., 2022). Time dependence and latitudinal distribution of the budget gap based on the model inversion suggests that it can be partitioned into a time-invariant natural source and a smaller time-varying component that scales with anthropogenic emissions during phaseout. Similar to CH_3Cl, CH_3Br emissions also have a very low direct radiative impact (GWP-100 of 2.43; Smith et al., 2021).

1.3 HALOGENATED VERY SHORT-LIVED SUBSTANCES (VSLSs)

VSLSs are defined as trace gases whose local lifetimes are shorter than 0.5 years and consist of organic and inorganic halogenated source gases (SGs) and product gases (PGs). The SGs include all VSLSs present in the atmosphere in the form they were emitted. Brominated and iodinated SGs are predominantly of natural oceanic origin, whereas chlorinated species have mostly anthropogenic sources. The halogenated PGs can arise from SG degradation and other sources of tropospheric halogens.

In contrast to longer-lived ODSs, which account for most of the present-day stratospheric halogen loading, VSLSs are not controlled by the Montreal Protocol (see **Box 1-3** for commonalities and differences between VSLSs and ODSs). There is convincing evidence that VSLSs now contribute about 25% to stratospheric bromine and 3–4% to stratospheric chlorine (Carpenter, Reimann et al., 2014; Engel, Rigby et al., 2018). Even though the VSLS contribution to total stratospheric chlorine is relatively small, it has shown a strong positive trend over the last decades (Hossaini et al., 2019). Recent studies have suggested that tropospheric iodine can also reach the stratosphere (Koenig et al., 2020) and contribute to halogen-driven ozone loss (Cuevas et al., 2022).

The overall contribution of VSLSs to stratospheric halogen loading and ozone destruction depends strongly on the spatial and temporal variability of their sources, transport pathways, and chemical transformation. In this section, we apply data from global networks to assess the mean surface mixing ratios and emissions, whereas observations close to the tropopause are used to infer the input of VSLSs to the stratosphere.

1.3.1 Tropospheric Abundance, Trends, and Emissions of Very Short-Lived Source Gases (VSL SGs)

Halogenated VSLSs are partially broken down during their transport to the stratosphere and show large spatial variability due to their nonuniform emission distributions and relatively short atmospheric lifetimes. A detailed compilation of chlorinated, brominated, and iodinated SG seasonal lifetimes was given in Table 1-5 of Carpenter, Reimann et al. (2014) and is updated in the *Annex* of this Assessment. Any interpretation of measurements from regional campaigns and global networks needs to take into account potential issues arising from the scarce spatial coverage and representativeness of the data.

Since the last Assessment, updated global network observations of chlorinated VSLSs have led to new emission estimates. Long-term changes of these emissions can show pronounced regional differences. For brominated VSLSs, emission estimates have remained largely unchanged, with some reduction of the upper and lower limits. Emissions of iodinated VSLSs are now considered to include inorganic iodine sources, which dominate the tropospheric iodine budget.

1.3.1.1 Chlorine-Containing VSL SGs

This section focuses on the chlorinated VSLSs most widely reported in the background atmosphere: dichloromethane (CH_2Cl_2), chloroform (trichloromethane, $CHCl_3$), tetrachloroethene (perchloroethylene, CCl_2CCl_2, shortened to C_2Cl_4), and 1,2-dichloroethane (CH_2ClCH_2Cl). In particular, CH_2Cl_2 and $CHCl_3$ have received much attention in the scientific literature in recent years due to increasing emission estimates. Long-term measurements of CH_2Cl_2 and C_2Cl_4 are available from both the NOAA and AGAGE surface networks, while measurements of $CHCl_3$ are available only from AGAGE. Hemispheric mean mole fractions from these globally distributed measurements and emissions derived with a 12-box model are given in **Table 1-4** and shown in **Figure 1-7**, together with regional emissions based on inverse modeling approaches (Claxton et al., 2020; An et al., 2021).

Dichloromethane (CH_2Cl_2) has shown steadily increasing mole fractions since the beginning of this century. Global mean mole fractions in 2020 amount to 38.3 and 45.5 ppt based on AGAGE and NOAA networks, respectively (**Table 1-4**). Differences between the global means of the two CH_2Cl_2 datasets of about 7 ppt in 2020 cannot be fully explained by the known calibration difference of ~10% (Carpenter, Reimann et al., 2014) and likely arise from differences in sampling locations between the networks. Large industrial sources lead to pronounced spatial variability (e.g., Claxton et al., 2020), which is also apparent in the strong IHDs with NH CH_2Cl_2 mole fractions being up to a factor of 3.5 larger than those in the SH (**Figure 1-7**). Global mean mole fractions increased by 3.2% yr^{-1} and 3.0% yr^{-1} for 2019–2020 based on AGAGE and NOAA, respectively (**Table 1-4**). These increase rates are smaller than the four-year mean increase rates for 2016–2020 of 4.3% yr^{-1} (AGAGE) and 4.6% yr^{-1} (NOAA). They are also considerably smaller than the peak growth rates of 6.7% yr^{-1} (AGAGE) and 6.6% yr^{-1} (NOAA) found for 2012–2016, thus confirming a slow flattening of the strong positive trends that occurred after 2010.

Anthropogenic sources of CH_2Cl_2 have been estimated to account for roughly 90% of global emissions (Montzka, Reimann et al., 2010). Natural marine sources of CH_2Cl_2 might also play a role; however, oceanic emission estimates have large uncertainties due to the paucity of observational data (e.g., Claxton et al., 2020). Measurements from the AGAGE and NOAA networks

Table 1-4. Annual global mean mole fractions of chlorinated VSL SGs and estimated emissions (including 1-sigma uncertainties) from the global networks. Emissions based on AGAGE and NOAA surface data were calculated using a global 12-box model (Cunnold et al., 1983; Rigby et al., 2013), identical to the global emissions shown in **Figure 1-3** for longer-lived ODSs. The calculations assume parameterized global steady-state total lifetimes of 0.54, 0.52, and 0.40 years for CH_2Cl_2, $CHCl_3$, and C_2Cl_4, respectively.

Compound	Annual Mean Mole Fraction (ppt)			Growth (2019–2020)		Annual Global Emissions (Gg yr^{-1})			Network
	2016	2019	2020	ppt yr^{-1}	% yr^{-1}	2016	2019	2020	
CH_2Cl_2	32.7	37.1	38.3	1.2	3.2	943 (±179)	1061 (±203)	1130 (±211)	AGAGE
	38.4	44.2	45.5	1.3	3.0	1126 (±204)	1328 (±235)	1328 (±242)	NOAA
$CHCl_3$	9.0	8.7	8.7	0.0	0.0	345 (±70)	335 (±69)	339 (±70)	AGAGE
C_2Cl_4	1.07	1.05	1.01	–0.04	–3.8	83 (±42)	86 (±40)	80 (±39)	AGAGE
	1.21	1.19	1.12	–0.07	–5.9	102 (±50)	98 (±49)	91 (±47)	NOAA

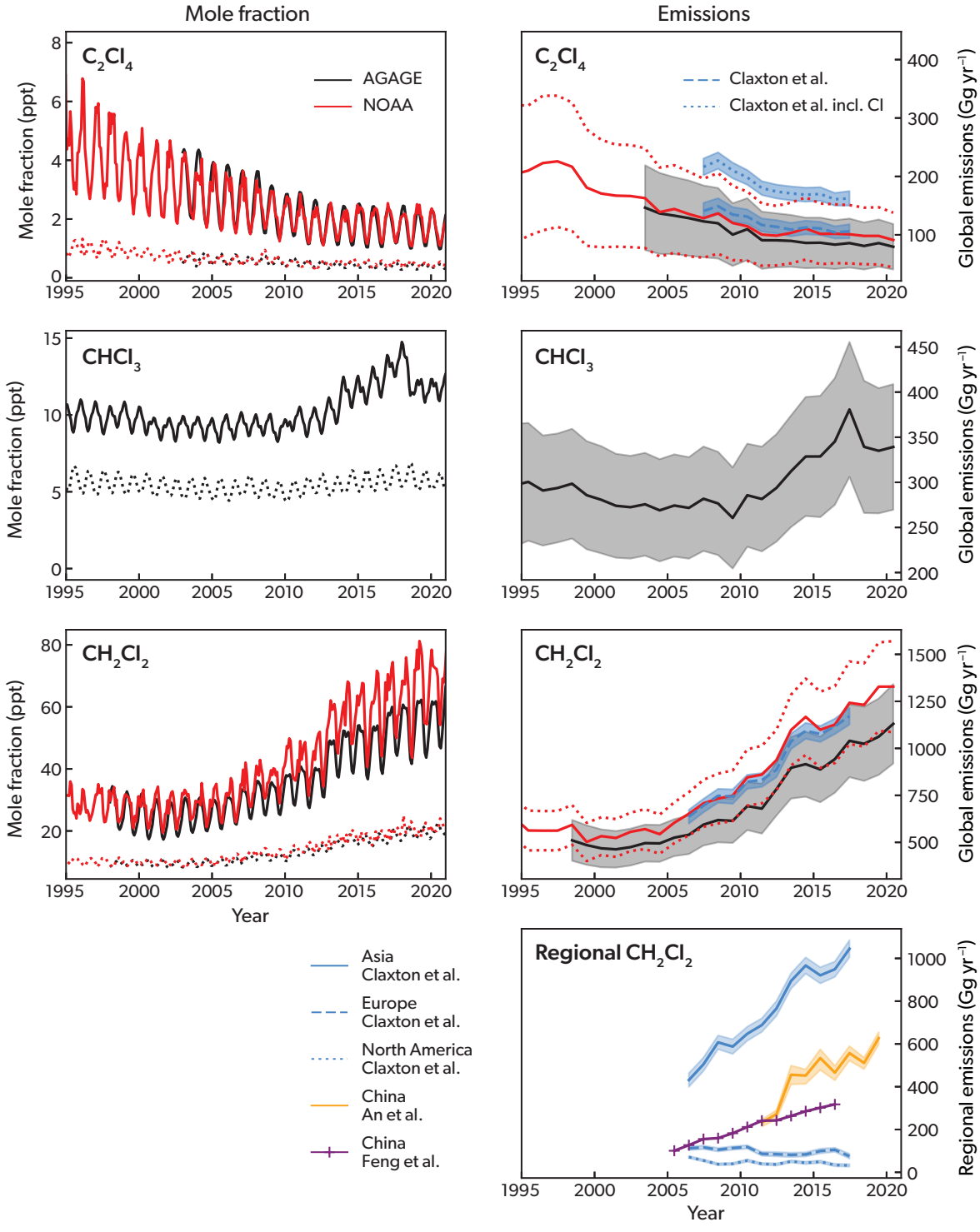

Figure 1-7. *(left three panels)* Monthly hemispheric mean mole fractions of C_2Cl_4, $CHCl_3$, and CH_2Cl_2 derived from AGAGE (black) and NOAA (red) observations in the Northern (solid lines) and Southern (dotted lines) Hemispheres. *(right three upper panels)* Global emissions estimates (Gg yr^{-1}) calculated using a global 12-box model (using methods described in **Figure 1-3**), with 1-sigma uncertainties indicated by shading (AGAGE) or dotted lines (NOAA). Global emissions for C_2Cl_4 from Claxton et al. (2020) are reported with loss due to only OH and photolysis and including an additional chlorine sink (incl. Cl). *(bottom right panel)* Regional estimates for Asia, Europe, and North America (Claxton et al., 2020, blue), as well as China (Feng et al., 2018, purple; An et al., 2021, yellow), are also shown together with 1-sigma uncertainties (shading). Estimates for China from Feng et al. (2018) use a bottom-up approach; all other regional estimates use a top-down methodology.

suggest global CH_2Cl_2 emissions for 2020 of 1130 (±211) Gg yr^{-1} and 1328 (±242) Gg yr^{-1} (**Table 1-4**), respectively, corresponding to a factor 2.5 increase compared to 2000.

Regional emission estimates have highlighted the influence of CH_2Cl_2 emissions from Asia, and in particular from China, on the global estimates and their long-term changes. Based on surface observations and chemistry-transport modeling, Asian emissions have been suggested to account for about 90% of global emissions in 2017 (Claxton et al., 2020). The global emission estimates from that study show a total increase between 2006 and 2017 of 534 Gg yr^{-1}, which is in very good agreement with other estimates of global long-term changes (**Figure 1-7**). Regional CH_2Cl_2 emissions from Asia account for an increase of 615 Gg yr^{-1}, more than offsetting the small decrease in European and North American emissions over the same time period (**Figure 1-7**). A substantial fraction of the Asian emission increase is driven by China, with a 217 Gg yr^{-1} increase estimated for 2005–2016 based on a bottom-up emission inventory (Feng et al., 2018). A combined top-down and bottom-up CH_2Cl_2 emission estimate suggests an even larger role for emissions from China, with an increase of 395 Gg yr^{-1} for 2011–2019 completely accounting for the global emission increase over the same time period (An et al., 2021). On a local scale, strongly enhanced mole fractions have been observed in China, potentially due to enhanced local emissions (Benish et al., 2021; Zeng et al., 2020). In addition, emissions from India appeared to have experienced a pronounced increase of 77 Gg yr^{-1} from 2008 to 2016 (Say et al., 2019).

Global chloroform ($CHCl_3$) mole fractions (**Table 1-4**) slightly decreased from 9.0 ppt in 2016 to 8.7 ppt in 2020 (AGAGE). Interestingly, NH surface concentrations increased quite rapidly between 2011 and 2017 (**Figure 1-7**), by 4.9% yr^{-1}; however, around 2018, concentrations dropped in a steplike manner back down to 2015 levels. A detailed analysis focusing on 2010–2015 revealed that the background $CHCl_3$ concentrations increased at nearly all stations, but the number of pollution events with highly elevated $CHCl_3$ only increased at stations in Asia, suggesting nearby sources (Fang et al., 2019a).

Atmospheric $CHCl_3$ stems from natural and anthropogenic emissions, with the contribution from each source term currently being debated and anthropogenic emission estimates ranging from 10% (McCulloch, 2003) to at least 50% (Worton et al., 2006) of the total emissions. In addition to the known natural sources (e.g., phytoplankton, peatlands, soils, and plants), $CHCl_3$ emissions from Antarctic tundra (Zhang et al., 2021), Dead Sea landscapes (Schechner et al., 2019), and coastal wetlands degraded by sea level rise (Jiao et al., 2018) were recently identified. Measurements from the AGAGE network suggest total global $CHCl_3$ emissions for 2020 of 339 (±70) Gg yr^{-1} (**Table 1-4**). Consistent with the global mole fractions, emissions increased until 2017 and dropped sharply afterwards back to 2015 values (**Figure 1-7**). Regional emission estimates for 2010–2015 suggest that the global emission increase of 44 Gg over this time period can be explained entirely by increasing emissions from eastern China (Fang et al., 2019a; 2019b).

Atmospheric C_2Cl_4 has continued to decrease over the past few decades (**Figure 1-7**). Global mean mole fractions in 2020 amount to 1.01 and 1.12 ppt based on the AGAGE and NOAA networks, respectively (**Table 1-4**). Decrease rates of 3.8% yr^{-1} (AGAGE) and 5.9% yr^{-1} (NOAA) for 2019–2020 are similar to values provided in the last Assessment for 2015–2016, suggesting that while the decreasing trend has slowed down when compared to the first decade of this century, it is still ongoing.

In consequence, global C_2Cl_4 emission estimates also show a slow decline, reaching values of 80 (±39) Gg yr^{-1} and 91 (±47) Gg yr^{-1} for AGAGE and NOAA, respectively (**Table 1-4**). The long-term decline of C_2Cl_4 emissions based on the 12-box model is in good agreement with estimates based on chemistry-transport modeling if the termolecular loss reaction of C_2Cl_4 with Cl atoms is not included (**Figure 1-7**). The latter approach suggests similar emissions from North America, Europe, and Asia, which together account for the total global emissions (Claxton et al., 2020). It also demonstrates the sensitivity of the emission estimates to the atmospheric C_2Cl_4 lifetime by showing that global emissions are ~1.5 times higher if an uncertain chlorine sink is included. Regional top-down emission estimates suggest modest contributions from India (2.9 ± 0.5 Gg yr^{-1}) and South Africa (0.8 ± 0.2 Gg yr^{-1}), accounting for 3.5% and 1% of the global emissions, respectively (Say et al., 2019; 2020).

No 1,2-dichloroethane (CH_2ClCH_2Cl) measurements have been published for either the AGAGE or the NOAA network; as a result, its budget and emissions are poorly constrained. Based on 2013/14 aircraft observations, boundary layer CH_2ClCH_2Cl mole fractions are of the order ~10–20 ppt in the NH (Engel, Rigby et al., 2018), with SH mole fractions a factor of ~6 lower (Hossaini et al., 2016), indicative of dominant anthropogenic sources.

For other minor chlorinated VSLS compounds such as chloroethane (C_2H_5Cl) and 1,2-dichloropropane ($C_3H_6Cl_2$), noteworthy mole fractions have been observed in and above the planetary boundary over a highly industrialized region in China during spring 2016 (Benish et al., 2021). No global background values are available for either of the two gases. While C_2H_5Cl and $C_3H_6Cl_2$ abundances were significantly lower than that of CH_2Cl_2, they were of the same magnitude as $CHCl_3$ and CH_2ClCH_2Cl, with all chlorinated VSL SGs being enhanced in this region compared to their global tropospheric background levels.

Short-lived halogenated unsaturated hydrocarbons (halogenated olefins), including the hydrofluoroolefins (HFOs) and the hydrochlorofluoroolefins (HCFOs), have been introduced as alternatives to HCFCs and HFCs due to their low GWP. While the HFOs are included in *Chapter 2*, the HCFOs are discussed as part of the VSLSs in this section. The only atmospheric record of HCFOs currently available is that for HCFO-1233zd(E) (E-CF_3CH=CHCl) from central Europe, where it has been detectable in all samples since 2016. A mean mole fraction of 0.03 ppt observed at the Jungfraujoch station in 2016 has increased to 0.19 ppt in 2020 (update from Vollmer et al., 2015a), which under the assumption of linear growth corresponds to an increase of 36% yr^{-1}. Based on these observations, HCFO-1233zd(E) emission estimates from Switzerland of 6 Mg yr^{-1} were derived for 2019/20 (Rust et al., 2022).

1.3.1.2 Bromine-Containing VSL SGs

The most abundant brominated VSLSs, bromoform ($CHBr_3$) and dibromomethane (CH_2Br_2), are largely produced by marine organisms such as macroalgae and phytoplankton (e.g., Carpenter and Liss, 2000; Leedham et al., 2013; Keng et al., 2021). $CHBr_3$ also has some anthropogenic sources resulting from the chemical treatment of sea water used in cooling units, industry, and desalination plants, as well as for ship ballast water

Box 1-3. Metrics for ODSs and VSLSs

Halogenated long-lived ozone-depleting substances (ODSs; lifetimes >0.5 yr) and very short-lived substances (VSLSs; lifetimes <0.5 yr) both contribute to stratospheric ozone depletion. However, the two groups of gases differ substantially in terms of their sources, emissions, and tropospheric processing. Some of the existing metrics traditionally used to evaluate long-lived ODSs cannot be directly applied to VSLSs without considering additional adjustments.

Commonalities and differences

Long-lived ODSs have largely anthropogenic sources, resulting from their past use and from current inadvertent by-product formation. Some gases have accumulated substantial banks over the past decades, which can delay emission reductions. Only a small fraction of ODSs stem from natural sources such as oceanic and terrestrial ecosystems. VSLSs have both natural and anthropogenic sources, with brominated and iodinated VSLSs being mostly produced naturally in the ocean and some smaller anthropogenic contributions from coastal power plants and ships (Maas et al., 2021). In contrast, chlorinated VSLSs originate largely from industrial processes, and their atmospheric abundances have increased strongly over the last two decades due to growing industrial emissions (Claxton et al., 2020). Noteworthy natural VSLS emissions can be impacted by anthropogenically driven oceanographic, meteorological, and air quality changes (*Chapter 7*). In consequence, there could be future changes in VSLS emissions resulting from direct anthropogenic emissions or anthropogenically altered natural emissions. Distinguishing between these two source terms will be a challenge, due to the existing large uncertainties in emission estimates and the paucity of observational data (see **Box 1-2**).

Most long-lived ODSs persist in the atmosphere for decades to centuries and are therefore well mixed throughout the troposphere. Irrespective of the geographic location of their emissions, nearly all long-lived ODSs are eventually injected into the stratosphere, where they release their ozone-depleting chlorine and bromine. In consequence, their impact on stratospheric ozone is largely independent of changes in emission location and troposphere-stratosphere transport patterns. In contrast, VSLSs can undergo rapid chemical degradation with pronounced lifetime variations depending on the distribution of tropospheric oxidants (e.g., Rex et al., 2014) and background conditions such as temperature and solar flux (e.g., Hossaini et al., 2010). In consequence, the impact of VSLSs on stratospheric ozone depends on a complex interplay between emission location, transport patterns, efficiency of deposition processes, and chemical processing, with enhanced transport in the tropics being of particular importance. In addition, VSLSs in inorganic form can impact tropospheric chemistry, thus contributing to tropospheric and stratospheric ozone depletion.

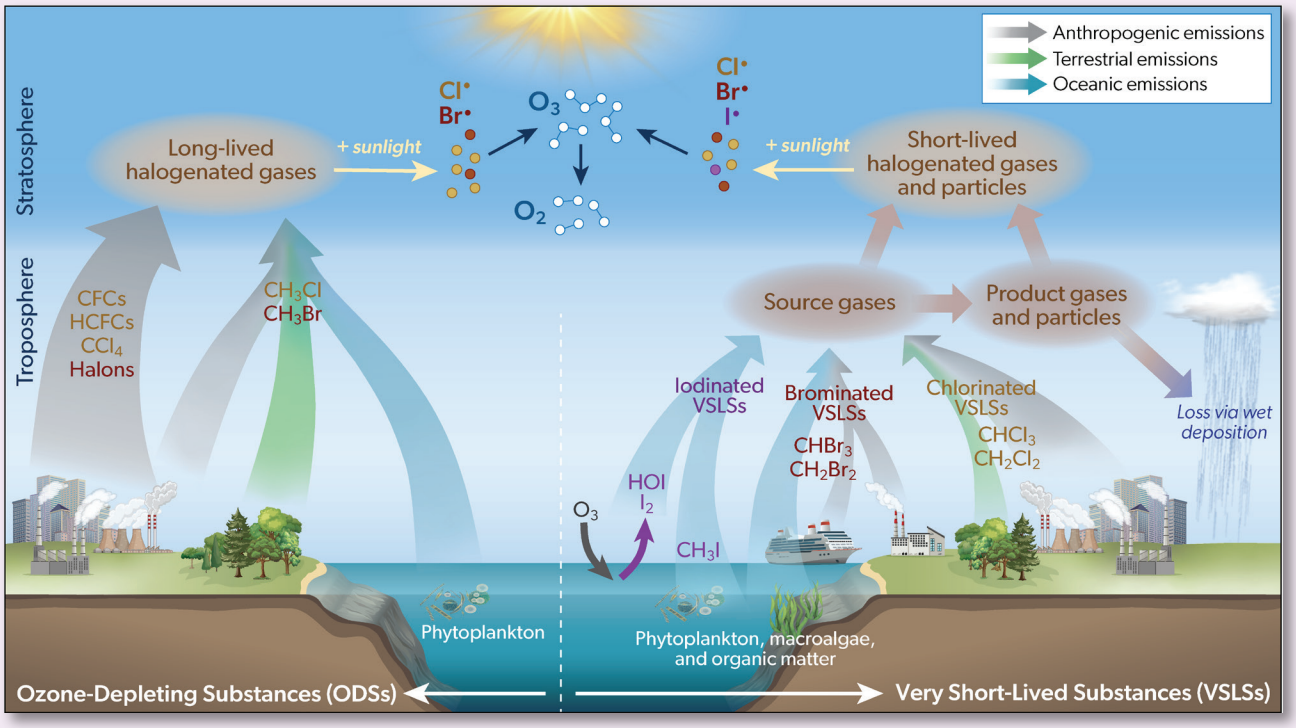

Box 1-3 Figure 1. Schematic of long-lived ozone-depleting substances (ODSs) and halogenated very short-lived substances (VSLSs).

Conventional metrics and their adjustments

Ozone depletion potential (ODP) was introduced as a metric for assessing a compound's ability to destroy stratospheric ozone (Wuebbles, 2015) and has been used extensively in policy frameworks, including the Montreal Protocol. The original concept was developed for long-lived ODSs and, given their uniform distribution and negligible chemical loss in the troposphere, is based on a single-value index independent of emission location and season. Moreover, the original ODP concept, having been developed for long-lived gases that do not impact tropospheric ozone, is based on the total column ozone change.

The more recent application of the ODP concept to VSLSs has led to some modifications of the original definition. As the ODP of a VSLS can change by a factor of up to 30 depending on where the emissions occur, ODP estimates for VSLSs must be reported as a function of season and location of emissions (e.g., Ko, Poulet et al., 2003; Brioude et al., 2010). Furthermore, the contribution of VSLSs to tropospheric ozone destruction needs to be excluded when calculating their ODP (Pisso et al., 2010; Claxton et al., 2019), prompting the introduction of the term stratospheric ODP (SODP, Zhang et al., 2020). Maps of SODP-weighted emissions and their global averages allow for the direct comparisons of the impact of short- and long-lived halogens on stratospheric ozone (Tegtmeier et al., 2015). For long-lived gases, ODP and SODP have nearly the same values, whereas for VSLSs, the difference between these two metrics provides a measure of their influence on tropospheric ozone (Zhang et al., 2020).

Quantitative intercomparisons of the total chlorine and bromine contributions to the stratospheric halogen loading also suffer from inconsistencies. For example, chlorinated VSLSs are taken into account when estimating the total tropospheric organic chlorine (*Section 1.4.1.1*), whereas brominated VSLSs are not included in the calculation of the total tropospheric organic bromine (*Section 1.4.2.1*). While this approach does not alter existing tropospheric halogen trends, brominated VSLSs may be of growing interest for trend estimates in coming years, given their highly uncertain future changes (*Chapter 7*).

A metric of the total amount of halogen-driven stratospheric ozone depletion is the equivalent effective stratospheric chlorine (EESC; *Section 1.4.4*). Current formulations of EESC (Engel et al., 2018) do not include the impact of VSLSs on stratospheric ozone and thus do not reflect their changing emissions over time. Given the highly variable tropospheric lifetimes of VSLSs, quantifying their contribution to EESC requires a seasonally resolved stratospheric injection function taking into account their tropical tropopause abundance, instead of the global annual surface mean values usually considered for ODSs.

Overall, large improvements in the understanding of VSLS emissions and tropospheric processing have been made over the recent decades. This has led to adjustments of some of the existing metrics, providing a basic framework for consistent intercomparison of VSLS and ODS impacts on stratospheric ozone. Other metrics continue to include only ODSs and might change in the future once detailed VSLS distribution estimates are available.

(Boudjellaba et al., 2016; Maas et al., 2019; 2021; Quivet et al., 2022). Their marine boundary layer mole fractions amount to 1.2 ppt ($CHBr_3$) and 0.9 ppt (CH_2Br_2) on average (**Table 1-5**), with a pronounced spatial variability.

Air-sea fluxes of brominated VSLSs show large spatiotemporal variations driven by changes in primary marine productivity, biogeochemical cycling, anthropogenic sources, sea surface temperature, and meteorology. Ship-based and land-based observations suggest high fluxes in coastal and upwelling regions with steep gradients toward the open ocean (e.g., Ziska et al., 2013). Given this large variability and the lack of adequate seasonal and spatial coverage of observational data, brominated VSLS emission inventories are not well constrained, with bottom-up estimates being a factor of two lower than top-down estimates. For $CHBr_3$, the range of global emission estimates of 120–820 Gg Br yr^{-1} given in the last Assessment (Engel, Rigby et al., 2018) has been changed to 150–820 Gg Br yr^{-1}, reflecting an update of the Ziska et al. (2013) emission climatology (Fiehn et al., 2018). The updated inventory shows enhanced $CHBr_3$ emissions in the tropical Indian Ocean and subtropical northern Atlantic, with emissions in the west Indian Ocean being almost twice as large as previous estimates. A new $CHBr_3$ emission inventory from a data-oriented machine-learning algorithm suggests an oceanic source of 385 Gg Br yr^{-1}, falling in the middle of the range of existing estimates (Wang et al., 2019). The study derived very high regional $CHBr_3$ emissions for the Bay of Bengal and South China Sea; the authors pointed out that these might be overestimated due to the lack of data in these regions and therefore require further confirmation.

Anthropogenic sources of $CHBr_3$ from the chlorination of coastal power plant cooling water in East and Southeast Asia have been estimated to amount to 25–75 Gg Br yr^{-1} (Maas et al., 2021). As such industrial sources are not included in any of the existing bottom-up emission inventories, they could explain some of the discrepancies between different approaches. For CH_2Br_2, the range from the last Assessment (57–280 Gg Br yr^{-1}) has been reduced to 54–100 Gg Br yr^{-1} when taking the new machine-learning algorithm estimates into account. This is consistent with a model sensitivity study showing more realistic CH_2Br_2 abundances in the lower-stratosphere NH high latitudes if the lower emission scenarios (i.e., Liang et al., 2010; Ordóñez et al., 2012) are used (Keber et al., 2020). Potential future changes of brominated VSLS emissions are discussed in *Chapter 7*.

1.3.1.3 Iodine-Containing VSL SGs

Iodinated VSLSs include the group of organic SGs, which stem from biotic (e.g., phytoplankton and cyanobacteria) and abiotic (e.g., photochemical breakdown of dissolved organic matter) oceanic sources. For the first time, this section also discusses inorganic iodine emissions, as new studies suggest that both organic and inorganic sources can contribute iodine to the stratosphere. Consequently, and differing from other VSLS

and ODS sources, iodine SGs include both organic (i.e., carbon-bonded) and inorganic (i.e., HOI, I_2), gas-phase emissions from the surface. However, since inorganic iodine plays an active role in tropospheric chemistry (i.e., recycling back and forth among reactive and reservoir species), the inorganic iodine SGs are expected to be completely recycled to inorganic PGs before they reach the upper troposphere (*Section 1.3.2.3*).

Methyl iodide (CH_3I) is the main organic iodine-containing source gas, with a mean mole fraction of 0.8 ppt in the marine atmospheric boundary layer (**Table 1-5**). Air-sea fluxes of CH_3I from coastal and open-ocean environments have been estimated to cause an input of 157–550 Gg I yr^{-1} to the atmosphere (Butler et al., 2007; Ziska et al., 2013), which is unchanged compared to the last two Assessments. CH_3I has been proposed as a replacement of CH_3Br as it is very effective in controlling a wide variety of soil pests and weeds (Waggoner et al., 2000). However, environmental and health concerns have limited its use as fumigant, and no current emission estimates from such sources exist. Other iodinated VSLSs, such as CH_2I_2, CH_2IBr, and, CH_2ICl account for an additional 340 Gg I yr^{-1}. Iodotrifluoromethane (CF_3I), currently under consideration as a replacement for halon in fire suppression

Table 1-5. Summary of observed mole fractions (in ppt) of VSL SGs from the marine atmospheric boundary layer (MBL) to the tropical tropopause layer (TTL) and above. Note that many of the upper-tropospheric measurements were made at least one decade ago in the case of brominated and iodinated SGs. As chlorinated SGs have significant anthropogenic sources and some show trends, data are based only on measurements from 2015 onwards.

	Marine Boundary Layer		Lower TTL		LZRH(z_0)[1]		Upper TTL		Tropical Tropopause	
Height Range			12 – 14 km		14.5 – 15.5 km		15.5 – 16.5 km		16.5 – 17.5 km	
Potential Temperature Range			340 – 355 K		355 – 365 K		365 – 375 K		375 – 385 K	
	Median[2]	Range[4]	Mean[3]	Range[4]	Mean[3]	Range[4]	Mean[3]	Range[4]	Mean[3]	Range[4]
Chlorinated VSLSs Based on Measurements from 2015 Onwards										
CH_2Cl_2			36.9	30.4–59.3	37.1	29.2–55.7	41.6	30.8–68.4	41.3	33.4–56.9
$CHCl_3$			7.7	5.8–8.4	7.7	6.0–8.6	7.8	5.7–8.5	6.7	5.4–7.8
C_2Cl_4			0.77	0.42–1.02	0.66	0.32–0.95	0.55	0.15–0.90	0.31	0.07–0.71
CH_2ClCH_2Cl			8.3	3.3–11.4	8.7	3.3–13.6	7.2	1.9–12.1	4.0	1.0–8.4
Brominated and Iodinated VSLSs Based on Measurements from 2004 Onwards										
$CHBr_3$	1.2	0.4–4.0	0.61	0.22–1.51	0.45	0.05–1.60	0.35	0.02–1.20	0.18	0.01–0.54
CH_2Br_2	0.9	0.6–1.7	0.93	0.61–1.15	0.81	0.49–1.08	0.72	0.30–1.11	0.59	0.17–0.89
CH_2BrCl	0.10	0.07–0.12	0.22	0.07–0.45	0.19	0.08–0.45	0.22	0.10–0.42	0.18	0.07–0.40
$CHBr_2Cl$	0.3	0.1–0.8	0.13	0.06–0.23	0.10	0.04–0.19	0.09	0.02–0.16	0.06	0.00–0.14
$CHBrCl_2$	0.3	0.1–0.9	0.23	0.14–0.55	0.17	0.08–0.40	0.15	0.07–0.31	0.11	0.05–0.32
CH_3I	0.8	0.3–2.1	0.16	0.00–0.49	0.10	0.00–0.32	0.05	0.00–0.32	0.03	0.00–0.14
Total VSLS Halogen Budgets Based on Estimates Above										
Total Cl			118	87–173	118	85–170	124	84–191	113 (105)[5]	86–158 (85–125)[5]
Anthrop. Cl[6]			98	72–147	99	70–144	104	69–164	94	71–134
Total Br	6.5	2.8–18.0	4.4	2.2–8.3	3.5	1.3–8.3	3.0	0.9–6.9	2.1	0.5–4.4
Total I	0.8	0.3–2.1	0.16	0.00–0.49	0.10	0.00–0.32	0.05	0.00–0.32	0.03	0.00–0.14

Notes:
[1] LZRH (z_0) corresponds to the level of zero clear-sky radiative heating (see **Box 1-3** of Carpenter, Reimann et al., 2014). As in the previous Assessment, this level is at about 15 km or 360 K, where there is a transition from clear-sky radiative cooling to clear-sky radiative heating.
[2] In the MBL, abundances are median values. For tropical MBL CH_2Cl_2, $CHCl_3$, CH_2ClCH_2Cl, and C_2Cl_4, no updates exist to the data from the CAST and CONTRAST missions presented in the last Assessment. MBL $CHBr_3$, CH_2Br_2, and CH_3I data are based on tropical data from the HalOcAt campaign (Ziska et al., 2013). MBL CH_2BrCl, $CHBr_2Cl$, and $CHBrCl_2$ data are from the previous Assessment (Carpenter, Reimann et al., 2014).
[3] In the TTL, abundances are mean values. For brominated VSLSs and CH_3I, data have been compiled from observations obtained during the Pre-AVE, CR-AVE, TC4, HIPPO, SHIVA, CONTRAST, and ATTREX aircraft campaigns (Navarro et al., 2015; Pan et al., 2017; Sala et al., 2014; Wofsy et al., 2011) and from balloon observations (Brinckmann et al., 2012). ATTREX values used here differ from those used in Wales et al. (2018), as they have been filtered by altitude instead of applying any tracer-tracer correlation. For chlorinated VSLSs, data are from the VIRGAS (2015) and POSIDON (2016) missions in 2015/16 only. (See below for definitions of field mission acronyms.) Note that calibration scales for VSLSs may differ among different research groups (e.g., Hall et al., 2014; Jones et al., 2011). Intercalibration of standards during CAST, CONTRAST, and ATTREX revealed generally good agreement between VSLS measurements performed by different instruments (relative standard deviation of <10%), although losses in aircraft sampling lines can add a major source of uncertainty (Andrews et al., 2016).
[4] In the MBL, the stated observed range is 10th to 90th percentile. In the TTL, the stated observed range represents the smallest mean minus 1 standard deviation and the largest mean plus 1 standard deviation.
[5] Values for 2019 are based on updated model simulations first described in Hossaini et al. (2019), which is used to derive total stratospheric VSL source gas injection for chlorine, as explained in *Section 1.3.2.1*. Model values are used in order to reduce variability from individual campaigns in assessing total Cl input to the stratosphere.
[6] The anthropogenic fraction of VSLS (Anthrop. Cl) is approximate and has been calculated from the sum of 90% of CH_2Cl_2, 50% of $CHCl_3$, and 100% of other compounds. Anthropogenic $CHCl_3$ source contributions are highly uncertain and have been chosen here as the upper range estimate of 50%.

Pre-AVE = Pre-Aura Validation Experiment (2004); CR-AVE = Costa Rica-Aura Validation Experiment (2006); TC4 = Tropical Composition, Cloud, and Climate Coupling missions (2007); HIPPO = HIAPER (High-Performance Instrumented Airborne Platform for Environmental Research) Pole-to-Pole Observations (2009–2011); SHIVA = Stratospheric Ozone: Halogen Impacts in a Varying Atmosphere (2011); ATTREX = Airborne Tropical TRopopause EXperiment (2011, 2013, and 2014); CAST = Coordinated Airborne Studies in the Tropics (2014); CONTRAST = Convective Transport of Active Species in the Tropics (2014); VIRGAS = Volcano-plume Investigation Readiness and Gas-phase and Aerosol Sulfur (2015); POSIDON = Pacific Oxidants, Sulfur, Ice, Dehydration, and cONvection (2016).

systems, has been estimated to have very little impact on stratospheric ozone due to its short lifetime (Zhang et al., 2020).

Inorganic iodine emissions occur in the form of hypoiodous acid (HOI) and molecular iodine (I_2) fluxes when ocean surface iodide (I^-) dissolved in the seawater reacts with deposited gas-phase ozone (Carpenter et al., 2013). Emission estimates of inorganic iodine depend strongly on surface I^- concentrations, which can vary by more than two orders of magnitude and are difficult to parameterize in regions that lack observational data (e.g., Wadley et al., 2020). A high-resolution dataset of sea-surface I^- estimates based on a machine learning algorithm suggests highest I^- concentrations in the tropics (Sherwen et al., 2019; Carpenter et al., 2021). Another uncertainty arises from the effect of the sea surface microlayer on I_2 solubility and emissions, which is currently not fully understood (Tinel et al., 2020). Global estimates of oceanic inorganic iodine emissions stem from modeling studies and range between 1.9 Tg I yr^{-1} (Prados-Roman et al., 2015) and 2.1 Tg I yr^{-1} (Sherwen et al., 2016). In consequence, inorganic iodine sources dominate the tropospheric iodine budget (Prados-Roman et al., 2015) and can account for a large fraction of tropospheric iodine oxide (IO) levels in the tropical Atlantic (Read et al., 2008; Lawler et al., 2014) and eastern Pacific (MacDonald et al., 2014), although they fail to adequately explain IO measurements in the Indian and Southern Oceans (Inamdar et al., 2020). Potential future changes of iodinated VSLS emissions are discussed in *Chapter 7*.

1.3.2 Input of VSLS Halogen to the Stratosphere

During transport from their surface sources to the stratosphere, halogenated SGs can undergo chemical degradation mainly through reaction with OH or photolysis. The originating halogenated PGs can experience dry and wet scavenging during transit to the stratosphere. We differentiate between stratospheric halogen input in the form of the emitted source gases (source gas injection [SGI]) and in the form of product gases (product gas injection [PGI]). While PGI has been traditionally based on gas-phase inorganic halogens, it can now also include

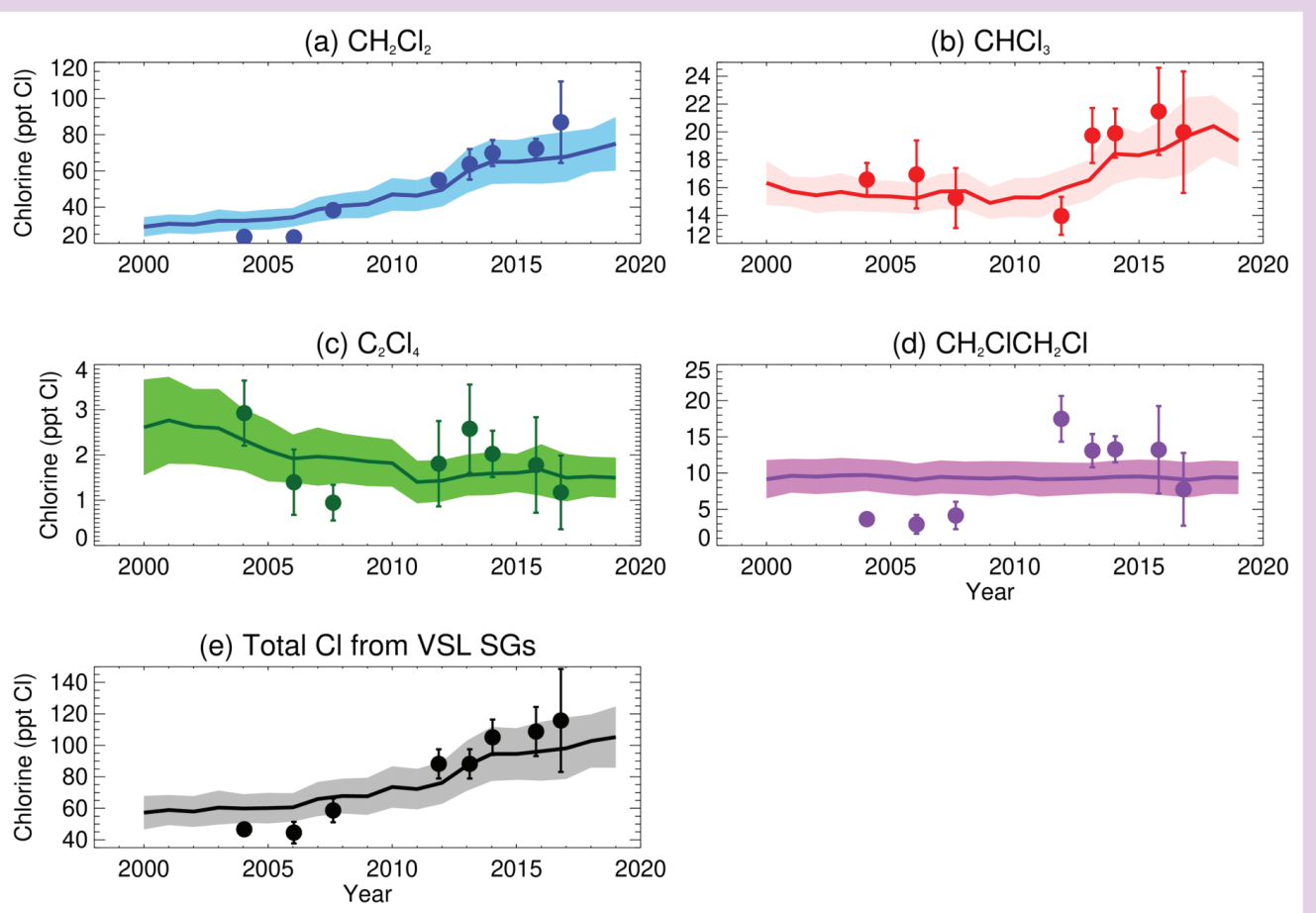

Figure 1-8. Stratospheric chlorine source gas injection (ppt Cl) from (a) CH_2Cl_2, (b) $CHCl_3$, (c) C_2Cl_4, (d) CH_2ClCH_2Cl, and (e) total. Model results (solid lines) with the ±1-sigma uncertainty (shading) are tropical mean (20°N–20°S) values derived from simulations with the offline 3-D chemistry-transport model TOMCAT/SLIMCAT constrained by observed surface abundances of these source gases. Observed tropopause quantities (filled circles) are averages (vertical bars denote ±1-sigma) for available aircraft data between 16.5 and 17.5 km in the tropics from Pre-AVE in 2004; CR-AVE in 2006; TC4 in 2007; ATTREX in 2011, 2013, and 2014; VIRGAS in 2015; and POSIDON in 2016 (campaign acronyms are provided in **Table 1-5**). [Updated from Hossaini et al., 2019.]

carbon-bonded compounds (e.g., phosgene) and particulate iodine (iodine taken up in particles). The relative contributions of SGI and PGI are different for each compound and depend on source distributions, tropospheric loss rates, timescales of troposphere-to-stratosphere transport, heterogeneous recycling processes, and removal by precipitation or sedimentation.

SGI is estimated from the global average halogen SG mixing ratios transported into the stratosphere and has been quantified from measurements around the tropical tropopause (~17 km), complemented by model simulations. PGI is estimated as the global average inorganic halogen mixing ratio injected into the stratosphere and has been derived mostly from global, Lagrangian, and box-modeling studies oriented to reproduce aircraft and balloon observations close to the tropopause.

1.3.2.1 Input of VSLS Chlorine to the Stratosphere

The input of VSLS chlorine to the stratosphere amounts to a total of 130 ± 30 ppt Cl in 2020. The underlying SGI and PGI contributions are estimated based on model data constrained by surface observations as well as aircraft and satellite observations, as explained below.

Observation-based chlorine SGI from VSLSs was estimated as 113 (86–158) ppt Cl based on measurements from the two tropical campaigns VIRGAS (2015) and POSIDON (2016; Table 1-5). CH_2Cl_2, $CHCl_3$, and CH_2ClCH_2Cl account for ~73%, ~18%, and ~7% of this total, respectively; the remaining ~1% stems from C_2Cl_4. Total chlorine SGI has increased by 13 ppt Cl (12%) compared to observational estimates given in the last Assessment and based on 2013/14 aircraft missions, with most of this difference (10 ppt Cl) driven by anthropogenic VSLS changes. It is noteworthy that the campaign-derived estimates might not reflect tropical average SGI trends, given the significant spatiotemporal variability in VSLS transport and lifetimes. For instance, aircraft measurements in the Asian summer monsoon anticyclone region during the StratoClim campaign (2015/16) showed significantly enhanced levels of CH_2Cl_2, CH_2ClCH_2Cl, and $CHCl_3$ (Adcock et al., 2021). In total, the three gases add up to 169–393 ppt Cl, which is more than two times the abundances observed over the West Pacific and Gulf of Mexico region, highlighting that the anticyclone acts as a rapid transport mechanism of nearby surface emissions into the stratosphere. Observations above Europe and the Atlantic during the WISE aircraft campaign (2017) detected up to a 150% (100%) enhancement in CH_2Cl_2 ($CHCl_3$) in air masses that entered the extratropical UTLS via the Asian summer monsoon anticyclone (Lauther et al., 2022). On a global scale, the enhanced entrainment has been estimated to contribute between 0.3 and 34.9 ppt to total equivalent chlorine in the NH lower stratosphere (Adcock et al., 2021; Ploeger et al., 2017).

Model-based chlorine SGI from VSLSs in 2019 is 105 (85–125) ppt (**Table 1-5**), showing good agreement with the observational data (**Figure 1-8**; update of Hossaini et al., 2019), with differences largely explained by limited sampling during individual campaigns. The chemistry-transport model simulations based on the latest and most up-to-date model version give an updated value of 96 (77–115) ppt for chlorine SGI in 2016. Consistent with the observed surface mole fractions, which are used to drive the simulations, the SGI model estimates show a continuous positive trend due to growing CH_2Cl_2, with slower growth after 2014 compared to earlier years.

Chlorinated PGI have been estimated based on TTL observations of phosgene ($COCl_2$) and hydrogen chloride (HCl), which can arise from chlorinated VSLS PGI or from recirculation of stratospheric air. Based on observations of $COCl_2$ (up to 32 ppt Cl) and HCl (up to 20 ppt Cl), chlorinated VSLS PGI was estimated as 25 ppt in the last Assessment (Engel, Rigby et al., 2018). The contribution of VSLSs to satellite measurements of $COCl_2$ between 2004 and 2016 changed from 20% to 27% (Harrison et al., 2019), consistent with model-derived long-term trends of chlorine PGI over the same time period (Hossaini et al., 2015). This trend is suspected to be driven by the growth of the CH_2Cl_2 degradation products, which are the largest contributors to the overall PGI (Hossaini et al., 2019).

Chlorinated VSLS PGI estimates are also available from model simulations, with the complexity of the involved chemical processes being one of the major challenges. Hossaini et al. (2019) determined a non-zero chlorine PGI from VSLSs of ~18 (±5) ppt Cl, which increases to ~34 (±7) ppt Cl if no tropospheric wet removal of chlorinated PGs is assumed. Following the methodology of the last Assessment, we derive a best estimate of 25 (13–50) ppt Cl PGI from VSLSs (**Table 1-6**), with the lower limit reflecting the lower limit from modeling work (Hossaini et al., 2019) and the mean value and upper limit reflecting the observational estimates.

In summary, a total of 130 (100–160) ppt Cl is injected into the stratosphere, according to our best estimates (**Table 1-6**). The contribution from SGI accounts for 105 (85–125) ppt Cl and is based on model data constrained by surface observations

Table 1-6. Summary of estimated VSL source gas injection (SGI) and product gas injection (PGI) contributions to stratospheric halogens (based on observations and model results).

VSLS Best Estimate (ppt)	SGI[1]	PGI[2]	Total (SGI + PGI)[3]
Chlorine	105 (85–125)	25 (13–50)	130 (100–160)
Bromine	2.1 (0.5–4.4)	2.8 (1.8–4.2)	5 (3–7)
Iodine	0–0.1	0.3–0.8	0.3–0.9

Notes:
[1] The SGI estimate for chlorinated SGs, which show increasing trends, is representative of the year 2019 based on model data (see **Table 1-5**). SGI for bromine and iodine represent the global mean from 2004 onwards, as there are no reports of long-term trends.
[2] PGI for chlorine has been estimated from observations based on HCl and $COCl_2$ and modeling studies and is representative of the year 2020. PGI for bromine has been estimated by box- and global-modeling studies based on BrO measurements from 2004 onwards.
[3] The SGI and PGI lower/upper limits are not strictly additive, because whenever SGI increases (e.g., due to rapid lifting), the correspondent PGI arising from SG photodecomposition decreases (and vice versa).

(update of Hossaini et al., 2019) in order to avoid the seasonal and regional variability of individual campaign-based estimates. The contribution from PGI accounts for 25 (13–50) ppt Cl. Compared to 2016 estimates based on the same methodology, chlorine VSLS injection to the stratosphere has increased by 10 ppt. While this increase is not significant, given the large uncertainties of the total VSLS injection, it is consistent with increasing abundances of tropospheric CH_2Cl_2. Model-derived long-term trends suggest that the relative contribution of VSLSs to total stratospheric chlorine increased from ~2% in 2000 to ~3.4% in 2017, reflecting VSLS growth and decreases in long-lived halocarbons (Hossaini et al., 2019).

1.3.2.2 Input of VSLS Bromine to the Stratosphere

Since the previous Assessment, the two tropical campaigns VIRGAS (2015) and POSIDON (2016) have confirmed existing estimates of stratospheric injections of bromine VSL SGs, which range from 0.5 to 4.4 ppt (**Table 1-5**). Most of the stratospheric injection of $CHBr_3$ was modeled to occur over the southern tip of India during boreal summer and over the Western Pacific in boreal winter, with an interannual variability of up to 20% due to the coupled ocean-atmosphere circulation system (Fiehn et al., 2018; Butler et al., 2018; Tegtmeier et al., 2020).

Taking into account all tropical measurements performed during the last two decades under the assumption of no long-term changes of brominated VSLSs, the current estimate for bromine SGI amounts to 2.1 (0.5–4.4) ppt Br, dominated by $CHBr_3$ and CH_2Br_2 (**Table 1-5**). The wider uncertainty range with respect to the last Assessment is in agreement with recent modeling studies that highlight the significant dependence of bromine SGI on the seasonal and regional variability of surface emissions (Fiehn et al., 2017; 2018; Tegtmeier et al., 2012; Keber et al., 2020), as well as on the variable photochemical degradation lifetime of VSL SGs over shallow and rapid convective regions (Aschmann and Sinnhuber, 2013; Fernandez et al., 2014; Butler et al., 2018; Filus et al., 2020).

At the NH extratropical tropopause, total organic bromine from VSLSs of up to 4.0 ± 1.2 ppt (fall) and 5.2 ± 1.3 ppt (winter) was detected during the TACTS (2012), WISE (2017), and PGS (2015/16) aircraft campaigns (**Figure 1-9**; Keber et al., 2020). These observations indicate that the seasonal SG troposphere-to-stratosphere transport over the NH mid- to high latitudes is significantly higher than the annual mean tropical injection of 2.1 (0.5–4.4) ppt (**Table 1-5**). The increase of SG mixing ratios with latitude, in particular during winter (**Figure 1-9**; Keber et al., 2020), is most probably related to the lifetime variations with season and latitude (*Annex*), although the influence of higher regional or seasonal sources cannot be excluded.

Stratospheric injection of bromine PGI across the extratropical tropopause was estimated as 1.5 ± 0.6 ppt, with a range of 0.2–3.3 ppt, depending on latitude (Rotermund et al., 2021). No new tropical PG observations have become available since the last Assessment. Global modeling studies confirm that a

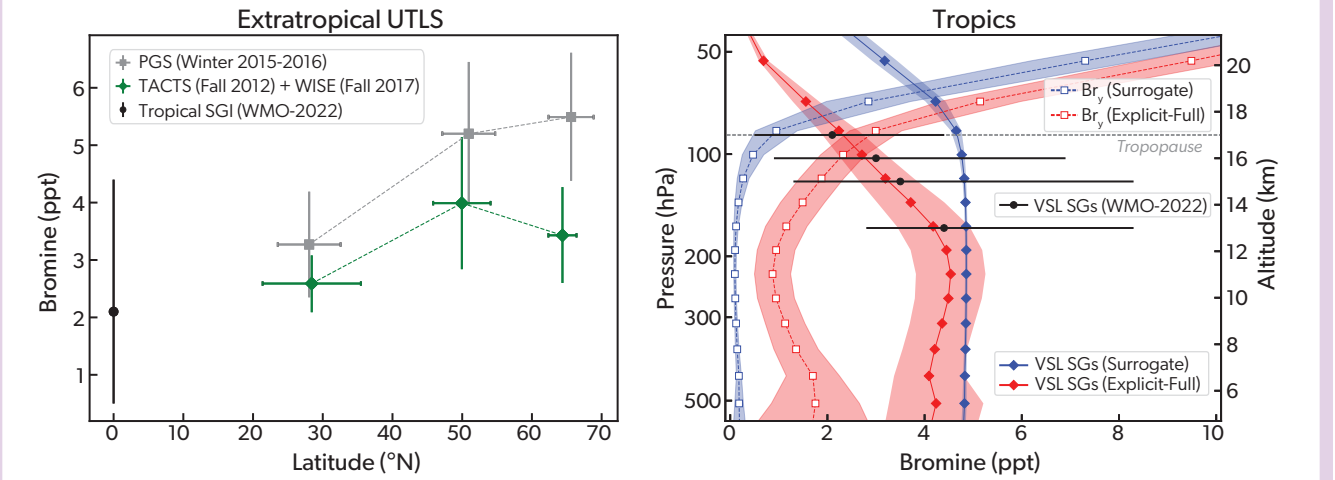

Figure 1-9. *(left panel)* Latitudinal cross section of total brominated VSL SGs observed during the PGS (gray) and WISE+TACTS (green) extratropical aircraft campaigns, binned by latitude just below the local tropopause (error bars denote 1-sigma uncertainty). Tropical SGI of 2.1 ppt Br is also shown (black; **Table 1-6**). Adapted from Keber et al. (2020). *(right panel)* Tropical vertical profile of brominated VSL SGs (filled diamonds) and inorganic bromine (Br_y; empty squares) for two different tropospheric chemical schemes: a simplified approach considering long-lived CH_3Br as a surrogate for VSL SGs (blue) and an explicit mechanism considering major and minor VSL SGs, as well as a full chemical treatment of Br_y processing in the troposphere (red). Note that at and below the tropopause, VSL PGs are assumed to be equal to Br_y, whereas above the tropopause Br_y also accounts for long-lived ODS bromine degradation. Shaded areas represent the annual spatiotemporal variability (mean ± 1-sigma) within the tropics (20°N–20°S). Black filled circles and bars show the assessed total brominated VSL SGs observational mean ± range within the TTL (see **Table 1-5**). WISE = Wave-driven ISentropic Exchange; TACTS = Transport and Composition in the Upper Troposphere/Lowermost Stratosphere; PGS = POLSTRACC (The Polar Stratosphere in a Changing Climate), GW-LCYCLE (Investigation of the Life cycle of gravity waves) and SALSA (Seasonality of Air mass transport and origin in the Lowermost Stratosphere). [Adapted from Fernandez et al., 2021.]

significant fraction of the VSLS bromine input to the stratosphere occurs via PGI, with tropical mean annual values ranging from 2.3 to 3.5 ppt (Tegtmeier et al., 2020; Fernandez et al., 2021). Model simulations with different degrees of complexity demonstrate that an explicit chemical modeling of tropospheric VSLSs is required to reproduce VSL SG observations in the TTL (**Figure 1-9**). The explicit modeling approach suggests significant enhancement of the VSL PG contribution to the total inorganic bromine (Br_y) in the lower stratosphere. Since inorganic PGs can directly destroy ozone, while the organic SGs first have to undergo chemical degradation, these relative contributions are important when analyzing the VSLS impact on stratospheric ozone.

In summary, a total of 5 (3–7) ppt bromine is injected to the stratosphere, with a contribution from SGI accounting for 2.1 (0.5–4.4) ppt Br and the remaining fraction of 2.8 (1.8–4.2) ppt Br delivered via PGI (**Table 1-6**). The new assessed range is very similar to the one provided in previous Assessments and indicates that the trend in the VSLS contribution to stratospheric bromine, if any, is very small (Tegtmeier et al., 2020).

1.3.2.3 Input of VSLS Iodine to the Stratosphere

In previous Assessments, stratospheric injection of iodinated VSLSs have considered only gas-phase iodine. As new evidence suggests a rapid shift in the partitioning between gas-phase and particulate iodine (Koenig et al., 2020), in this Assessment iodinated PG entrainment also includes the contribution of particulate iodine (inorganic iodine taken up in particles). The transport of particulate iodine across the tropopause can enable inorganic iodine, either from recycled inorganic SGs or from photodecomposed organic SGs, to reach the stratosphere. Given the larger stratospheric ozone destruction efficiency of a single iodine atom compared with that of bromine and chlorine (Klobas et al., 2021), small amounts of iodine reaching the stratosphere can contribute to stratospheric ozone loss (Koenig et al., 2020; Cuevas et al., 2022; see *Chapter 4*).

The contribution of iodine VSL SGs in the form of CH_3I to the stratospheric halogen loading remains identical to previous Assessments (0–0.1 ppt). Estimates derived from observations (**Table 1-5**) and global modeling studies suggest that CH_3I mixing ratios rapidly decay to close to zero just before reaching the tropical tropopause (Saiz-Lopez et al., 2015; Tegtmeier et al., 2013). The CH_3I decomposition has been suggested to make up for 30–40% of the inorganic iodine injection to the stratosphere (Koenig et al., 2020). The dominant fraction arises from the inorganic iodine SGs (i.e., HOI and I_2) released from the ocean surface and rapidly processed during their transport to the stratosphere (see *Section 1.3.1.3*).

Current quantitative measurements of IO radicals and particulate iodine performed during tropical and subtropical campaigns (TORERO, CONTRAST, and ATom) suggest that 0.77 ± 0.10 ppt of total iodine PGI can reach the tropopause (**Figure 1-10**; Koenig et al., 2020). In the upper troposphere, gas-phase iodine dominates, and observations are compatible with model simulations only if ice recycling is assumed (Saiz-Lopez et al.,

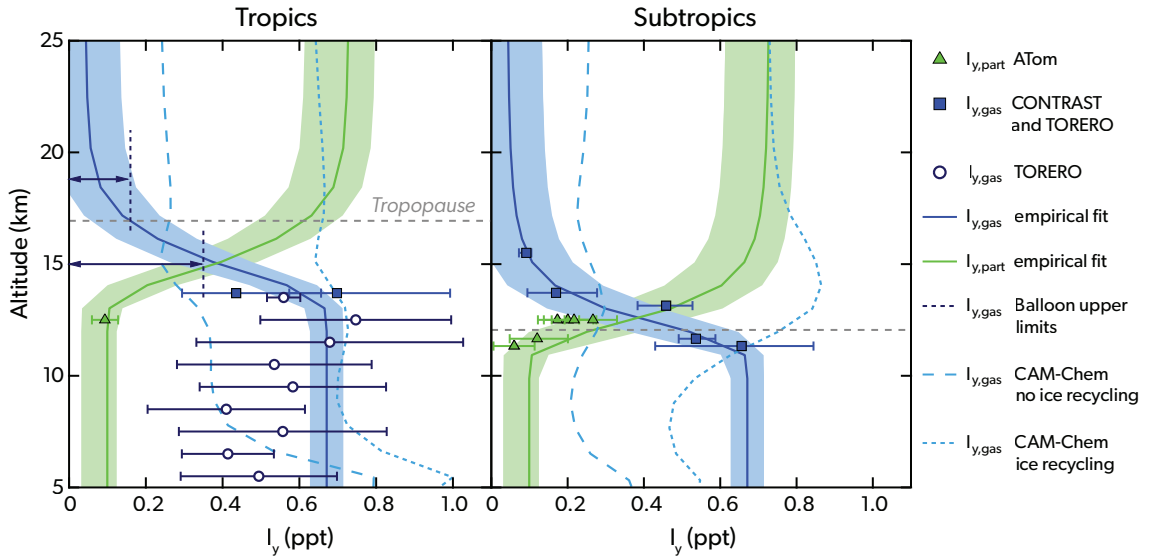

Figure 1-10. Vertical profiles of iodinated VSLSs within the tropics (20°N–20°S; left) and subtropics (20–60°N and 20–60°S; right). Aircraft-based total gas-phase iodine ($I_{y,gas}$, blue) and particulate iodine ($I_{y,part}$, green) mixing ratios are shown with different symbols depending on the campaign (ATom, CONTRAST, and TORERO [Tropical Ocean tRoposphere Exchange of Reactive halogen species and Oxygenated VOC]). Filled symbols indicate values in the UTLS, while tropospheric profiles are shown with empty symbols (error bars denote 1-sigma of observations plus 30% of box-model uncertainty, added in quadrature). Dark-blue vertical dashed-lines in the left panel indicate balloon-borne $I_{y,gas}$ upper-limit estimations during twilight (Butz et al., 2009) above and below the tropopause (light-gray horizontal dashed lines). Blue and green solid lines represent an empirical fit based on observed H_2O/O_3 ratios (shading denotes 1-sigma uncertainty) assuming a constant total stratospheric iodine abundance ($I_{y,gas}$ + $I_{y,part}$ = 0.77 ppt). CAM-Chem model output considering only gas-phase iodine with two different chemical schemes are shown in cyan. [Adapted from Koenig et al., 2020 and Saiz-Lopez et al., 2015.]

2015). However, in the upper TTL, empirical fits of the new observations suggest that the efficient gas-to-particle multiphase repartitioning results in particulate iodine being the dominant contribution of the 0.77 ± 0.10 ppt iodine injection (Koenig et al., 2020). The particulate iodine formation results in a net reduction of gas-phase iodine consistent with balloon-borne upper limits of the latter (Bosch et al., 2003; Butz et al., 2009). Given the large uncertainties and unknowns regarding iodine uptake and sedimentation on stratospheric aerosols, the overall gas-to-particle PGI partitioning currently cannot be distinguished. Estimations of the iodine entrainment into the stratosphere, and consequently of the iodine impact on the ozone layer, should be taken with caution.

Based on the available compendium of iodine measurements, we provide a new range of VSLS iodine input to the stratosphere of 0.3–0.9 ppt (**Table 1-6**), which is higher than the range of 0–0.8 ppt given in the last Assessment (Engel, Rigby et al., 2018). Stratospheric iodine input is dominated by inorganic

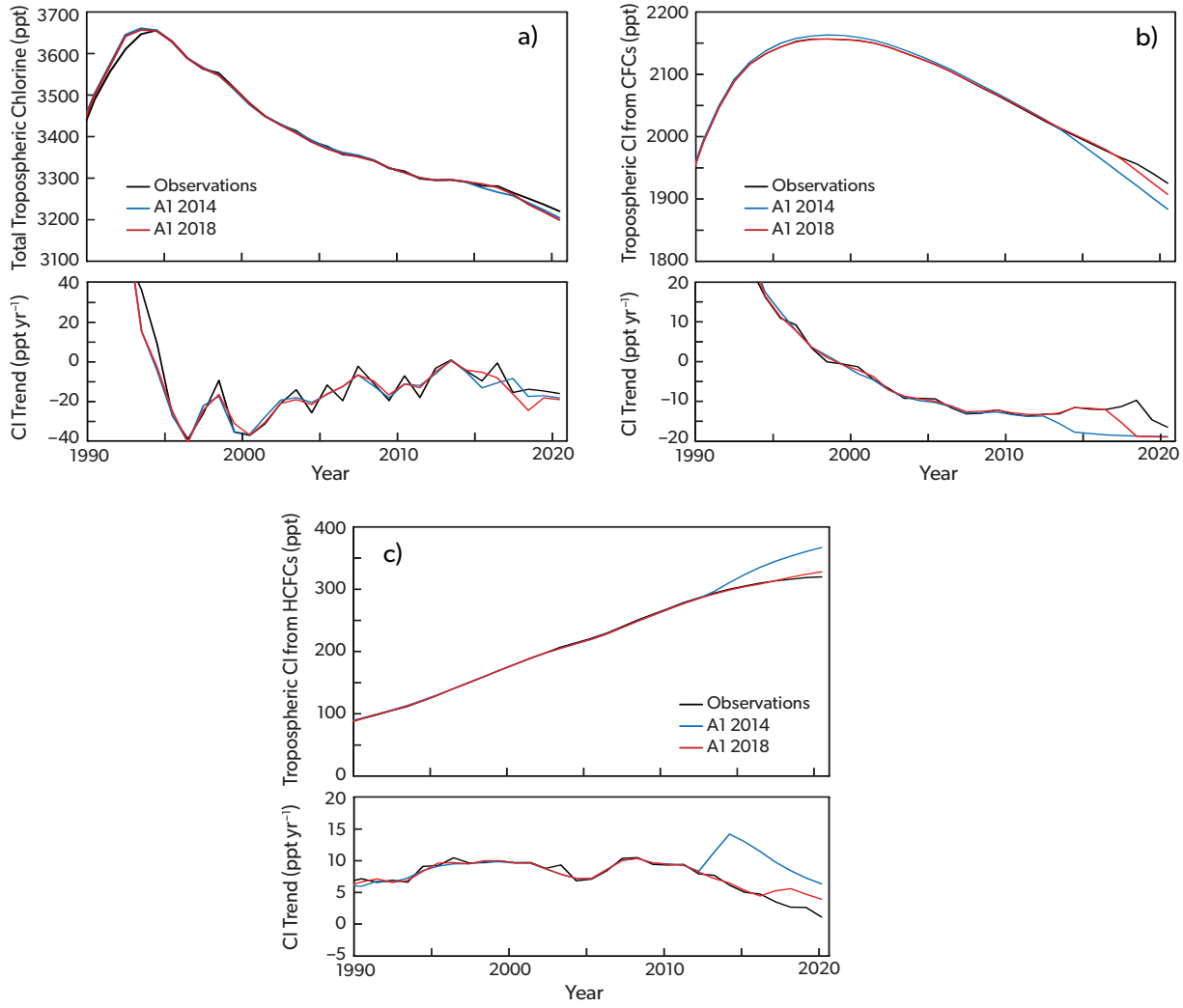

Figure 1-11. (a) Near-surface total tropospheric organic chlorine from the combined global ground-based measurement networks (black line), in comparison to the A1 scenarios from the 2014 (blue line) and 2018 (red line) Assessments. The observed global annual mole fractions of CFC-11, CFC-12, CFC-113, CH_3CCl_3, CCl_4, CH_3Cl, HCFC-22, HCFC-141b, HCFC-142b, and halon-1211 were determined from NOAA and AGAGE data. The observed global annual mole fractions of CFC-114, CFC-112, and CFC-113a were derived from AGAGE and UEA/FZJ data. Values for CFC-115 and CFC-13 were from AGAGE only. Total organic chlorine also includes contributions from VSL SGs (AGAGE and NOAA: CH_2Cl_2, and C_2Cl_4; AGAGE only: $CHCl_3$; see also **Table 1-6**). Continuous observations of these three species from AGAGE and NOAA are available only back to the mid-1990s. Between 1990 and 1995, the same constant mixing ratio as in the 2018 Assessment was used for CH_2Cl_2. Contributions from $CHCl_3$ and C_2Cl_4 before 1995 were not considered, as no in situ measurements are available. For species that are not included in the calculation of the scenarios (some minor ODSs and VSLSs), the observed values were added to the scenario totals in order to provide a comparison based on the same set of compounds. Panels (b) and (c) show the same as panel (a) for the sum of the tropospheric chlorine contents of the CFCs and the tropospheric chlorine content of all HCFCs, respectively.

Table 1-7. Contributions of long-lived ODSs and VSL SGs to total chlorine in the troposphere. Chlorine mid-year mole fractions were derived using AGAGE, NOAA, and UEA/FZJ data. Shown are absolute and relative contributions to total Cl over five-year periods, as indicated. For the average rate of change, the values in parentheses represent the standard deviation of the annual growth rates during the respective period, which reflects the observed variability (1 standard deviation). Changes in total chlorine were calculated relative to values at the beginning of each period (e.g., for 2008–2012, relative to 3342 ppt total chlorine in 2008). We refer to these periods as five-year periods, as they are based on annual average values, e.g., from the beginning of 2016 to the end of 2020. Values for past years differ slightly from previous Assessments because of updated calibration information, different methods for determining global mean mole fractions, and rounding errors.

Compound	Total Cl (ppt)			Contribution to Total Cl (%)			Average Rate of Change of Total Cl (ppt yr^{-1})		
	2012	2016	2020	2012	2016	2020	2008–2012	2012–2016	2016–2020
All CFCs	2026	1977	1925	61.5	60.3	59.8	–13.0 (0.7)	–12.1 (0.7)	–13.0 (3.1)
CCl_4	340	322	307	10.3	9.8	9.6	–4.7 (0.3)	–4.4 (0.3)	–3.9 (0.5)
HCFCs	286	310	320	8.7	9.4	9.9	9.0 (0.7)	5.9 (1.3)	2.5 (1.0)
CH_3CCl_3	16	7.8	4.2	0.48	0.24	0.13	–4.1 (0.9)	–2.0 (0.5)	–0.9 (0.2)
Halon-1211	3.96	3.55	3.16	0.12	0.11	0.1	–0.07 (0.01)	–0.10 (0.00)	–0.10 (0.01)
Total Controlled Cl	2672	2621	2559	81.1	79.9	79.5	–12.9 (0.1)	–12.8 (0.8)	–15.1 (2.4)
CH_3Cl	539	556	547	16.4	17	17	–1.5 (5.4)	4.3 (3.7)	–2.3 (5.7)
VSLSs[1]	84	103	113	2.5	3.1	3.5	2.3 (3.1)	4.9 (5.2)	2.5 (3.3)
Total Cl	3295	3281	3220				–12.1 (8.0)	–3.6 (4.7)	–15.1 (3.6)

[1] Not including CH_2ClCH_2Cl (due to the absence of near-surface long-term trends), as well as SGI.

iodine plus a minor contribution from organic iodine. The non-zero minimum edge is obtained assuming that total iodine in the lower stratosphere is not preserved (Koenig et al., 2020), whereas no central value is provided due to the very large uncertainties regarding the gas-to-particle iodine partitioning. If the upper limit of the range is considered, the impact of iodine on tropical lower-stratospheric ozone could be as large as that of brominated VSLSs.

1.4 CHANGES IN ATMOSPHERIC HALOGENS

1.4.1 Tropospheric and Stratospheric Chlorine Changes

1.4.1.1 Tropospheric Chlorine Changes

The total amount of chlorine from ODSs that were controlled under the original Montreal Protocol is continuing to decline, as the overall emissions are smaller than the rate at which these ODSs are destroyed. Total tropospheric chlorine has been decreasing continuously since its peak abundance observed during 1993–1994 (**Figure 1-11a**). The maximum annual average total chlorine observed from controlled and uncontrolled substances was about 3660 ppt in 1994. The rate of decrease slowed from 39 ppt yr^{-1} in 1995–1996 to 3.6 ppt yr^{-1} between 2012 and 2016, then accelerated again to an average 15.1 ± 3.6 ppt yr^{-1} between 2016 and 2020. This recent acceleration is predominantly due to changes in substances not controlled by the Montreal Protocol, namely CH_3Cl and VSLSs. The concentrations of tropospheric chlorine shown in **Figure 1-11a** do not include several minor species (i.e., any species contributing less than 1 ppt of chlorine; see *Introduction*), but these have very little influence on the total or its trend. When looking at total chlorine from controlled ODSs only, there is still a recent acceleration in the rate of decline (though much less pronounced), from an average rate of 12.8 ± 0.8 ppt yr^{-1} between 2012 and 2016 to 15.4 ± 2.4 ppt yr^{-1} between early 2016 and late 2020 (**Table 1-7**). **Figure 1-11b and c** show the temporal evolution of combined tropospheric chlorine from CFCs and HCFCs, respectively. It is apparent that the former has not declined as rapidly as expected in the A1 scenarios from the 2014 and 2018 Assessments, although there is a more recent CFC-11-driven reduction in the growth rate; in contrast, the latter has not increased as rapidly as expected and is approaching near-zero growth rates in 2020. The tropospheric chlorine contribution from HCFCs has continued to increase, reaching 320 ± 3 ppt in 2020. However, the annual average growth rate of chlorine from HCFCs decreased from 5.9 ± 1.3 ppt yr^{-1} reported in the 2018 Assessment to 2.5 ± 1.0 ppt yr^{-1} during 2016–2020. Total tropospheric chlorine (including uncontrolled substances) reached 3220 ppt in 2020, which is equivalent to a 12% reduction from the previous maximum, and about 1.8% lower than in 2016.

1.4.1.2 Stratospheric Chlorine Changes

Long-term changes in stratospheric inorganic chlorine are driven by changes in tropospheric chlorine and transport variability. The total organic chlorine in the troposphere has been declining since the early 1990s (**Figure 1-11**), and as a consequence, a decline in stratospheric inorganic chlorine is also expected. The timing of the trend reversal is shifted between the two atmospheric regions according to timescales of transport and photochemical conversion. Details of the stratospheric trend will also be impacted by changes in the stratospheric circulation and the relative contributions of SGs.

Total column abundance for hydrogen chloride (HCl) and chlorine nitrate ($ClONO_2$) and their summation (Cl_y) at Jungfraujoch (46.5°N) and Lauder (45.0°S) are presented in **Figure 1-12**, with the corresponding trends listed in **Table 1-8**. HCl shows a statistically significant decrease from 1997 to 2020 at the two stations of –0.41 ± 0.15% yr^{-1} and –0.56 ± 0.12% yr^{-1}, respectively (updated from Mahieu et al., 2014a), similar to the trend reported in the last

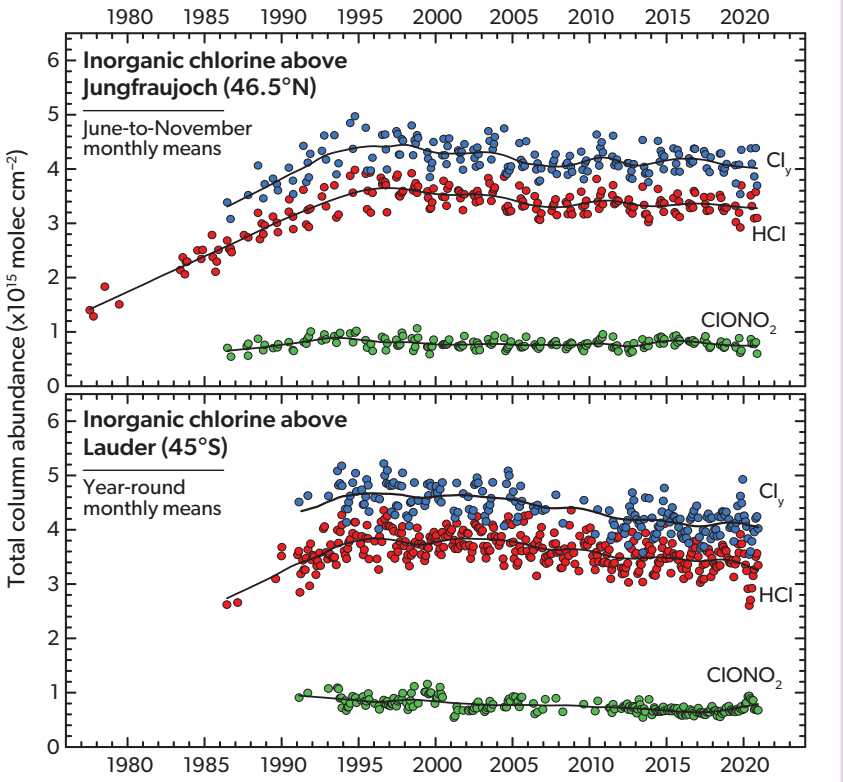

Figure 1-12. Time series of monthly mean total column abundances for the two main stratospheric chlorine reservoirs HCl (red circles) and $ClONO_2$ (green circles) derived at two mid-latitude stations, Jungfraujoch (46.5°N) and Lauder (45.0°S), in the framework of the NDACC network. The HCl and $ClONO_2$ sum is a good proxy of total inorganic chlorine and is denoted as Cl_y (blue circles). For Jungfraujoch, the datasets are restricted to June through November in an effort to limit the variability caused by atmospheric transport and subsidence during winter and spring. The continuous lines come from non-parametric least-squares fits involving an integration time of about three years and help to visualize the non-monotonic and non-linear changes in stratospheric chlorine.

Table 1-8. Observed inorganic chlorine trends for the total column and for the upper atmosphere. Trends (% yr^{-1}) of HCl and $ClONO_2$ and their summation (Cl_y) are based on the FTIR column time series shown in **Figure 1-12**. Near-global (60°S–60°N) trends in HCl averaged over the middle stratosphere are based on trend profiles from GOZCARDS, Aura MLS, and ACE-FTS, and trends of $ClONO_2$ are from ACE-FTS. All uncertainties are estimated at 2-sigma.

Data Source/Location	Cl_y Species	Altitude Region	Rate of Change (% yr^{-1})	Time Period
FTIR NDACC Jungfraujoch (46.5°N)	HCl	Total column	−0.41 ± 0.15	1997–2020
	$ClONO_2$		−0.07 ± 0.39	
	Cl_y		−0.34 ± 0.15	
FTIR NDACC Lauder (45.0°S)	HCl	Total column	−0.56 ± 0.12	1997–2020
	$ClONO_2$		−0.97 ± 0.41	
	Cl_y		−0.65 ± 0.11	
GOZCARDS1 (60°S–60°N)	HCl	68 to 10 hPa	−0.56 ± 0.26	1997–2020
Aura MLS (60°S–60°N)			−0.28 ± 0.21	2005–2020
ACE-FTS (60°S–60°N)	HCl	68 to 10 hPa	−0.30 ± 0.17	2004–2020
	$ClONO_2$	23–8 hPa	−0.53 ± 0.14	2004–2020

[1] GOZCARDS trends are derived from merged HCl data (updated from Froidevaux et al., 2015) based on a multi-linear regression model that accounts for seasonal and shorter-period cycles, as well as longer-term variations relating to the QBO, ENSO, and solar flux (Froidevaux et al., 2019). From 2011 onwards, no ACE-FTS data are used in GOZCARDS. The 2-sigma error bars are based on a bootstrap residual resampling method.
[2] MLS trends are based on version 4 Aura MLS data derived with the regression model and bootstrap method described in footnote 1 of this table.
[3] ACE-FTS trends are based on version 4.1 data (HCl data updated from Bernath and Fernando, 2018; $ClONO_2$ data updated from Bernath et al., 2021). Trends are derived from a linear trend calculation applied to seasonally averaged data with the dynamical variability removed based on a regression model that includes N_2O time series in the fitting. The errors are 2-sigma estimates, taking into account the autocorrelation of the residuals.

Assessment for 1997–2016. In contrast, $ClONO_2$ shows a significant decrease only at the SH station (–0.97 ± 0.41% yr^{-1}), while at the NH station the time series is flat with no significant trend (–0.07 ± 0.39% yr^{-1}). Interestingly, the SH $ClONO_2$ abundance in 2020 was higher than during any previous year since 2014.

The long-term decreases in HCl and $ClONO_2$ lead to a significant negative trend in Cl_y, which is stronger in the SH (–0.65 ± 0.11% yr^{-1}) than in the NH (–0.34 ± 0.15% yr^{-1}). Shorter-term temporal variability in inorganic chlorine (e.g., increasing values at Jungfraujoch between 2005 and 2011) have been attributed to circulation changes in the NH (Mahieu et al., 2014a). Such fluctuations seem to appear somewhat regularly for the NH HCl and Cl_y data (**Figure 1-12**). Transport anomalies are known to influence stratospheric gases in different ways in the two hemispheres. HCl columns have been found to be sensitive to variations in the lower-stratospheric age of air and have been used to infer differences in lower-stratospheric age of air between the NH and SH (Strahan et al., 2020; Prignon et al., 2021).

Stratospheric HCl trends from limb-viewing satellite observations (**Table 1-8**) confirm the FTIR-based findings for the near-global scale (60°S–60°N). The merged satellite record from the Global OZone Chemistry And Related trace gas Data records for the Stratosphere (GOZCARDS) yields decreasing HCl of –0.56 ± 0.26% yr^{-1} for 1997–2020 (updated from Froidevaux et al., 2015), consistent with the FTIR column trends. If the evaluations are constrained to a shorter time period, the satellite records from the Aura Microwave Limb Sounder (MLS) and the Atmospheric Chemistry Experiment-Fourier Transform Spectrometer (ACE-FTS) suggest trends of –0.28 ± 0.21% yr^{-1} (2005–2020) and –0.30 ± 0.17% yr^{-1} (2004–2020), respectively (updated from Froidevaux et al., 2015, 2019; Bernath and Fernando, 2018; Bernath et al., 2021). These provide convincing evidence that the rate of decline in middle-stratospheric HCl slowed down considerably after 2004. Taking into account the time shift between the troposphere and the middle/upper stratosphere of about four years, this is in good agreement with surface chlorine abundances, which decreased by –0.50 ± 0.03% yr^{-1} for 1992–2016 and slowed down to a decrease of –0.36 ± 0.02% yr^{-1} for 2000–2016. ACE-FTS measurements suggest that the upper-stratospheric HCl (and thus Cl_y) decline slowed even further after around 2010, when the rapid initial decline of species with shorter atmospheric lifetimes, such as CH_3CCl_3, became smaller (Bernath and Fernando, 2018; Bernath et al., 2020). In addition, model simulations in good agreement with satellite observations suggest that this HCl decline is about 15% slower than it would be without the contribution from chlorinated VSLSs (Hossaini et al., 2019), demonstrating that VSLSs have offset a portion of stratospheric chlorine reductions since the mid-2000s.

1.4.2 Tropospheric and Stratospheric Bromine Changes

1.4.2.1 Tropospheric Bromine Changes

The total amount of bromine from ODSs that were controlled under the original Montreal Protocol is continuing to decline, as the overall emissions are smaller than the rate at which these ODSs are destroyed. Results from the AGAGE and NOAA networks indicate that total tropospheric bromine from the controlled substances (CH_3Br and halons) reached a maximum in 1999, with an annual average value of 17.1 ppt. Both the timing and the

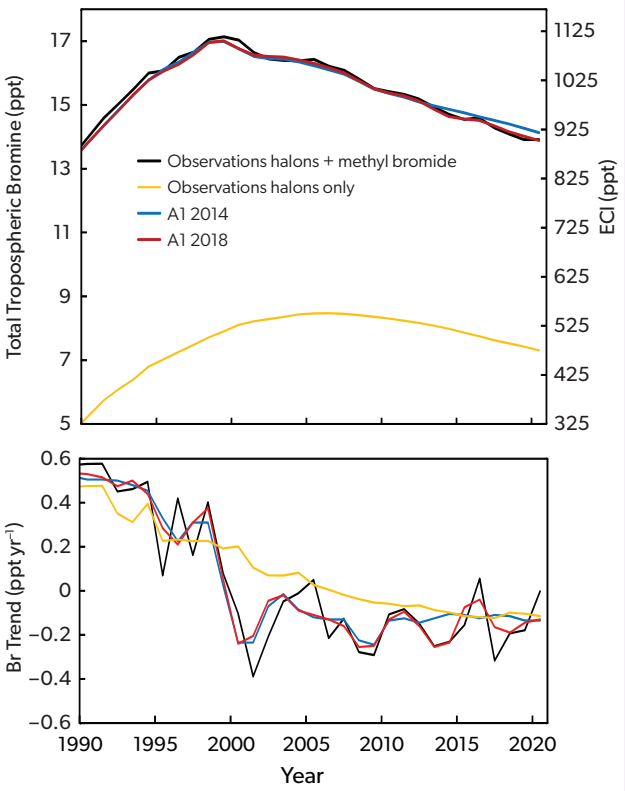

Figure 1-13. Time series of near-surface tropospheric bromine mole fractions (sum of halons and CH_3Br, black line) and those of halons only (yellow line) in comparison to the A1 scenarios from the 2014 (blue line) and 2018 (red line) Assessments. Long-term global surface observations are not available for brominated VSLSs, and therefore their contribution is not included here. Values in the upper panel are also expressed as equivalent chlorine (right-hand axis), using a value of α = 65 to account for the higher efficiency of bromine in catalyzing ozone destruction. All values are derived from a merged dataset based on NOAA, AGAGE, and UEA/FZJ data.

mole fraction are slightly different than those given in previous Assessments (i.e., 16.9 ppt in 1998) due to the effects detailed in the *Introduction*. Since 1999, the abundance of tropospheric bromine has been decreasing continuously (**Figure 1-13**), reaching a value of 13.9 ppt by 2020. While CH_3Br has been decreasing since the late 1990s (except for the brief increase in 2015–2016 and the stable period after 2017; see *Section 1.2.7*), bromine from halons started decreasing only around 2006. From 2012 to 2016, total controlled bromine declined at a rate of 0.15 ± 0.14 ppt yr^{-1} (1% yr^{-1}), and this rate increased to 0.18 ± 0.05 ppt yr^{-1} during 2016–2020. Halons contributed ~64% to this decline (2012–2016: ~70%), with CH_3Br accounting for the remainder. Similar to the last Assessment, the decrease in total bromine over the past five-year period was therefore again dominated by a decrease in halon abundances. The observed decrease in total controlled bromine is in overall good agreement with the decrease projected by the A1 scenario from the last Assessment (Carpenter, Daniel et al., 2018). Note that the tropospheric bromine total discussed

here does not include contributions from brominated VSLSs of around 5 ppt (see *Section 1.4.2.2*), as no trends from AGAGE or NOAA surface measurements of these gases are available.

1.4.2.2 Stratospheric Bromine Changes

Total stratospheric inorganic bromine (Br_y) originates from long-lived ODSs, mainly CH_3Br and halons, as well as from VSLSs, both in organic and inorganic forms. Estimates of stratospheric Br_y rely on two different methods. The first method (SG-based) sums up all bromine in the form of ODSs and VSL SGs found at the stratospheric entry level (e.g., Brinckmann et al., 2012; Navarro et al., 2015). This approach provides the contribution from the measured species at a high accuracy, but any bromine entering the stratosphere in inorganic form needs to be added to this to get true total bromine. The second method infers Br_y from atmospheric measurements of bromine oxide (BrO) coupled with photochemical modeling of the Br_y partitioning (e.g., Dorf et al., 2008; Parrella et al., 2013; Werner et al., 2017) or, following an equivalent methodology, from measurements of bromine nitrate ($BrONO_2$; Höpfner et al., 2021). This approach is ideally applied in the middle and upper stratosphere, where all bromine is present in inorganic form. If the method is applied in the lower stratosphere, additional measurements of the organic bromine from long-lived ODSs and VSL SGs are needed to determine total bromine (Wales et al., 2018; Werner et al., 2017). Uncertainties can also arise from the BrO or $BrONO_2$ measurements, as well as from the model-derived partitioning of Br_y, and depend on the measurement technique and probed photochemical regime.

Time series of Br_y estimates derived from the two methods are shown in **Figure 1-14a**. For the SG-based method, observations of the long-lived CH_3Br and halons were added to time-invariant and current best estimates of SG and PG injections from brominated VSLSs (5 ± 2 ppt; **Table 1-6**) to derive Br_y estimates (blue lines). Given that CH_3Br and halons are sufficiently long-lived to be transported into the stratosphere, the amounts of their stratospheric injection are taken as global mean surface values (**Figure 1-13**). For the BrO-based method, total column and vertically resolved BrO measurements were used to obtain Br_y estimates and plotted against the "year of stratospheric entry" (symbols in **Fig. 1-14a**). Ground-based measurements from the NH station Harestua (60°N) suggest a very slow decline with some year-to-year variability. Values measured in 2020, and mapped to a stratospheric entry in 2016, suggest 19.6 ppt of total bromine, in excellent agreement with the SG-based method assuming a

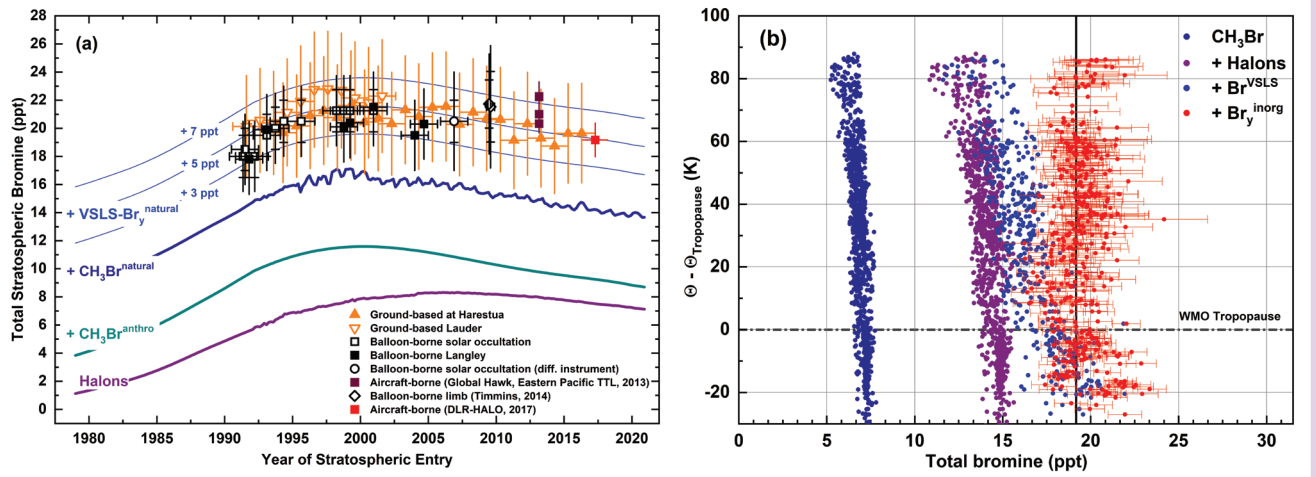

Figure 1-14. (a) Changes in total stratospheric Br_y (ppt) derived from balloon-borne (black open and filled symbols; update of Dorf et al., 2006) and airborne (purple filled squares from Werner et al., 2017; red filled square from Rotermund et al., 2021) BrO observations and from ground-based UV-visible measurements of stratospheric BrO made at Harestua (60°N) and Lauder (45°S) stations (filled and open orange triangles, respectively; adapted from Hendrick et al., 2007, 2008). All UV-visible measurements of stratospheric BrO were evaluated using a common BrO absorption cross section (based on Wahner et al., 1988), frequency-shifted to match the wavelength scale (Wilmouth et al., 1999). For the balloon-borne observations, exclusive of those using the Langley method, the outer and inner capping of the error bars correspond to the precision and accuracy of the estimates, respectively. For the ground-based measurements (triangles), the error bars correspond to the total uncertainties in the Br_y estimates. For stratospheric data, the date corresponds to the time when the air was last in the troposphere, i.e., sampling date minus estimated mean age of the stratospheric air parcel. Time series of halons and CH_3Br, with the latter split into the natural and anthropogenic fraction, have been updated (NOAA data only; see Carpenter, Reimann et al., 2014, for details). The blue lines show the expected stratospheric Br_y, assuming an additional input of 3, 5, and 7 ppt of brominated VSLSs, respectively. For tropospheric data, the date corresponds to the sampling time. This figure updates Figure 1-16 from the previous Assessment (Engel, Rigby et al., 2018). (b) Inferred total bromine as a function of potential temperature distance from the WMO tropopause during the WISE campaign in fall 2017. The organic bromine species are summed up according to their Br atomicity: CH_3Br (dark blue), sum of four halons (purple), and brominated VSLSs (light blue). The inferred inorganic Br_y is subsequently added (red), resulting in the UTLS total bromine. The solid black line represents the LS weighted mean total bromine of 19.2 ± 1.2 ppt. [Adapted from Rotermund et al., 2021.]

VSLS contribution of 5 ppt. Long-term changes based on ground-based BrO measurements indicate a slow decline of total bromine of –0.18 ± 0.04 ppt yr^{-1} (–0.8% yr^{-1}) since 2003. This decrease is in very good agreement with trends in tropospheric bromine, which have ranged between 0 and –0.4 ppt yr^{-1} since the early 2000s (**Figure 1-13**). The $BrONO_2$-based MIPAS satellite estimates focus on the period of maximum Br_y loading, with 21.2 ± 1.4 ppt Br at mid-latitudes corresponding to stratospheric entry between 1997 and 2006 and no significant long-term trend.

Data from the Global Hawk during the ATTREX campaign in the Eastern Pacific in 2013 suggests slightly higher Br_y concentrations of up to 22.3 ppt (purple filled square, **Figure 1-14a**) for air masses directly measured in the tropical tropopause region (Werner et al., 2017). Measurements during the 2017 WISE campaign also found elevated bromine values in the TTL, with a Br_y estimate of 21.6 ± 0.7 ppt (Rotermund et al., 2021), somewhat larger than the Br_y of 19.2 ± 1.2 ppt found in the extratropical and polar lower stratosphere. Both campaigns indicate slightly enhanced total Br_y in the upwelling part of the stratospheric Brewer-Dobson circulation in the tropics compared to those measured in its subsistence region at mid- and high latitudes, in agreement with earlier studies (Navarro et al., 2015; Werner et al., 2017; Wales et al., 2018). The cause of this difference is presently unclear, although it is conceivable that some bromine is heterogeneously taken up on the cold aerosols and cloud particles in the TTL and ultimately removed by sedimentation (Sinnhuber and Folkins, 2006). In addition, the Br_y estimates for both campaigns include directly measured VSLS contributions, which are known to show pronounced spatiotemporal variability in the TTL, with ranges of 0.5–4.4 and 1.8–4.2 ppt for brominated SGI and PGI, respectively (**Table 1-6**).

Observations of total bromine at mid- to high latitudes during the WISE campaign have demonstrated the large impact of transport-related variations on the Br_y budget in this region (**Figure 1-14b**; Rotermund et al., 2021). Bromine-rich air masses from the tropics were found to persistently protrude into the mid-latitude lowermost stratosphere during the boreal summer, causing a pronounced variability in Br_y, with a high bromine region of 20.9 ± 0.8 ppt exceeding the mean value of 19.2 ± 1.2 ppt.

1.4.3 Tropospheric and Stratospheric Iodine Changes

Tropospheric iodine stems mostly from oceanic emissions of

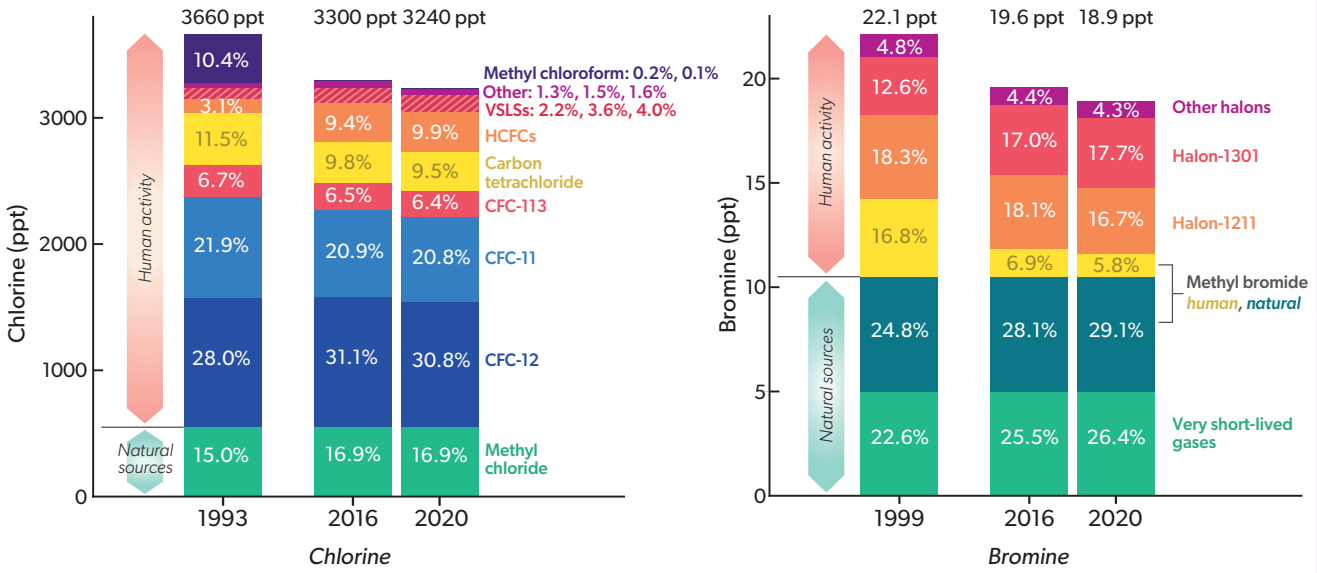

Figure 1-15. Chlorine and bromine input to the stratosphere for a reference year (1993 for chlorine and 1999 for bromine), 2016, and 2020 for different species and classes of compounds. The reference is close to the maximum of chlorine or bromine loading of the troposphere. Mole fractions of long-lived gases were mostly derived from surface observations from global networks (AGAGE and NOAA), except for CH_3Cl before 1995, when observations from both networks were unavailable and values were filled with the simulations from scenario A1 of the previous Assessment (Carpenter, Daniel et al., 2018) as derived from firn air measurements (Montzka, Fraser et al., 2003). The VSLS contributions for bromine are included as a constant 5 ppt, as in previous Assessments. The VSLS chlorine contribution is based on the VSL SG input from a model constrained by observed surface boundary conditions (update of Hossaini et al., 2015). Total VSLS Cl input derived in this way is 80 ppt, 120 ppt, and 130 ppt for years 1993, 2016, and 2020, respectively. For chlorine, HCFCs include HCFC-22, HCFC-141b, HCFC-142b, and HCFC-124; "other" includes contributions from minor CFCs (CFC-13, CFC-112, CFC-113a, CFC-114+CFC-114a, and CFC-115) and halon-1211. For bromine, "other halons" is the sum of bromine contained in halon-1202 and halon-2402. Methyl chloride is counted as having purely natural sources, despite some indications of anthropogenic contributions. The contribution of natural sources to CH_3Br mole fractions was estimated as a constant 5.5 ppt, based on the published firn air and ice core measurements (Butler et al., 1999; Trudinger et al., 2004; Saltzman et al., 2004; 2008), whereas the anthropogenic contribution was estimated by the global surface mole fractions measured by AGAGE and NOAA minus 5.5 ppt.

inorganic iodine in the form of hypoiodous acid (HOI) and molecular iodine (I_2). These emissions are driven by the reaction of ozone with iodide (I^-) at the ocean surface. Since tropospheric ozone over the NH has increased over the last decades, oceanic emissions as well as tropospheric levels of inorganic iodine are likely to have increased in response. Observations reveal a positive trend in iodine in spruce tree rings in the Tibet Plateau (Zhao et al., 2019), as well as in Greenland and Alpine ice cores, with the latter showing a tripling in iodine since 1950 (Legrand et al., 2018). This iodine increase can be explained by model-derived oceanic iodine emissions in the North Atlantic and their increase over the latter half of the 20th century (Cuevas et al., 2018). While observations and models agree on increasing tropospheric iodine levels, it should be noted that the results are accompanied by large uncertainties due to the lack of observational constraints on ozone changes, iodide levels, flux parameterizations, and tropospheric iodine chemistry (Carpenter et al., 2021).

Tropospheric iodine also stems from oceanic emissions of organic iodine in the form of CH_3I. Earlier measurements at remote sites in the western and northern Pacific from the late 1990s to 2011 reported long-term decadal oscillations of atmospheric CH_3I, possibly related to natural oscillations of sea surface temperature (Yokouchi et al., 2012). These results suggest that climate change can impact oceanic trace gas emissions. However, very little updated data on CH_3I tropospheric trends exist to further investigate such impacts. One of the few available datasets consists of observations in the Greater Pearl River Delta region of China during 2001–2018 and shows a significant increase in CH_3I over the measurement period, of 0.08 ± 0.02 ppt yr^{-1}. Given the proximity to densely populated regions, these trends could be related to anthropogenic sources, based on the use of CH_3I as a methylating agent (Zeng et al., 2020).

For stratospheric iodine, no observational trend estimates exist. Assuming iodine injections in particulate form is a plausible entrainment mechanism (Koenig et al., 2020), changes in oceanic emissions and aerosol iodine content could also influence stratospheric iodine levels. Given the large uncertainties in the processes controlling tropospheric particulate iodine formation and reactive transport to the stratosphere, any model-based stratospheric iodine trend can also be expected to have large uncertainties.

1.4.4 Changes in Ozone-Depleting Halogen Abundance in the Stratosphere

Figure 1-15 illustrates the contributions of different ODSs or ODS groups to chlorine and bromine input to the stratosphere during the respective peak years (Cl: 1993, Br: 1999), as well as in 2016 and 2020. In contrast to *Sections 1.4.1.1* and *1.4.2.1*, VSLS tropopause estimates are included here, as these species have strong sinks in the troposphere and therefore ground-based measurements do not reflect the actual amounts reaching the stratosphere. In 2020, total chlorine and bromine entering the stratosphere from controlled and uncontrolled ODSs reached values of 3240 ppt and 18.9 ppt, respectively. Thus, the chlorine and bromine inputs have declined by 11.5% (420 ± 20 ppt) and 14.5% from their peak abundances, respectively, with 1.6% and 3.2% of this decline between 2016 and 2020.

Equivalent effective stratospheric chlorine (EESC) also generally follows the changes in tropospheric ODSs but additionally includes calculations 1) reflecting the ability of bromine to destroy more ozone than chlorine (α-factors of 60 and 65 were used here for mid-latitude and polar winter conditions, respectively; see **Figure 1-16**), 2) addressing the influence of stratospheric lifetime differences between ODSs, and 3) taking into account effects from the transport of air in the stratosphere (timescales of years), which is much slower than in the free troposphere (days to months). As noted in the last Assessment, the traditional use of EESC in 1980 as a benchmark is somewhat arbitrary, as 1) anthropogenically induced ozone loss occurred prior to 1980, and 2) a return to 1980 EESC levels does not imply a recovery of the ozone layer to the 1980 state, ozone being influenced by many additional parameters (e.g., greenhouse gas abundances,

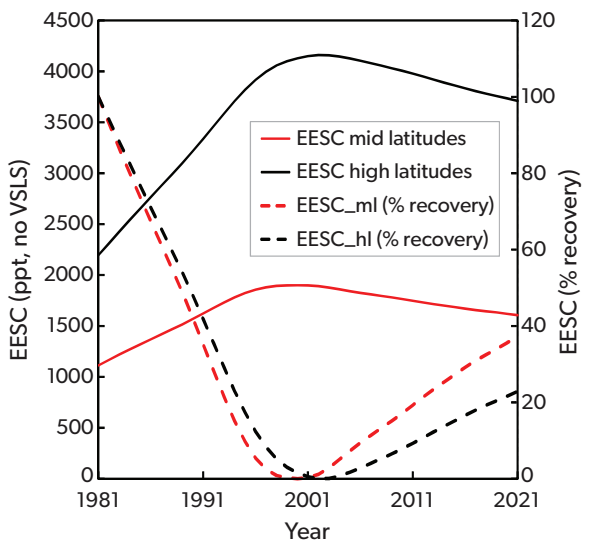

Figure 1-16. Level of EESC (left y-axis) and its percentage recovery toward 1980 benchmark values (right y-axis) using the improved EESC calculation from the 2018 Assessment (Engel, Rigby et al., 2018), which is based on the method by Engel et al. (2018). Solid lines show the EESC at 3 (red) and 5.5 (black) years of mean age, representative of mid-latitude conditions and polar winter conditions, respectively. The dashed lines indicate the percentage of recovery at those same years of mean age, but are shown relative to 1980 levels (defined as 100% recovery) and EESC maxima (defined as 0% recovery). In all cases, the different age spectra were parameterized as suggested by Newman et al. (2007) using half of the mean age as the width of the age spectrum and an inverse Gaussian function as the shape of the age spectrum. The age spectrum has been integrated over a time period of 20 years. Fractional release factors were calculated as in the last Assessment, based on the work by Ostermöller et al. (2017). The same tropospheric data were used as in *Sections 1.4.1.1* and *1.4.2.1*. VSLS contributions to EESC are not included in this calculation, and the higher efficiency of bromine to destroy stratospheric ozone is taken into account (factors of 60 for mid-latitude and 65 for polar winter conditions).

changes in stratospheric dynamics and chemistry). For EESC calculations, an average stratospheric transit time, or mean age, of 5.5 years is again used to reflect typical polar winter conditions, and a three-year mean age for mid-latitude conditions. Here we exclusively use the new and improved formulation of EESC suggested by Engel et al. (2018), introduced in the last Assessment, which also included a comparison to the previously used formulation by Newman et al. (2007). A limitation of the EESC metric is that it does not include contributions from VSLSs (also see **Box 1-3** on VSLS metrics) or nitrous oxide (N_2O), with the latter having an unknown but certainly substantial impact on stratospheric ozone (Ravishankara et al., 2009). Also, more recently, regional variability in EESC has been observed based on observations in the vicinity of the Asian monsoon (e.g., it is between 200 to 300 ppt higher at a mean age of three years; Adcock et al., 2021), which raises some questions on the applicability of this concept for the entire stratosphere, especially for relatively short-lived ODSs with large regional emissions close to stratospheric input regions such as CH_3Cl and CH_3Br (see also *Sections 1.2.5* and *1.2.6*). In addition, a recent study has highlighted the shortcomings of a simple α-factor for bromine, as it does not take into account the global chemistry-climate state, and it suggested the future introduction of an equivalent effective stratospheric benchmark-normalized chlorine (EESBnC) to reflect changes in the rates of bromine- and chlorine-mediated ozone loss (Klobas et al., 2020).

As is shown in **Figure 1-16** and **Table 1-9**, the previously reported decline in EESC has continued. For mid-latitude conditions, we derive an average recovery rate of 37% relative to the 1980 benchmark. This compares to 31% recovery in 2016 reported in the last Assessment. For polar winter conditions, recovery has progressed from 18% in 2016 to 23% in 2020, again relative to 1980, confirming that a full recovery, even only to the 1980 EESC levels, is not expected in the near future.

1.4.5 Tropospheric and Stratospheric Fluorine Changes

Atmospheric fluorine results from the photodissociation of fluorine-bearing source gases including CFCs, halons, HCFCs, HFCs, PFCs, and other compounds. The resulting inorganic fluorine reservoir gas HF is very stable in the atmosphere, and as a consequence, fluorine does not contribute to stratospheric ozone depletion. The primary interest in monitoring inorganic fluorine (F_y) is to provide an independent measure of the accumulation of the associated source gases, many of which are potent greenhouse gases. Among the source gases, HFCs (*Chapter 2*) are of growing interest because their increasing atmospheric abundance is a direct consequence of the restrictions on ODS production and consumption. The regulation of HFCs has been added to the Montreal Protocol in the framework of the Kigali Amendment, in part because they are replacement compounds for substances already regulated under the Protocol.

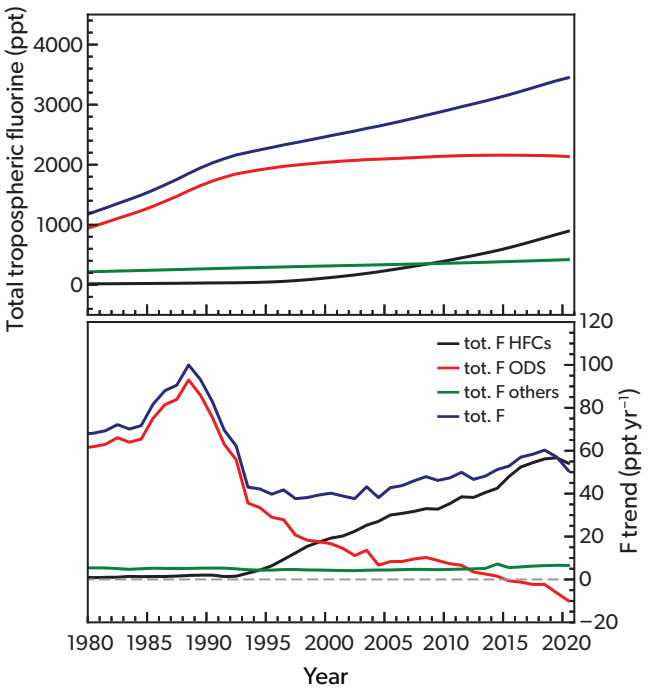

Figure 1-17. *(top)* Tropospheric total fluorine time series and *(bottom)* annual changes from long-lived gases, separated by contributions due to ODSs, HFCs (see *Chapter 2*), and other fluorinated gases (such as SF_6, NF_3, CF_4, not including minor species; see *Introduction*). Mole fractions for ODSs and other fluorinated gases were derived from a merged dataset based on NOAA, AGAGE, and UEA/FZJ data. HFC mole fractions were derived from AGAGE and NOAA data. HFC records prior to regular global measurements were supplemented with estimates from Vollmer et al. (2011), Vollmer et al. (2015b), and the simulated mole fractions from the A1 scenarios in the previous Assessment (Carpenter, Daniel et al., 2018).

Changes in tropospheric fluorine concentrations result from changes in tropospheric concentrations of long-lived ODSs (*Section 1.2*) and HFCs (*Chapter 2*), as well as PFCs and other compounds (*Section 1.5.4*), as shown in **Figure 1-17**. In contrast

Table 1-9. EESC values for 1980 and 2020 as well as when EESC was at its maximum. Values are given for 3 and 5.5 years of mean age (representative of mid-latitude and polar winter conditions, respectively) and are based on the improved method of Engel et al. (2018). Also shown are percentage changes achieved by early 2020 with respect to the maximum and the percentage recovery with respect to the 1980 values.

	EESC 1980 (ppt)	EESC Maximum (ppt) [year]	EESC 2020 (ppt)	Change from Maximum (%)	Recovery to 1980 Level (%)
Mid-Latitude Conditions	1113	1900 [1999]	1607	–15	37
Polar Winter Conditions	2196	4160 [2001]	3710	–11	23

Table 1-10. Observed inorganic fluorine trends for the total column (FTIR) and for the upper atmosphere (ACE-FTS). Trends (% yr^{-1}) of HF and $2xCOF_2$ and their summation (F_y), which represents most of the inorganic fluorine in the stratosphere, are based on mid-latitude FTIR column and ACE-FTS time series shown in **Figure 1-18**. Trends relative to 2004 have been derived for the common time period of observations 2004–2020. All uncertainties are estimated at 2-sigma.

Species	Rate of Change 2004–2020 (% yr^{-1})			
	ACE-FTS (40–50°N)	FTIR (Jungfraujoch, 46.5°N)	ACE-FTS (40–50°S)	FTIR (Lauder, 45.0°S)
F_y	0.87 ± 0.22	0.72 ± 0.19	0.48 ± 0.26	0.05 ± 0.25
HF	0.88 ± 0.20	0.66 ± 0.21	0.59 ± 0.30	0.31 ± 0.22
$2xCOF_2$	1.22 ± 0.49	0.89 ± 0.34	0.28 ± 0.25	–0.45 ± 0.40

to chlorine, total tropospheric fluorine has continued to increase, with a 2016–2020 trend of 57.1 ± 0.8 ppt yr^{-1} corresponding to 1.71 ± 0.02% yr^{-1}. Similarity with the trend reported in the last Assessment (1.7 ± 0.07% yr^{-1} for 2012–2016) suggests stable growth rates of total fluorine. The contributions of the different compound classes to the tropospheric fluorine trend have changed over time. The ODS contribution to the fluorine budget remained relatively constant between 2005 and 2015 and started to decline afterwards. As a result, the fluorine trend due to ODSs alone became negative after 2016, reaching –10 ppt yr^{-1} in 2020. In contrast, the fluorine trend due to HFCs alone increased constantly between 1995 and 2019 and only flattened in 2020, reaching 55 ppt yr^{-1} in 2020.

A good proxy for the total inorganic fluorine (F_y) in the stratosphere is calculated as the weighted sum of the two most abundant fluorinated reservoirs, i.e., hydrogen fluoride (HF) and two times carbonyl fluoride (COF_2). Total column F_y, based on FTIR HF and COF_2 measurements at two mid-latitude stations, has increased steadily since 1989, with a stronger positive trend over the first 15 years of the record (**Figure 1-18**). ACE-FTS satellite data, available since 2004, are mostly consistent with the FTIR data but suggest slightly stronger positive trends. The largest discrepancies exist for the SH, where COF_2 from FTIR measurements has been decreasing, inconsistent with the ACE-FTS satellite record. This is possibly related to transport variability impacting the long-term changes in the two datasets in different ways. In total, F_y in the NH stratosphere has increased at a rate of 0.87 ± 0.22% yr^{-1} (ACE-FTS) and 0.72 ± 0.19% yr^{-1} (FTIR) over the 2004–2020 time period (**Table 1-10**). This long-term change is smaller than tropospheric trends over 2000–2016 of 1.53 ± 0.02% yr^{-1}. While changes in inorganic stratospheric fluorine are largely driven by changes in total tropospheric fluorine, they are also impacted by the efficiency of the fluorine release from the different compound classes. As the relative contributions from different compounds

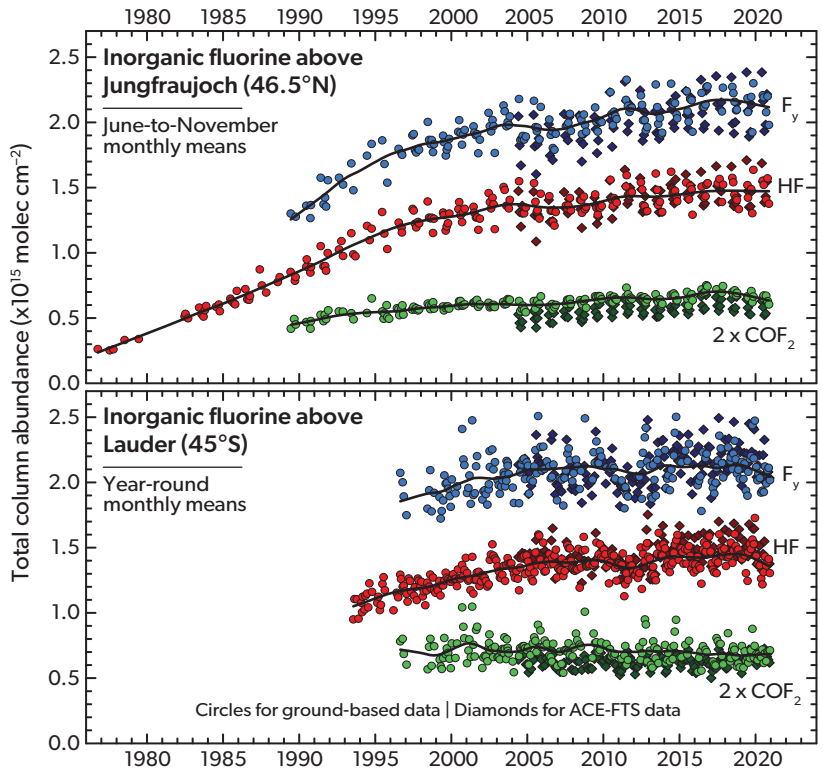

Figure 1-18. Multi-decadal monthly mean total column time series of the two main stratospheric fluorine reservoirs, HF and COF_2, and their summation, F_y, derived at two mid-latitude stations (Jungfraujoch, 46.5°N, and Lauder, 45.0°S) in the framework of the NDACC network and from ACE-FTS occultation measurements (40–50°S and 40–50°N). HF monthly means are reproduced as red symbols; 2 x COF_2 as green symbols. Their summation (blue symbols) is a good proxy of total inorganic fluorine. The satellite and ground-based data are given as diamonds and circles, respectively. Note that the ACE-FTS time series for Fy also includes the contribution of COCIF, a species that cannot be measured from the ground. Finally, non-parametric fits to the FTIR data are shown as continuous thick curves. [Adapted and updated from Prignon et al., 2021.]

have changed over time, a direct correlation of stratospheric and tropospheric fluorine changes is not necessarily expected.

1.5 CHANGES IN OTHER TRACE GASES THAT INFLUENCE OZONE AND CLIMATE

In this section, gases that are not covered by the Montreal Protocol but that indirectly affect stratospheric ozone are discussed. These include long-lived greenhouse gases such as methane (CH_4) and nitrous oxide (N_2O), aerosol precursor gases such as carbonyl sulfide (COS) and sulfur dioxide (SO_2), and other fluorinated chemicals such as sulfur hexafluoride (SF_6) and perfluorocarbons (PFCs). As in the last Assessment, HFCs are covered in *Chapter 2*; while carbon dioxide (CO_2), even though it induces temperature changes that directly alter the chemical rates that produce and destroy ozone, is not included due to its coverage in great detail in the recent IPCC report (IPCC, 2021).

1.5.1 Nitrous Oxide (N_2O) and Methane (CH_4)

Observations of Atmospheric Abundance. N_2O and CH_4 cause the release of chemicals into the stratosphere that catalytically produce and destroy ozone. For an extensive and comprehensive overview of the emissions and abundances of both gases up to 2019, see the recently published IPCC report (IPCC, 2021). In summary, their global abundances have continued to increase, reaching 332.1 ± 0.4 ppb (N_2O) and 1866.3 ± 3.3 ppb (CH_4) in 2019. As an update to the IPCC report, N_2O increased by a further 1.1 ppb between 2019 and 2020 (**Table 1-11**), which is distinctly higher than the average growth rate between 2012 and 2019 of 0.96 ± 0.05 ppb yr^{-1} (IPCC, 2021). CH_4 increased, on average, by 9.3 ± 2.4 ppb yr^{-1} between 2014 and 2019; the recent 2019–2020 change of 10–13 ppb yr^{-1} is at the upper end of this range (**Table 1-11**).

Emissions, Lifetimes, and Radiative Forcings. Several recent publications have found that global N_2O emission increases have been accelerating over the last two decades and by now exceed some of the highest projections (Thompson et al., 2019; Tian et al., 2020; IPCC, 2021). These increases are driven by anthropogenic emissions (mainly from nitrogen additions to croplands), which account for nearly half of the global N_2O emissions in recent years. Due to its much shorter lifetime and its multitude of source and sink processes, the derivation of atmospheric emissions of CH_4 is generally more complex. However, recent increases are likely mainly driven directly (agriculture and fossil fuels) or indirectly (prolonged El Niño conditions) by anthropogenic activities (see Box 5.2 in IPCC, 2021).

In particular, the accelerating increase of N_2O abundances and emissions is a serious threat for stratospheric ozone, as it is the main driver of NO_x-induced ozone depletion and by far the most abundant ODS (Ravishankara et al., 2009; Müller et al., 2021). To illustrate these effects, we here use the maximum range of potential N_2O ODPs from 0.015 to 0.030 as derived by Revell et al. (2015) for various atmospheric scenarios between the years 2000 and 2100. When deriving CFC-11-equivalent emissions from this range, we estimate between 461 and 922 Gg yr^{-1} for 2020, i.e., 5–10 times the ODP-weighted emissions from all CFCs in that year. In addition, the increase in N_2O emissions translates to an increase of 52–104 Gg of CFC-11 equivalent emissions between 2016 and 2020. Anthropogenic emissions N_2O were driving that increase, and these alone (43%, Tian et al., 2020) were equal to more than two times the ODP-weighted emissions from all CFCs in 2020. For context, when compared to the CFC emission peak from 1987, those 2020 anthropogenic N_2O emissions were equal to more than 20 % the ODP-weighted emissions from CFCs in that year.

The direct radiative forcing effects from N_2O and CH_4 in 2020 are estimated at 207 mW m^{-2} and 520 mW m^{-2}, respectively.

1.5.2 Aerosol Precursors: Carbonyl Sulfide (COS) and Sulfur Dioxide (SO_2)

The sulfur-containing gases COS and SO_2 act as precursor gases of stratospheric sulfate aerosol, which can influence halogen chemistry. Stratospheric COS and SO_2 injections occur regularly via troposphere-stratosphere air mass transport or sporadically via explosive volcanic eruptions.

Carbonyl Sulfide (COS). NOAA measurements have reported global mean COS mole fractions of 497 ppt for 2020 and trends of –1.5% yr^{-1} for 2019–2020 (**Table 1-11**) and –1.3% yr^{-1} for the four-year time period 2016–2020. These small negative trends are of opposite sign compared to the small positive trends reported for 2012–2016 in the previous Assessment.

COS is one of the major sources of stratospheric sulfate aerosols, contributing between 40% (Feinberg et al., 2019) and 70% (Brühl et al., 2012) to the stratospheric sulfur budget during volcanically quiescent periods. Satellite observations confirm model-derived values of ~0.45 ppb COS around the tropical tropopause (Brühl et al., 2015). Current estimates of the source and sink terms do not balance the atmospheric observations and imply that there may be a large missing COS source of 235 to 800 Gg S yr^{-1} (e.g., Lennartz et al., 2017; Ma et al., 2021; Whelan et al., 2018). Sulfur isotope measurements have recently been used to better constrain atmospheric COS sources and have identified the main source to be the ocean (Davison et al., 2021), anthropogenic activities (Hattori et al., 2020), or both (Angert et al., 2019). Overall, there is no consensus on the cause of the COS imbalance.

Sulfur Dioxide (SO_2). SO_2 is short-lived with highly variable mole fractions in the troposphere, and it can be entrained into the stratosphere through volcanic eruptions and direct transport. Large uncertainties exist in how efficiently SO_2 is transported from major anthropogenic emission regions into the stratosphere, mostly due to poorly known heterogeneous SO_2 loss processes occurring during uplift. Aircraft campaign measurements in the tropical Pacific and Gulf of Mexico region have reported relatively low SO_2 mixing ratios in the tropical tropopause layer (TTL), suggesting zonally averaged SO_2 at the tropical tropopause of around 5 ppt (Rollins et al., 2017; Rollins et al., 2018). These measurements are in good agreement with some model simulations and MIPAS satellite data (Brühl et al., 2015), indicating that on a global scale the direct transport of SO_2 into the stratosphere is a minor source of stratospheric aerosols. However, zonal asymmetries of SO_2 injections can be expected primarily in outflow regions of the Asian summer monsoon convection, where upper troposphere SO_2 of more than 100 ppt was observed (Lelieveld et al., 2018). The overall impact of such enhanced injections on the stratospheric SO_2 budget remains to be clarified.

Table 1-11. Annual mean mole fractions, mole fraction changes, and global emissions of selected fluorinated compounds with radiative forcing greater than 0.1 mW m^{-2} (see *Introduction*) and other gases of interest (uncertainties are 1-sigma), measured from ground-based sampling networks. The measured mole fractions are expressed in dry air mole fractions as ppt or ppb.

Chemical	Mole Fraction (ppt)		Change (2019–2020)		Emissions (Gg yr^{-1})		Network
	2016	2020	(ppt yr^{-1})	(% yr^{-1})	2016	2020	
Perfluorocarbon (PFCs)							
CF_4 (PFC-14)	**82.8**	**86.4**	**0.9**	**1.1**	**13 ± 1**	**15 ± 1**	AGAGE
C_2F_6 (PFC-116)	**4.57**	**4.94**	**0.09**	**1.9**	**2.1 ± 0.1**	**2.2 ± 0.1**	AGAGE
	3.98	*4.34*	*0.07*	*1.7*	*n.a.*	*n.a.*	UEA/FZJ
C_3F_8 (PFC-218)	**0.63**	**0.7**	**0.02**	**2.7**	**0.5 ± 0.0**	**0.6 ± 0.1**	AGAGE
	0.60	*0.66*	*0.01*	*1.3*	*n.a.*	*n.a.*	UEA/FZJ
c-C_4F_8 (PFC-318)	**1.56**	**1.82**	**0.07**	**3.8**	**2.1 ± 0.1**	**2.5 ± 0.2**	AGAGE
	1.44	*1.69*	*0.06*	*3.6*	*n.a.*	*n.a.*	UEA/FZJ
n-C_6F1_4 (PFC-5-1-14	*0.22*	*0.22*	*0.00*	*0.0*	*n.a.*	*n.a.*	UEA/FZJ
Other Fluorinated Compounds							
SF_6 (sulfur hexafluoride)	**8.9**	**10.3**	**0.3**	**3.5**	**8.8 ± 0.3**	**9.0 ± 0.3**	AGAGE
	8.9	**10.3**	**0.3**	**3.3**	**n.a.**	**n.a.**	NOAA
NF_3 (nitrogen trifluoride)	**1.5**	**2.3**	**0.2**	**11.5**	**2.0 ± 0.1**	**3.0 ± 0.1**	AGAGE
SO_2F_2 (sulfuryl fluoride)	**2.2**	**2.6**	**0.09**	**3.7**	**2.9 ± 0.4**	**2.9 ± 0.4**	AGAGE
$CHF_2OCHFCF_3$ (desflurane)	*0.35*	*0.37*	*–0.01*	*–2.7*	*n.a.*	*n.a.*	AGAGE[1]
Other Compounds							
CH_4 (methane) (ppb, Tg yr^{-1})	**1842**	**1878**	**12**	**0.7**	**551 ± 74**	**576 ± 76**	AGAGE
	1843	**1879**	**13**	**0.7**	**n.a.**	**n.a.**	NOAA
	1840	**1872**	**11**	**0.6**	**n.a.**	**n.a.**	UCI
	1841	**1872**	**10**	**0.5**	**n.a.**	**n.a.**	CSIRO
N_2O (nitrous oxide) (ppb, Tg yr^{-1})	**329.4**	**333.5**	**1.1**	**0.3**	**27 ± 2**	**31 ± 2**	AGAGE
	329.0	**333.0**	**1.1**	**0.3**	**n.a.**	**n.a.**	NOAA
	328.6	**332.6**	**1.1**	**0.3**	**n.a.**	**n.a.**	CSIRO
COS (carbonyl sulfide)	**497**	**472**	**–7**	**–1.5**	**n.a.**	**n.a.**	NOAA
H_2 (hydrogen) (ppb)	**533**	**542**	**3**	**0.6**	**n.a.**	**n.a.**	AGAGE
	536	**546**	**4**	**0.7**	**n.a.**	**n.a.**	CSIRO

General footnote: Mole fractions in this table represent independent estimates based on air sampling collected at Earth's surface from different research groups for the years indicated. Results in bold text are estimates of globally averaged annual mole fractions and are derived on gravimetric calibration scales. As in **Table 1-1**, UEA/FZJ data from whole-air flask samples collected at Cape Grim, Australia (CGO), which are based on volumetric calibration scales, are shown in italics. Absolute changes (ppt yr^{-1}) are calculated by subtracting the 2019 annual mole fractions from the 2020 annual mole fractions; relative changes (% yr^{-1}) are the same difference relative to the 2019 value. Annual mole fractions and global emissions reported by AGAGE were generally calculated using a 12-box inverse model (e.g., Cunnold et al., 1983; Rigby et al., 2013) that were optimized to represent the AGAGE in situ observations made at remote locations, except for H_2. The global H_2 mole fractions from AGAGE were calculated as the average mole fractions between measurements made at Mace Head, Ireland (MHD), and at CGO. Annual mole fractions reported by NOAA are global annual averages from whole-air flask measurements except for SF_6, which used both in situ and flask measurements. Annual mole fractions reported by CSIRO are global annual averages from whole-air flask measurements.

The presented values are updates from AGAGE (agage.mit.edu) with calibrations as specified in Prinn et al. (2018) and related primary publications; NOAA (gml.noaa.gov/dv/site/); CSIRO data archived at WDCGG (gaw.kishou.go.jp); UCI (data.ess-dive.lbl.gov/view/doi:10.3334/CDIAC/ATG.002); and the following publications: Leedham Elvidge et al., 2018; Droste et al., 2020.

Notes:
[1]Values are based on measurements made only at Jungfraujoch, Switzerland.

1.5.3 Other Fluorine-Containing Species (SF_6, Perfluorocarbons, NF_3, SO_2F_2, SF_5CF_3, Hydrofluoroethers)

Most of the other fluorine-containing species exhibit increasing global mole fractions. The total direct radiative forcing due to these substances increased from 12.7 mW m^{-2} in 2016 to 14.3 mW m^{-2} in 2020.

Sulfur Hexafluoride (SF_6). The atmospheric global surface mean mole fraction of SF_6 increased from 8.9 to 10.3 ppt between 2016 and 2020 (**Table 1-1**1 and **Figure 1-19**), which is comparable to the increase of 1.3 ppt during 2012–2016 reported in the last Assessment. While the concentrations from ground-based networks agree very well, FTIR measurements of air above the Jungfraujoch station in the Swiss Alps show a slightly higher increase of 3.86 ± 0.14% yr^{-1} between 2014 and 2020 (compared to 3.56 ± 0.11% yr^{-1} from the near-surface measurements); trends from the ACE-FTS satellite-based measurements are between the two at 3.73% ± 0.15 yr^{-1} (**Table 1-2**). Some of these differences (especially those between the in situ network global trend and the European FTIR record) can probably be attributed to the main sources of SF_6 being located in the NH.

Global emissions of SF_6 were 8.8 Gg yr^{-1} in 2016 and 9.0 Gg yr^{-1} in 2020. Simmonds et al. (2020) estimated Chinese, Korean, and Western European emissions of SF_6, with the former accounting for 36 (29–42) % of total global emissions in 2018, and the latter two being about 10 times smaller in comparison. The radiative forcing of SF_6 is estimated at 5.9 mW m^{-2} in 2020, representing an increase of 0.8 mW m^{-2} since 2016.

Perfluorocarbons (PFCs). PFCs consist exclusively of carbon and fluorine and, in the case of alkane and cycloalkane derivatives, typically have very long lifetimes and high radiative efficiencies. Long-term observation-based trends and mole fractions are available for 10 PFCs: CF_4, C_2F_6, C_3F_8 *c*-C_4F_8, *n*-C_4F_{10}, *n*-C_5F_{12}, *i*-C_6F_{14}, *n*-C_6F_{14}, *n*-C_7F_{16}, and *n*-C_8F_{18}. Improved estimates of PFC radiative efficiencies have recently been published by Hodnebrog et al. (2020), leading to higher GWPs in all cases. Since 2016, atmospheric abundances of all PFCs have continued to increase, albeit at very different rates (**Table 1-11** and **Figure 1-19**).

CF_4 is the most abundant PFC. Its mole fraction increased from 82.8 ppt to 86.4 ppt between 2016 and 2020 (update from Say et al., 2021), which is higher than the 3 ppt increase previously reported between 2012 and 2016. When comparing these observations with FTIR-based remote sensing observations at Jungfraujoch between 2014 and 2020, the increase of 0.93 ± 0.07% yr^{-1} from the latter is slightly lower than the rate of 1.06 ± 0.02% yr^{-1} derived from ground-based measurements (**Table 1-2**). ACE-FTS-based upper-tropospheric growth during that period was 1.07 ± 0.06% yr^{-1}, i.e., very similar to the in situ record-based rate.

Emissions of CF_4 are estimated to have increased on a global basis, from 13 ± 1 Gg yr^{-1} in 2016 to 15 ± 1 Gg yr^{-1} in 2020, confirming that the period of increasing CF_4 emissions first reported by Trudinger et al. (2016), and recently updated by Say et al. (2021), is continuing. Estimates of northwestern European emissions did not change significantly during 2010–2019 and are equivalent to 0.7% of the global total in 2018 (Say et al., 2021). Emissions from East Asia are estimated at 4–5 Gg yr^{-1}, and there is evidence that the global CF_4 emission increase between 2012 and 2019 is likely driven by increased emissions from that region (Kim et al., 2021). Part of these emissions likely originate from Chinese rare earth metal production (Cai et al., 2018). Radiative

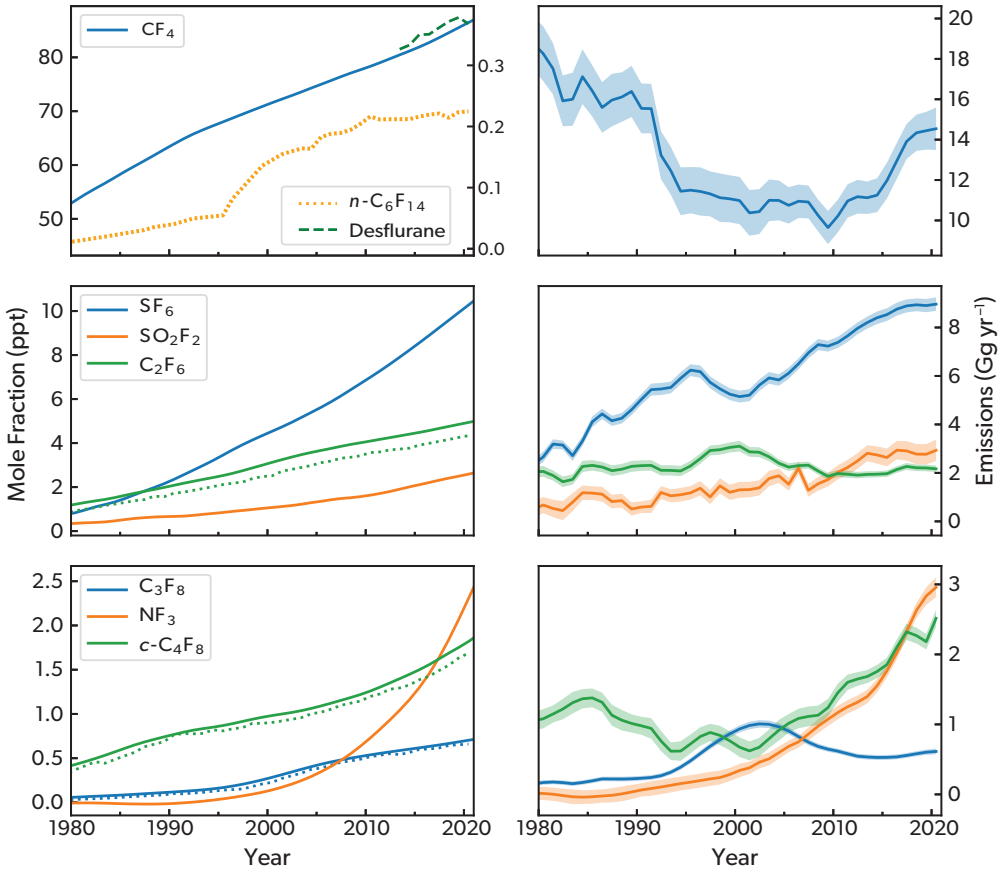

Figure 1-19. Global mean surface mole fraction (*left*) and emissions estimates (*right*) for the same fluorinated greenhouse gases as in **Table 1-11** (excluding CFCs, halons, HCFCs and HFCs). Solid lines show global mole fractions and emissions derived using AGAGE measurement data and a 12-box model, as described in **Figure 1-3**. Shading indicated the 1 standard deviation uncertainty in emissions. Dotted lines show annual mean mole fractions measured at Cape Grim, Australia, by UEA/FZJ. A dashed line in the top-left panel shows the annual mean mole fractions (since 2013) of desflurane measured at Jungfraujoch, Switzerland, by Empa. The left axis in the top-left panel is for CF_4, and the right axis is for *n*-C_6F_{14} and desflurane.

forcing from anthropogenic CF_4 increased from 4.2 mW m^{-2} to 4.6 mW m^{-2} between 2016 and 2020.

Over the 2016 to 2020 period, global mole fractions of hexafluoroethane (C_2F_6) and octafluoropropane (C_3F_8) increased from 4.57 ppt to 4.94 ppt, and from 0.63 to 0.70 ppt, respectively (updates from Say et al., 2021). Both increases are similar to those observed between 2012 and 2016. This translates to global emissions of 2.2 ± 0.1 Gg yr^{-1} for C_2F_6 in 2020, i.e., practically unchanged since 2016 (**Table 1-11**), and of 0.6 ± 0.0 Gg yr^{-1} for C_3F_8, an increase from 0.5 ± 0.0 Gg yr^{-1} in 2016. Northwestern European emissions were estimated to be somewhat higher contributors to the global total, with contributions of 1.6% for C_2F_6 and, notably, 5.1% for C_3F_8 in 2018 (Say et al., 2021). For recent years, a much larger fraction of global C_2F_6 emissions (~1.2 Gg yr^{-1}) has been estimated to originate from East Asia (Kim et al., 2021), again with likely contributions from rare earth metal production (Cai et al., 2018). Radiative forcing from the two gases increased from 1.20 mW m^{-2} to 1.30 mW m^{-2} (C_2F_6) and from 0.17 mW m^{-2} to 0.19 mW m^{-2} (C_3F_8) over the 2016–2020 period.

For octafluorocyclobutane (*c*-C_4F_8), Mühle et al. (2019) presented a comprehensive overview of global observations, including a full reconstruction of its atmospheric history. Based on evidence from firn air, atmospheric abundances were near zero (<0.02 ppt) from the early 1900s to the early 1960s, which is in agreement with the current understanding that there are no natural sources of this PFC. Global *c*-C_4F_8 mole fractions have increased monotonically since. This is qualitatively in line with the previously published records of Saito et al. (2010) and Oram et al. (2012), including a temporary slowdown during the 1990s and early 2000s, although some differences exist. These are probably at least in part related to independent calibration scales. The SH Oram et al. record was recently updated by Droste et al. (2020), and the results from that study agree with those of Mühle et al. (2019) in that both report abundances to be accelerating over approximately the two decades leading up to 2020 (**Figure 1-19**). Mole fractions of *c*-C_4F_8 reached 1.69 ppt in the SH (update from Droste et al., 2020) and 1.82 ppt globally (update from Mühle et al., 2019) in 2020. In terms of emissions, the recent increases in *c*-C_4F_8 mole fractions translate to 2.1 ± 0.1 Gg yr^{-1} in 2016, and 2.5 ± 0.1 Gg yr^{-1} in 2020 (update from Mühle et al., 2019), with the AGAGE emission estimates for 2016 slightly higher than those of Droste et al. (2020), i.e., 1.9 Gg yr^{-1}. Regional inverse methods and observations were used to estimate emissions from eastern Asia (0.73 Gg yr^{-1} in 2017, 31 ± 4% of global emissions, predominantly from eastern China), northern and central India (0.14 ± 0.06 Gg yr^{-1} in mid-2016), northwestern Europe, and Australia (about 1% and 0.7% of the global total, respectively), as well as indications that two Russian facilities might possibly be contributing between 5% and 26% of the global total (Mühle et al., 2019). Atmospheric sources were previously thought to be mainly from the semiconductor industry, but PTFE (polytetrafluoroethylene) and HFP (hexafluoropropylene) production is likely a more dominant contributor (Mühle et al., 2019). In support of this theory, Mühle et al. (2022) reported that *c*-C_4F_8 emissions are highly correlated with the production of HCFC-22 for feedstock uses, as almost all of this is pyrolyzed to produce PTFE and HFP. In 2020, *c*-C_4F_8 contributed 0.58 mW m^{-2} to global radiative forcing.

Updated trends of five less abundant longer-chain PFCs, i.e., *n*-C_4F_{10}, *n*-C_5F_{12}, *n*-C_6F_{14}, *n*-C_7F_{16}, and the newly detected perfluoro-2-methylpentane (*i*-C_6F_{14}), were recently reported by Droste et al. (2020). This included a new calibration of all species except *n*-C_5F_{12} due to the identification and separation of isomers present in the atmosphere. All PFCs continued to increase between 2016 and 2020, though at relatively slow rates, i.e., from 0.194 ppt to 0.202 ppt (*n*-C_4F_{10}), from 0.148 ppt to 0.149 ppt (*n*-C_5F_{12}; increase not significant within uncertainties), from 0.220 ppt to 0.225 ppt (*n*-C_6F_{14}), from 0.110 ppt to 0.116 ppt (*n*-C_7F_{16}), and from 0.065 ppt to 0.072 ppt (*i*-C_6F_{14}). No update is available for abundances of *n*-C_8F_{18} (which in 2011 was 0.09 ppt; Ivy et al., 2012). Global emissions of the five former PFCs were estimated by Droste et al. (2020) to have remained constant between 2013 and 2017 at 0.09 Gg yr^{-1} (*n*-C_4F_{10}), 0.06 Gg yr^{-1} (*n*-C_5F_{12}), 0.14 Gg yr^{-1} (*n*-C_6F_{14}), 0.18 Gg yr^{-1} (*n*-C_7F_{16}), and 0.09 Gg yr^{-1} (*i*-C_6F_{14}). Expressed as radiative forcing, the combined contribution of all six PFCs (at their last-known abundances) amounted to 0.38 mW m^{-2} in 2020.

Nitrogen Trifluoride (NF_3). Between 2016 and 2020, global mole fractions of NF_3 increased from 1.5 ppt to 2.3 ppt, thus maintaining its annual growth rate of >10% (update from Arnold et al., 2013; **Table 1-11** and **Figure 1-19**). NF_3 emissions also continued to increase, from 2.0 ± 0.1 Gg yr^{-1} to 3.0 ± 0.1 Gg yr^{-1}, with radiative forcing concurrently increasing by almost 60%, to 0.48 mW m^{-2} in 2020.

Sulfuryl Fluoride (SO_2F_2). SO_2F_2 is mainly used as a substitute for CH_3Br. Its rate of growth has declined since the previous Assessment, with global mole fractions of 2.2 ppt in 2016 and 2.6 ppt in 2020. This is, however, still equivalent to a very rapid growth of about 18% from 2016 to 2020, compared to the 25% increase between 2012 and 2016 (update from Mühle et al., 2009, and Gressent et al., 2021; **Table 1-11** and **Figure 1-19**). SO_2F_2 global emissions reported in this Assessment are 2.9 ± 0.4 Gg yr^{-1} in both 2016 and 2020. In terms of regional SO_2F_2 emissions, North America was recently identified as the major global emitter (Gressent et al., 2021), and the reported long-term increase in emissions is partly due to the expanded use of SO_2F_2 for post-harvest treatment, although soil fumigation remains another main source. Radiative forcing from this gas increased from 0.45 mW m^{-2} to 0.52 mW m^{-2} between 2016 and 2020.

(Trifluoromethyl) Sulfur Pentafluoride (SF_5CF_3). SH observations confirm that mole fractions of SF_5CF_3 are virtually unchanged, with 0.152 ppt reported for 2016 and 0.155 ppt for 2020 (update from Sturges et al., 2012), corresponding to no renewed emissions of this species. Consequently, SF_5CF_3 radiative forcing remained at 0.09 mW m^{-2}.

Halogenated Ethers (HFEs). Atmospheric abundances, trends, and emissions of desflurane (HFE-236ea2, $CHF_2OCHFCF_3$), isoflurane (HCFE-235da2, $CHF_2OCHClCF_3$), and sevoflurane (HFE-347 isomer, $(CF_3)_2CHOCH_2F$) were first reported by Vollmer et al. (2015c), who determined global mean mole fractions in 2014 of 0.30 ppt, 0.097 ppt, and 0.13 ppt, respectively. An update is available only for desflurane, for which mole fractions derived from observations at the Jungfraujoch station in Switzerland increased slightly, from 0.35 ppt in 2016 to 0.37 ppt in 2020, equivalent to an increase from 0.17 mW m^{-2} to 0.18 mW m^{-2} in 2020. In the absence of updated atmospheric abundances, the best estimates of radiative forcing from isoflurane and sevoflurane remain at 0.04 mW m^{-2} for both anesthetics (using the recent GWP update from Andersen et al., 2021, for sevoflurane). No updated emission estimates are available for any of the three species.

In addition, Vollmer et al. (2019) reported the first observations of the potent greenhouse gas octafluorooxolane (*c*-C_4F_8O). The radiative efficiency of this HFE is relatively high at 0.47 W m^{-2} ppb^{-1}, but atmospheric mole fractions remain low at 0.074 ppt in the NH in 2018. Emissions, which are thought to originate predominantly from usage as a solvent in the semiconductor industry, peaked at 0.15 ± 0.04 Gg yr^{-1} in 2004 and have since declined to <0.015 Gg yr^{-1} in 2018.

1.5.4 Molecular Hydrogen (H_2)

H_2 is an abundant atmospheric trace gas with both natural and anthropogenic emission sources and a relatively complex biogeochemical cycle. It is relevant for this Assessment as a stratospheric source gas for hydrogen oxide radicals (HO_x), and also adds stratospheric water vapor (H_2O) when oxidized. In addition, its atmospheric impacts may well become more important in the near future due to its use in fuel cells and internal combustion engines and related emerging applications. Few publications have estimated the potential decrease in ozone levels from such hydrogen emissions. These studies all have large uncertainties, but they indicate that the resulting impacts on global ozone are likely small (<1%) even in the case of an extreme leakage scenario (Schultz et al., 2003; Tromp et al., 2003; Feck et al., 2008; Vogel et al., 2011).

Observations of Atmospheric Abundance. Atmospheric abundances of H_2 have increased from ~330 ppb during the mid-to-late 1800s to the present levels of 530–550 ppb in the late 20th and early 21st centuries, an increase of about 70% (Patterson et al., 2020; Patterson et al., 2021). The increase in atmospheric H_2 is primarily attributed to increasing anthropogenic emissions and production from the oxidation of methane over the 20th century (Patterson et al., 2021).

Global mole fractions of H_2 in 2020 were approximately 544 ppb (**Table 1-11**). The increase in the atmospheric abundance of H_2 from 2016 to 2020 was around 10 ppb, with about 4 ppb of this occurring between 2019 and 2020 alone. There is a small inter-hemispheric gradient in the atmospheric H_2 mole fractions due to the major sink being biological uptake on land. This results in approximately 3% higher concentrations in the Southern Hemisphere (Ehhalt and Rohrer, 2009).

Emissions, Lifetimes, and Radiative Forcings. The largest source of H_2 in the atmosphere is from the photolysis of formaldehyde, which is formed by the photochemical oxidation (reaction with the hydroxyl radical) of methane and other organic compounds. Recent reviews and updates estimate this source to be in the range of 30–77 Tg yr^{-1} (Ehhalt and Rohrer, 2009; Zgonnik, 2020). The second largest source is from incomplete combustion processes, through fossil fuel combustion and biomass burning. Carbon monoxide (CO) is formed during incomplete combustion, which then reacts with water vapor to produce carbon dioxide (CO_2) and H_2. Estimates for fossil fuel sources range from 11 to 20 Tg yr^{-1}, while estimates for biomass burning range from 10–20 Tg yr^{-1}. Hydrogen is also emitted from geological sources, including volcanoes, with a recent review suggesting this may be as high as 23 Tg yr^{-1} (Zgonnik, 2020). Lastly, H_2 is emitted by nitrogen fixation on land, and in the ocean, with emissions estimated to be 3–6 Tg yr^{-1} for oceans and 0–6 Tg yr^{-1} for land (Ehhalt and Rohrer, 2009; Zgonnik, 2020).

There are two major sinks of atmospheric H_2, with the largest one being uptake by soil microorganisms as a fuel source and the other oxidation of H_2 by the hydroxyl radical (OH). Estimates for the soil uptake sink range from 55–88 Tg yr^{-1}, while the sink for oxidation by OH ranges from 8–19 Tg yr^{-1} (Ehhalt and Rohrer, 2009; Zgonnik, 2020).

The atmospheric lifetime of H_2 is estimated to be about two years (Ehhalt and Rohrer, 2009). Even though H_2 is not a greenhouse gas, Derwent et al. (2020) estimate that it has an indirect GWP_{100} of about 5 ± 1. This is primarily due to its reaction with tropospheric OH, which depletes the oxidizing capacity of the troposphere, resulting in a longer methane lifetime, and through the production of ozone in the troposphere.

REFERENCES

Adcock, K., C.E. Reeves, L.J. Gooch, E.L. Elvidge, P.J. Fraser, R. Langenfelds, C.A.M. Brenninkmeijer, J.-L. Wang, C.-F. Ou-Yang, T. Röckmann, S. O'Doherty, W.T. Sturges, D.E. Oram, M.J. Ashfold, N.M. Hanif, and J.C. Laube, CFC-113a (CF_3CCl_3) in the atmosphere: an update of distributions, trends, emissions and potential source, ***Atmos. Chem. Phys.***, ***18***, 4737–4751, doi:10.5194/acp-18-4737-2018, 2018.

Adcock, K.E., M.J. Ashfold, C.C-K. Chou, L.J. Gooch, N. Mohd Hanif, J.C. Laube, D.E. Oram, C.F. Ou-Yang, M. Panagi, W.T. Sturges, and C.E. Reeves, Investigation of East Asian emissions of CFC-11 using atmospheric observations in Taiwan, ***Environ. Sci. Technol.***, ***54*** (7), 3814–3822, doi:10.1021/acs.est.9b06433, 2020.

Adcock, K.E., P.J. Fraser, B.D. Hall, R.L. Langenfelds, G. Lee, S.A. Montzka, D.E. Oram, T. Röckmann, F. Stroh, W.T. Sturges, B. Vogel, and J.C. Laube, Aircraft-based observations of ozone-depleting substances in the upper troposphere and lower stratosphere in and above the Asian summer monsoon, ***J. Geophys. Res. Atmos.***, ***126*** (1), 1–18, doi:10.1029/2020JD033137, 2021.

An, M., L.M. Western, D. Say, L. Chen, T. Claxton, A.L. Ganesan, R. Hossaini, P.B. Krummel, A.J. Manning, J. Mühle, S. O'Doherty, R.G. Prinn, R.F. Weiss, D. Young, J. Hu, B. Yao, and M. Rigby, Rapid increase in dichloromethane emissions from China inferred through atmospheric observations, ***Nat. Commun.***, ***12*** (1), 7279, doi:10.1038/s41467-021-27592-y, 2021.

Andersen, M.P.S., O.J. Nielsen, and J.D. Sherman, The global warming potentials for anesthetic gas sevoflurane need significant corrections, ***Environ. Sci. Technol.***, ***55*** (15), 10,189–10,191, doi:10.1021/acs.est.1c02573, 2021.

Andrews, S.J., L.J. Carpenter, E.C. Apel, E. Atlas, V. Donets, J.R. Hopkins, R.S. Hornbrook, A.C. Lewis, R.T. Lidster, R. Lueb, J. Minaeian, M. Navarro, S. Punjabi, D. Riemer, and S. Schauffler, A comparison of very short-lived halocarbon (VSLS) and DMS aircraft measurements in the tropical west Pacific from CAST, ATTREX and CONTRAST, ***Atmos. Meas. Tech.***, 9(10), 5213–5225, doi:10.5194/amt-9-5213-2016, 2016.

Angert, A., W. Said-Ahmad, C. Davidson, and A. Amrani, Sulfur isotopes ratio of atmospheric carbonyl sulfide constrains its sources, ***Sci. Rep.***, ***9***, 741, doi:10.1038/s41598-018-37131-3, 2019.

Arnold, T., C.M. Harth, J. Mühle, A.J. Manning, P.K. Salameh, J. Kim, D.J. Ivy, L.P. Steele, V.V. Petrenko, J.P. Severinghaus, D. Baggenstos, and R.F. Weiss, Nitrogen trifluoride global emissions estimated from updated atmospheric measurements, ***Proc. Natl. Acad. Sci.***, ***110*** (6), 2029–2034, doi:10.1073/pnas.1212346110, 2013.

Aschmann, J., and B.M. Sinnhuber, Contribution of very short-lived substances to stratospheric bromine loading: uncertainties and constraints, ***Atmos. Chem. Phys.***, ***13*** (3), 1203–1219, doi:10.5194/acp-13-1203-2013, 2013.

Bahlmann, E., F. Keppler, J. Wittmer, M. Greule, H.F. Schöler, R. Seifert, and C. Zetzsch, Evidence for a major missing source in the global chloromethane budget from stable carbon isotopes, ***Atmos. Chem. Phys.***, ***19*** (3), 1703–1719, doi:10.5194/acp-19-1703-2019, 2019.

Barreto, H. and F. Howland: Introductory Econometrics. Using Monte Carlo Simulation with Microsoft Excel, Cambridge University Press, New York, 2006.

Benish, S.E., R.J. Salawitch, X. Ren, H. He, and R.R. Dickerson, Airborne observations of CFCs over Hebei Province, China in spring 2016, ***J. Geophys. Res. Atmos.***, ***126*** (18), doi:10.1029/2021JD035152, 2021.

Bernath, P., and A.M. Fernando, Trends in stratospheric HCl from the ACE satellite mission, ***J. Quant. Spectrosc. Radiat. Trans., 217***, 126–129, doi:10.1016/j.jqsrt.2018.05.027, 2018.

Bernath, P.F., J. Steffen, J. Crouse, and C.D. Boone, Sixteen-year trends in atmospheric trace gases from orbit, ***J. Quant. Spectrosc. Radiat. Trans.***, ***253***, 107178, doi:10.1016/j.jqsrt.2020.107178, 2020.

Bernath, P.F., J. Crouse, R.C. Hughes, and C.D. Boone, The atmospheric chemistry experiment Fourier transform spectrometer (ACE-FTS) version 4.1 retrievals: Trends and seasonal distributions, ***J. Quant. Spectrosc. Radiat. Trans., 259***, 107409, doi:10.1016/j.jqsrt.2020.107409, 2021.

Bosch, H., C. Camy-Peyret, M.P. Chipperfield, R. Fitzenberger, H. Harder, U. Platt, and K. Pfeilsticker, Upper limits of stratospheric IO and OIO inferred from center-to-limb-darkening-corrected balloon-borne solar occultation visible spectra: Implications for total gaseous iodine and stratospheric ozone, ***J. Geophys. Res.***, ***108*** (D15), doi:10.1029/2002JD003078, 2003.

Boudjellaba, D., J. Dron, G. Revenko, C. Demelas, and J.L. Boudenne, Chlorination by-product concentration levels in seawater and fish of an industrialised bay (Gulf of Fos, France) exposed to multiple chlorinated effluents, ***Sci. Total Environ.***, ***541***, 391–399, doi:10.1016/j.scitotenv.2015.09.046, 2016.

Brinckmann, S., A. Engel, H. Bonisch, B. Quack, and E. Atlas, Short-lived brominated hydrocarbons–observations in the source regions and the tropical tropopause layer, ***Atmos. Chem. Phys.***, ***12*** (3), 1213–1228, doi:10.5194/acp-12-1213-2012, 2012.

Brioude, J., R.W. Portmann, J.S. Daniel, O.R. Cooper, G.J. Frost, K.H. Rosenlof, C. Granier, A.R. Ravishankara, S.A. Montzka, and A. Stohl, Variations in ozone depletion potentials of very short-lived substances with season and emission region, ***Geophys. Res. Lett.***, ***37*** (19), doi:10.1029/2010GL044856, 2010.

Brühl, C., J. Lelieveld, P.J. Crutzen, and H. Tost, The role of carbonyl sulphide as a source of stratospheric sulphate aerosol and its impact on climate, ***Atmos. Chem. Phys.***, ***12*** (3), 1239–1253, doi:10.5194/acp-12-1239-2012, 2012.

Brühl, C., J. Lelieveld, H. Tost, M. Höpfner, and N. Glatthor, Stratospheric sulfur and its implications for radiative forcing simulated by the chemistry climate model EMAC, ***J. Geophys. Res. Atmos., 120*** (5), 2103–2118, doi:10.1002/2014JD022430, 2015.

Burkholder, J.B., S.P. Sander, J. Abbatt, J.R. Barker, C. Cappa, J.D. Crounse, T.S. Dibble, R.E. Huie, C.E. Kolb, M.J. Kurylo, V.L. Orkin, C.J. Percival, D.M. Wilmouth, and P.H. Wine, ***Chemical Kinetics and Photochemical Data for Use in Atmospheric Studies***, Evaluation No. 19, JPL Publication 19-5, Jet Propulsion Laboratory, Pasadena, California, [available at: https://jpldataeval.jpl.nasa.gov/pdf/NASA-JPL%20Evaluation%2019-5.pdf], 2019.

Butler, J.H., S.A. Montzka, A.D. Clarke, J.M. Lobert, and J.W. Elkins, Growth and distribution of halons in the atmosphere, ***J. Geophys. Res. Atmos.***, ***103*** (D1), 1503–1511, doi:10.1029/97JD02853, 1998.

Butler, J., M. Battle, M.L. Bender, S.A. Montzka, A.D. Clarke, E.S. Saltzman, C.M. Sucher, J.P. Severinghaus, and J.W. Elkins, A record of atmospheric halocarbons during the twentieth century from polar firn air, ***Nature***, ***399***, 749–755, doi:10.1038/21586, 1999.

Butler, J.H., D.B. King, J.M. Lobert, S.A. Montzka, S.A. Yvon-Lewis, B.D. Hall, N.J. Warwick, D.J. Mondeel, M. Aydin, and J.W. Elkins, Oceanic distributions and emissions of short- lived halocarbons, Glob. Biogeochem. Cycles, ***21*** (1), doi:10.1029/2006GB002732, 2007.

Butler, J.H., S.A. Yvon-Lewis, J.M. Lobert, D.B. King, S.A. Montzka, J.L. Bullister, V. Koropalov, J.W. Elkins, B.W. Hall., L. Hu, and Y. Liu, A comprehensive estimate for loss of atmospheric carbon-tetrachloride (CCl_4) to the ocean, ***Atmos. Chem. Phys.***, ***16*** (17), 10,899–10,910, doi:10.5194/acp-16-10899-2016, 2016.

Butler, R., P.I. Palmer, L. Feng, S.J. Andrews, E.L. Atlas, L.J. Carpenter, V. Donets, N.R.P. Harris, S.A. Montzka, L.L. Pan, R.J. Salawitch, and S.M. Schauffler, Quantifying the vertical transport of $CHBr_3$ and CH_2Br_2 over the western Pacific, ***Atmos. Chem. Phys.***, ***18*** (17), 13,135–13,153, doi:10.5194/acp-18-13135-2018, 2018.

Butler, J.H., and S.A. Montzka, The NOAA Annual Greenhouse Gas Index (AGGI), ***NOAA Earth System Research Laboratory***, Boulder, Colorado, [available at: https://gml.noaa.gov/aggi/aggi.html], 2021.

Butz, A., H. Bosch, C. Camy-Peyret, M.P. Chipperfield, M. Dorf, S. Kreycy, L. Kritten, C. Prados-Roman, J. Schwarzle, and K. Pfeilsticker, Constraints on inorganic gaseous iodine in the tropical upper troposphere and stratosphere inferred from balloon-borne solar occultation observations, ***Atmos. Chem. Phys.***, ***9*** (18), 7229–7242, doi:10.5194/acp-9-7229-2009, 2009.

Cai, B., H. Liu, F. Kou, Y. Yang, B. Yao, X. Chen, D.S. Wong, L. Zhang, J. Li, G. Kuang, L. Chen, J. Zheng, D. Guan, and Y. Shan, Estimating perfluorocarbon emission factors for industrial rare earth metal electrolysis, ***Resour. Conserv. Recycl.***, ***136***, 315–323, doi:10.1016/j.resconrec.2018.04.018, 2018.

Carpenter, L.J., and P.S. Liss, On temperate sources of bromoform and other reactive organic bromine gases, ***J. Geophys. Res. Atmos.***, ***105*** (D16), 20,539–20,547, doi:10.1029/2000JD900242, 2000.

Carpenter, L.J., S.M. MacDonald, M.D. Shaw, R. Kumar, R.W. Saunders, R. Parthipan, J. Wilson, and J.M. C. Plane, Atmospheric iodine levels influenced by sea surface emissions of inorganic iodine, ***Nat. Geosci., 6***, 108–111, doi:10.1038/ngeo1687, 2013.

Carpenter, L.J., and S. Reimann (Lead authors), J.B. Burkholder, C. Clerbaux, B.D. Hall, R. Hossaini, J.C. Laube, and S.A. Yvon-Lewis, Ozone-Depleting Substances (ODSs) and Other Gases of Interest to the Montreal Protocol, Chapter 1 in ***Scientific Assessment of Ozone Depletion: 2014***, Global Ozone Research and Monitoring Project–Report No. 55, World Meteorological Organization, Geneva, Switzerland, 2014.

Carpenter, L.J., and J.S. Daniel (Lead authors), E.L. Fleming, T. Hanaoka, J. Hu, A.R. Ravishankara, M.N. Ross, S. Tilmes, T.J. Wallington, and D.J. Wuebbles, Scenarios and Information for Policymakers, Chapter 6 in ***Scientific Assessment of Ozone Depletion: 2018***, Global Ozone Research and Monitoring Project–Report No. 58, World Meteorological Organization, Geneva, Switzerland, 2018.

Carpenter, L.J., R.J. Chance, T. Sherwen, T.J. Adams, S.M. Ball, M.J. Evans, H. Hepach, L.D.J. Hollis, C. Hughes, T.D. Jickells, A. Mahajan, D.P. Stevens, L. Tinel, and M.R. Wadley, Marine iodine emissions in a changing world, ***Proc. R. Soc. A***, ***477*** (2247), doi:10.1098/rspa.2020.0824, 2021.

Chen, X., X. Huang, and L.L. Strow, Near-global CFC-11 trends as observed by atmospheric infrared sounder from 2003 to 2018, ***J. Geophys. Res. Atmos.***, ***125*** (22), e2020JD033051, doi:10.1029/2020JD033051, 2020.

Chipperfield, M.P., M.I. Hegglin, S.A. Montzka, P.A. Newman, S. Park, S. Reimann, M. Rigby, A. Stohl, G.J. M. Velders, H. Walter-Terrinoni, and B. Yao, ***Report on the Unexpected Emissions of CFC-11***, Ozone Research and Monitoring, WMO No. 1268, World Meteorological Organization, Geneva, Switzerland, 2021.

Choi, H., M.-K. Park, P.J. Fraser, H. Park, S. Geum, J. Mühle, J. Kim, I. Porter, P.K. Salameh, C.M. Harth, B.L. Dunse, P.B. Krummel, R.F. Weiss, S. O'Doherty, D. Young, and S. Park, Top-down and bottom-up estimates of anthropogenic methyl bromide emissions from eastern China, ***Atmos. Chem. Phys.***, ***22***, 5157–5173, doi:10.5194/acp-22-5157-2022, 2022.

Claxton, T., R. Hossaini, O. Wild, M.P. Chipperfield, and C. Wilson, On the regional and seasonal ozone depletion potential of chlorinated very short lived substances, ***Geophys. Res. Lett.***, ***46*** (10), 5489–5498, doi:10.1029/2018GL081455, 2019.

Claxton, T., R. Hossaini, C. Wilson, S.A. Montzka, M.P. Chipperfield, O. Wild, E.M. Bednarz, L.J. Carpenter, S.J. Andrews, S.C. Hackenberg, J. Mühle, D. Oram, S. Park, M. Park, E. Atlas, M. Navarro, S. Schauffler, D. Sherry, M. Vollmer, T. Schuck, A. Engel, P.B. Krummel, M. Maione, J. Arduini, T. Saito, Y. Yokouchi, S. O'Doherty, D. Young, and C. Lunder, A synthesis inversion to constrain global emissions of two very short lived chlorocarbons: dichloromethane, and perchloroethylene, ***J. Geophys. Res. Atmos.***, ***125*** (12), e2019JD031818, doi:10.1029/2019JD031818, 2020.

Cuevas, C.A., N. Maffezzoli, J.P. Corella, A. Spolaor, P. Vallelonga, H.A. Kjær, M. Simonsen, M. Winstrup, B. Vinter, C. Horvat, R.P. Fernandez, D. Kinnison, J.-F. Lamarque, C. Barbante, and A. Saiz-Lopez, Rapid increase in atmospheric iodine levels in the North Atlantic since the mid-20th century, ***Nat. Commun.***, ***9*** (1452), doi:10.1038/s41467-018-03756-1, 2018.

Cuevas C.A., Fernandez R.P., Kinnison D.E., Li Q., Lamarque J.F., Trabelsi T., Francisco J.S., Solomon S., Saiz-Lopez A. The influence of iodine on the Antarctic stratospheric ozone hole, ***Proc. Natl. Acad. Sci.***, 119(7), doi: 10.1073/pnas.2110864119, 2022.

Cunnold, D.M., R.G. Prinn, R.A. Rasmussen, P.G. Simmonds, F.N. Alyea, C.A. Cardelino, A.J. Crawford, P.J. Fraser, and R.D. Rosen, The atmospheric lifetime experiment: 3. lifetime methodology and application to 3 years of $CFCl_3$ data, ***J. Geophys. Res. Oceans***, ***88*** (C13), 8379–8400, doi:10.1029/JC088iC13p08379, 1983.

Cunnold, D.M., P.J. Fraser, R.F. Weiss, R.G. Prinn, P.G. Simmonds, B.R. Miller, F.N. Alyea, and A.J. Crawford, Global trends and annual releases of CCl_3F and CCl_2F_2 estimated from ALE/GAGE and other measurements from July 1978 to June 1991, ***J. Geophys. Res. Atmos.***, ***99*** (D1), 1107–1126, doi:10.1029/93JD02715, 1994.

Daniel, J.S., S. Solomon, and D.L. Albritton, On the evaluation of halocarbon radiative forcing and global warming potentials, ***J. Geophys. Res. Atmos.***, ***100*** (D1), 1271–1285, doi:10.1029/94JD02516, 1995.

Delahaye, T., R. Armante, N.A. Scott, N. Jacquinet-Husson, A. Chédin, L. Crépeau, C. Crevoisier, V. Douet, A. Perrin, A. Barbe, V. Boudon, A. Campargue, L.H. Coudert, V. Ebert, J.M. Flaud, R.R. Gamache, D. Jacquemart, A. Jolly, F. Kwabia Tchana, A. Kyuberis, G. Li, O.M. Lyulin, L. Manceron, S. Mikhailenko, N. Moazzen-Ahmadi, H.S.P. Müller, O.V. Naumenko, A. Nikitin, V.I. Perevalov, C. Richard, E. Starikova, S.A. Tashkun, V.G. Tyuterev, J. Vander Auwera, B. Vispoel, A. Yachmenev, and S. Yurchenko, The 2020 edition of the GEISA spectroscopic database, ***J. Mol. Spectrosc.***, ***380***, 111510, doi:10.1016/J.JMS.2021.111510, 2021.

Derwent, R.G., D.S. Stevenson, S.R. Utembe, M.E. Jenkin, A.H. Khan, and D.E. Shallcross, Global modelling studies of hydrogen and its isotopomers using STOCHEM-CRI: Likely radiative forcing consequences of a future hydrogen economy, ***Int. J. Hydrog. Energy***, ***45***, 9211–9221, doi:10.1016/j.ijhydene.2020.01.125, 2020.

Deventer, M.J., Y. Jiao, S.H. Knox, F. Anderson, M.C. Ferner, J.A. Lewis, and R.C. Rhew, Ecosystem-scale measurements of methyl halide fluxes from a brackish tidal marsh invaded with perennial pepperweed (Lepidium latifolium), ***J. Geophys. Res. Biogeosci.***, ***123*** (7), 2104–2120, doi:10.1029/2018JG004536, 2018.

Ding, X., Q. Ling, Y. Huo, Y. Liang, H. Wang, J. Zhang, S. Wang, T. Wang, X. Ye, and J. Chen, Gaseous and particulate chlorine emissions from typical iron and steel industry in China, ***J. Geophys. Res. Atmos.***, ***125*** (15), doi:10.1029/2020JD032729, 2020.

Dorf, M., A. Butz, C. Camy-Peyret, M.P. Chipperfield, L. Kritten, and K. Pfeilsticker, Bromine in the tropical troposphere and stratosphere as derived from balloon-borne BrO observations, ***Atmos. Chem. Phys.***, ***8*** (23), 7265–7271, doi:10.5194/acp-8-7265-2008, 2008.

Dorf, M., J.H. Butler, A. Butz, C. Camy-Peyret, M.P. Chipperfield, L. Kritten, S.A. Montzka, B. Simmes, F. Weidner, and K. Pfeilsticker, Long-term observations of stratospheric bromine reveal slow down in growth, ***Geophys. Res. Lett.***, ***33*** (24), doi:10.1029/2006GL027714, 2006.

Droste, E.S., K.E. Adcock, M.J. Ashfold, C. Chou, Z. Fleming, P.J. Fraser, L.J. Gooch, A.J. Hind, R.L. Langenfelds, E.L Elvidge, N.M. Hanif, S. O'Doherty, D.E. Oram, C. Ou-Yang, M. Panagi, C.E. Reeves, W.T. Sturges, and J.C. Laube, Trends and emissions of six perfluorocarbons in the Northern Hemisphere and Southern Hemisphere, ***Atmos. Chem. Phys., 20*** (8), 4787–4807, doi:10.5194/acp-20-4787-2020, 2020.

Ehhalt, D.H., and F. Rohrer, The tropospheric cycle of H_2: a critical review, ***Tellus B: Chem. Phys. Meteorol.***, ***61*** (3), 500–535, doi:10.1111/j.1600-0889.2009.00416.x, 2009.

Engel, A., H. Bönisch, J. Ostermöller, M.P. Chipperfield, S. Dhomse, and P. Jöckel, A refined method for calculating equivalent effective stratospheric chlorine, ***Atmos. Chem. Phys.***, ***18*** (2), 601–609, doi:10.5194/acp-18-601-2018, 2018.

Engel, A., and M. Rigby (Lead Authors), J.B. Burkholder, R.P. Fernandez, L. Froidevaux, B.D. Hall, R. Hossaini, T. Saito, M.K. Vollmer, and B. Yao, Update on Ozone-Depleting Substances (ODSs) and Other Gases of Interest to the Montreal Protocol, Chapter 1 in ***Scientific Assessment of Ozone Depletion: 2018***, Global Ozone Research and Monitoring Project–Report No. 58, World Meteorological Organization, Geneva, Switzerland, 2018.

Fang, X., S. Park, T. Saito, R. Tunnicliffe, A.L. Ganesan, M. Rigby, S. Li, Y. Yokouchi, P.J. Fraser, C.M. Harth, P.B. Krummel, J. Mühle, S. O'Doherty, P.K. Salameh, P.G. Simmonds, R.F. Weiss, D. Young, M.F. Lunt, A.J. Manning, A. Gressent, and R.G. Prinn, Rapid increase in ozone-depleting chloroform emissions from China, ***Nat. Geosci.***, ***12***, 89–93, doi:10.1038/s41561-018-0278-2, 2019a.

Fang, X., J.A. Pyle, M.P. Chipperfield, J.S. Daniel, S. Park, and R.G. Prinn, Challenges for the recovery of the ozone layer, ***Nat. Geosci.***, ***12***, 592–596, doi:10.1038/s41561-019-0422-7, 2019b.

Fang, X., B. Yao, M.K. Vollmer, S. Reimann, L. Liu, L. Chen, R.G. Prinn, and J. Hu, Changes in HCFC emissions in China during 2011–2017, ***Geophys. Res, Lett.***, ***46*** (16), 10,034–10,042, doi:10.1029/2019GL083169, 2019c.

Feck, T., J.-U. Grooß, and M. Riese, Sensitivity of Arctic ozone loss to stratospheric H_2O, ***Geophys. Res. Lett.***, ***35*** (1), doi:10.1029/2007GL031334, 2008.

Feinberg, A., T. Sukhodolov, B.-P. Luo, E. Rozanov, L.H.E. Winkel, T. Peter, and A. Stenke, Improved tropospheric and stratospheric sulfur cycle in the aerosol–chemistry–climate model SOCOL-AERv2, ***Geosci. Model Dev.***, ***12***, 3863–3887, doi:10.5194/gmd-12-3863-2019, 2019.

Feng, Y., P. Bie, Z. Wang, L. Wang, and J. Zhang, Bottom-up anthropogenic dichloromethane emission estimates from China for the period 2005–2016 and predictions of future emissions, ***Atmos. Environ.***, ***186***, 241–247, doi:10.106/j.atmosenv.2018.05.039, 2018.

Fernandez, R.P., R.J. Salawitch, D.E. Kinnison, J.F. Lamarque, and A. Saiz-Lopez, Bromine partitioning in the tropical tropopause layer: Implications for stratospheric injection, ***Atmos. Chem. Phys.***, ***14*** (24), 13,391–13,410, doi:10.5194/acp-14-13391-2014, 2014.

Fernandez, R.P., J.A. Barrera, A.I. López-Noreña, D.E. Kinnison, J. Nicely, R.J. Salawitch, P.A. Wales, B.M. Toselli, S. Tilmes, J.-F. Lamarque, C.A. Cuevas, and A. Saiz-Lopez, Intercomparison between surrogate, explicit and full treatments of VSL bromine chemistry within the CAM-Chem chemistry-climate model, ***Geophys. Res. Lett.***, ***48*** (4), doi:10.1029/2020GL091125, 2021.

Fiehn, A., B. Quack, H. Hepach, S. Fuhlbrugge, S. Tegtmeier, M. Toohey, E. Atlas, and K. Krüger, Delivery of halogenated very short-lived substances from the west Indian Ocean to the stratosphere during the Asian summer monsoon, ***Atmos. Chem. Phys.***, ***17*** (11), 6723–6741, doi:10.5194/acp-17-6723-2017, 2017.

Fiehn A., B. Quack, I. Stemmler, F. Ziska, and K. Krüger, Importance of seasonally resolved oceanic emissions for bromoform delivery from the tropical Indian Ocean and west Pacific to the stratosphere, ***Atmos. Chem. Phys., 18***, 11,973–11,990, doi:10.5194/acp-18-11973-2018, 2018.

Filus, M.T., E.L. Atlas, M.A. Navarro, E. Meneguz, D. Thomson, M.J. Ashfold, L.J. Carpenter, S.J. Andrews, and N.R.P. Harris, Transport of short-lived halocarbons to the stratosphere over the Pacific Ocean, ***Atmos. Chem. Phys***., ***20*** (2), 1163–1181, doi:10.5194/acp-20-1163-2020, 2020.

Forster, P., T. Storelvmo, K. Armour, W. Collins, J.-L. Dufresne, D. Frame, D.J. Lunt, T. Mauritsen, M.D. Palmer, M. Watanabe, M. Wild, and H. Zhang, The Earth's Energy Budget, Climate Feedbacks, and Climate Sensitivity, Chapter 7, In: ***Climate Change 2021: The Physical Science Basis***, Contribution of Working Group I to the Sixth Assessment Report of the Intergovernmental Panel on Climate Change, [Masson-Delmotte, V., P. Zhai, A. Pirani, S.L. Connors, C. Péan, S. Berger, N. Caud, Y. Chen, L. Goldfarb, M.I. Gomis, M. Huang, K. Leitzell, E. Lonnoy, J.B.R. Matthews, T.K. Maycock, T. Waterfield, O. Yelekçi, R. Yu, and B. Zhou (eds.)], Cambridge University Press, Cambridge, United Kingdom and New York, NY, USA, 923–1054 pp., doi:10.1017/9781009157896.009, 2021.

Fraser, P.J., B.L. Dunse, P.B. Krummel, L.P. Steele, N. Derek, B. Mitrevski, C.E. Allison, Z. Loh, A.J. Manning, A. Redington, and M. Rigby, Australian chlorofluorocarbon (CFC) emissions: 1960–2017, ***Enviro. Chem.***, 17 (8), 525–544, doi:10.1071/EN19322, 2020.

Friedrich, M., S. Smeekes, and J.-P. Urbain, Autoregressive wild bootstrap inference for nonparametric trends, ***J. Econom.***, ***214*** (1), 81–109, doi:10.1016/j.jeconom.2019.05.006, 2020a.

Friedrich, M., E. Beutner, H. Reuvers, S. Smeekes, J.-P. Urbain, W. Bader, B. Franco, B. Lejeune, and E. Mahieu, A statistical analysis of time trends in atmospheric ethane, ***Clim. Change***, ***162***, 105–125, doi:10.1007/s10584-020-02806-2, 2020b.

Froidevaux, L., J. Anderson, H.-J. Wang, R.A. Fuller, M.J. Schwartz, M.L. Santee, N.J. Livesey, H.C. Pumphrey, P.F. Bernath, J.M. Russell III, and M.P. McCormick, Global ozone chemistry and related trace gas data records for the Stratosphere (GOZCARDS): methodology and sample results with a focus on HCl, H_2O, and O_3, ***Atmos. Chem. Phys***., ***15*** (18), 10,471–10,507, doi:10.5194/acp-15-10471-2015, 2015.

Froidevaux, L., D.E. Kinnison, R. Wang, J. Anderson, and R.A. Fuller, Evaluation of CESM1 (WACCM) free-running and specified dynamics atmospheric composition simulations using global multispecies satellite data records, ***Atmos. Chem. Phys.***, ***19*** (7), 4783–4821, doi:10.5194/acp-19-4783-2019, 2019.

Ganesan, A.L., M. Rigby, A. Zammit-Mangion, A.J. Manning, R.G. Prinn, P.J. Fraser, C.M. Harth, K.-R. Kim, P.B. Krummel, S. Li, J. Mühle, S.J. O'Doherty, S. Park, P.K. Salameh, L.P. Steele, and R.F. Weiss, Characterization of uncertainties in atmospheric trace gas inversions using hierarchical Bayesian methods, ***Atmos. Chem. Phys.***, ***14***, 3855–3864, doi:10.5194/acp-14-3855-2014, 2014.

Gardiner, T., A. Forbes, M. de Mazière, C. Vigouroux, E. Mahieu, P. Demoulin, V. Velazco, J. Notholt, T. Blumenstock, F. Hase, I. Kramer, R. Sussmann, W. Stremme, J. Mellqvist, A. Strandberg, K. Ellingsen, and M. Gauss, Trend analysis of greenhouse gases over Europe measured by a network of ground-based remote FTIR instruments, ***Atmos. Chem. Phys***., ***8*** (22), 6719–6727, doi:10.5194/acp-8-6719-2008, 2008.

Gordon I.E., L.S. Rothman, R.J. Hargreaves, R. Hashemi, E.V. Karlovets, F.M. Skinner, E.K. Conway, C. Hill, R.V. Kochanov, Y. Tan, P. Wcisło, A.A. Finenko, K. Nelson, P.F. Bernath, M. Birk, V. Boudon, A. Campargue, K.V. Chance, A. Coustenis, B.J. Drouin. J.–M. Flaud, R.R. Gamache, J.T. Hodges, D. Jacquemart, E.J. Mlawer, A.V. Nikitin, V.I. Perevalov, M. Rotger, J. Tennyson, G.C. Toon, H. Tran, V.G. Tyuterev, E.M. Adkins, A. Baker, A. Barbe, E. Canè, A.G. Császár, A. Dudaryonok, O. Egorov, A.J. Fleisher, H. Fleurbaey, A. Foltynowicz, T. Furtenbacher, J.J. Harrison, J.–M. Hartmann, V.–M. Horneman, X. Huang, T. Karman, J. Karns, S. Kassi, I. Kleiner, V. Kofman, F. Kwabia–Tchana, N.N. Lavrentieva, T.J. Lee, D.A. Long, A.A. Lukashevskaya, O.M. Lyulin, V.Yu. Makhnev, W. Matt, S.T. Massie, M. Melosso, S.N. Mikhailenko, D. Mondelain, H.S.P. Müller, O.V. Naumenko, A. Perrin, O.L. Polyansky, E. Raddaoui, P.L. Raston, Z.D. Reed, M. Rey, C. Richard, R. Tóbiás, I. Sadiek, D.W. Schwenke, E. Starikova, K. Sung, F. Tamassia, S.A. Tashkun, J. Vander Auwera, I.A. Vasilenko, A.A. Vigasin, G.L. Villanueva, B. Vispoel, G. Wagner, A. Yachmenev, and S.N. Yurchenko, The HITRAN2020 molecular spectroscopic database, ***J. Quant. Spectrosc. Radiat. Transf.***, ***277***, 107949, doi:10.1016/j.jqsrt.2021.107949, 2022.

Graziosi, F., J. Arduini, F. Furlani, U. Giostra, L.J.M. Kuijpers, S.A. Montzka, B.R. Miller, S.J. O'Doherty, A. Stohl, P. Bonasoni, and M. Maione, European emissions of HCFC-22 based on eleven years of high frequency atmospheric measurements and a Bayesian inversion method, ***Atmos. Environ.***, ***112***, 196–207, doi:10.1016/j.atmosenv.2015.04.042, 2015.

Gressent, A., M. Rigby, A.L. Ganesan, R.G. Prinn, A.J. Manning, J. Mühle, P.K. Salameh, P.B. Krummel, P.J. Fraser, L.P. Steele, B. Mitrevski, R.F. Weiss, C.M. Harth, R.H. Wang, S. O'Doherty, D. Young, S. Park, S. Li, B. Yao, S. Reimann, M.K. Vollmer, M. Maione, J. Arduini, and C.R. Lunder, Growing atmospheric emissions of sulfuryl fluoride, ***J. Geophys. Res. Atmos.***, ***126*** (9), e2020JD034327, doi:10.1029/2020JD034327, 2021.

Hall, B.D., A. Engel, J. Muhle, J.W. Elkins, F. Artuso, E. Atlas, M. Aydin, D. Blake, E.G. Brunke, S. Chiavarini, P.J. Fraser, J. Happell, P.B. Krummel, I. Levin, M. Loewenstein, M. Maione, S.A. Montzka, S. O'Doherty, S. Reimann, G. Rhoderick, E.S. Saltzman, H.E. Scheel, L.P. Steele, M.K. Vollmer, R.F. Weiss, D. Worthy, and Y. Yokouchi, Results from the International Halocarbons in Air Comparison Experiment (IHALACE), ***Atmos. Meas. Tech.***, ***7*** (2), 469–490, doi:10.5194/amt-7-469-2014, 2014.

Han, J.R., L. Li, S.S. Su, J. Wu, X.K. Fang, S.L. Jia, J.B. Zhang, and J.X. Hu, Estimated HCFC-142b emissions in China: 2000-2050, ***Chinese Sci. Bull.***, ***59*** (24), 3046–3053, doi:10.1007/s11434-014- 0337-z, 2014.

Harris, N.R.P., and D. Wuebbles (Lead Authors), J.S. Daniel, J. Hu, L.J. M. Kuijpers, K.S. Law, M.J. Prather, and R. Schofield, Scenarios and information for policymakers, Chapter 5 in ***Scientific Assessment of Ozone Depletion: 2014***, Global Ozone Research and Monitoring Project–Report No. 55, World Meteorological Organization, Geneva, Switzerland, 2014.

Harrison, J.J., M.P. Chipperfield, R. Hossaini, C.D. Boone, S. Dhomse, W. Feng, and P.F. Bernath, Phosgene in the upper troposphere and lower stratosphere: a marker for product gas injection due to chlorine-containing very short lived substances, ***Geophys. Res. Lett.***, ***46*** (2), 1032–1039, doi:10.1029/2018GL079784, 2019.

Hattori, S., K. Kamezaki, and N. Yoshida, Constraining the atmospheric OCS budget from sulfur isotopes, ***Proc. Natl. Acad. Sci.***, ***117*** (34), 20,447–20,452; doi:10.1073/pnas.2007260117, 2020.

Hendrick, F., M. Van Roozendael, M.P. Chipperfield, M. Dorf, F. Goutail, X. Yang, C. Fayt, C. Hermans, K. Pfeilsticker, J.P. Pommereau, J.A. Pyle, N. Theys, and M. De Mazière, Retrieval of stratospheric and tropospheric BrO profiles and columns using ground-based zenith-sky DOAS observations at Harestua, 60° N, ***Atmos. Chem. Phys.***, ***7*** (18), 4869–4885, doi:10.5194/acp-7-4869-2007, 2007.

Hendrick, F., P.V. Johnston, M. De Mazière, C. Fayt, C. Hermans, K. Kreher, N. Theys, A. Thomas, and M. Van Roozendael, One-decade trend analysis of stratospheric BrO over Harestua (60°N) and Lauder (45°S) reveals a decline, ***Geophys. Res. Lett.***, ***35*** (14), doi:10.1029/2008GL034154, 2008.

Hodnebrog, Ø., B. Aamaas, J.S. Fuglestvedt, G. Marston, G. Myhre, C.J. Nielsen, M. Sandstad, K.P. Shine, and T.J. Wallington, Updated global warming potentials and radiative efficiencies of halocarbons and other weak atmospheric absorbers, ***Rev. Geophys.***, ***58*** (3), e2019RG000691, doi:10.1029/2019RG000691, 2020.

Höpfner, M., O. Kirner, G. Wetzel, B.-M. Sinnhuber, F. Haenel, S. Johansson, J. Orphal, R. Ruhnke, G. Stiller, and T. von Clarmann, The Michelson Interferometer for Passive Atmospheric Sounding global climatology of $BrONO_2$ 2002–2012: a test for stratospheric bromine chemistry, ***Atmos. Chem. Phys.***, ***21***, 18,433–18,464, doi:10.5194/acp-21-18433-2021, 2021.

Hossaini, R., M.P. Chipperfield, B.M. Monge-Sanz, N.A.D. Richards, E. Atlas, and D.R. Blake, Bromoform and dibromomethane in the tropics: A 3-D model study of chemistry and transport, ***Atmos. Chem. Phys.***, 10 (2), 719–735, doi:10.5194/acp-10-719-2010, 2010.

Hossaini, R., M.P. Chipperfield, A. Saiz-Lopez, J.J. Harrison, R. von Glasow, R. Sommariva, E. Atlas, M. Navarro, S.A. Montzka, W. Feng, S. Dhomse, C. Harth, J. Mühle, C. Lunder, S. O'Doherty, D. Young, S. Reimann, M.K. Vollmer, P.B. Krummel, and P.F. Bernath, Growth in stratospheric chlorine from short-lived chemicals not controlled by the Montreal Protocol, ***Geophys. Res. Lett.***, ***42*** (11), 4573–4580, doi:10.1002/2015gl063783, 2015.

Hossaini, R., M.P. Chipperfield, A. Saiz-Lopez, R. Fernandez, S. Monks, W. Feng, P. Brauer, and R. von Glasow, A global model of tropospheric chlorine chemistry: Organic versus inorganic sources and impact on methane oxidation, ***J. Geophys. Res. Atmos.***, ***121*** (23), 14,271–14,297, doi:10.1002/2016JD025756, 2016.

Hossaini, R., E. Atlas, S.S. Dhomse, M.P. Chippefield, P.F. Bernath, A.M. Fernando, J. Mühle, A.A. Leeson, S.A. Montzka, W. Feng, J.J. Harrison, P. Krummel, M.K. Vollmer, S. Reimann, S. O'Doherty, D. Young, M. Maione, J. Arduini, and C.R. Lunder, Recent trends in stratospheric chlorine from very short-lived substances,

J. Geophys. Res. Atmos., *124* (4), 2318–2335, doi:10.1029/2018JD029400, 2019.

HTOC (Halons Technical Options Committee), ***2018 Assessment Report***, United Nations Environment Programme, Ozone Secretariat, Nairobi, Kenya, [available at: https://ozone.unep.org/sites/default/files/Assessment_Panel/Assessment_Panels/TEAP/Reports/HTOC/HTOC_assessment_2018.pdf], 2018.

Hu, L., S.A. Montzka, J.B. Miller, A.E. Andrews, S.J. Lehman, B.R. Miller, K. Thoning, C. Sweeney, H. Chen, D.S. Godwin, K. Masarie, L. Bruhwiler, M.L. Fischer, S.C. Biraud, M.S. Torn, M. Mountain, T. Nehrkorn, J. Eluszkiewicz, S. Miller, R.R. Draxler, A.F. Stein, B.D. Hall, J.W. Elkins, and P.P. Tans, U.S. emissions of HFC-134a derived for 2008–2012 from an extensive flask-air sampling network, *J. Geophys. Res. Atmos.*, *120*, 801–825, doi:10.1002/2014JD022617, 2015.

Hu, L., S.A. Montzka, B.R. Miller, A.E. Andrews, J.B. Miller, S.J. Lehman, B.R. Miller, C. Sweeney, S.M. Miller, K. Thoning, C. Siso, E.L. Atlas, D.R. Blake, J. de Gouw, J.B. Gilman, G. Dutton, J.W. Elkins, B. Hall, H. Chen, M.L. Fischer, M.E. Mountain, T. Nehrkorn, S.C. Biraud, F.L. Moore, and P.P. Tans, Continued emissions of carbon tetrachloride from the United States nearly two decades after its phaseout for dispersive uses, *Proc. Natl. Acad. Sci.*, *113* (11), 2880–2885, doi:10.1073/pnas.1522284113, 2016.

Hu, L., S.A. Montzka, S.J. Lehman, D.S. Godwin, B.R. Miller, A.E. Andrews, K. Thoning, J.B. Miller, C. Sweeney, C. Siso, J.W. Elkins, B.D. Hall, D.J. Mondeel, D. Nance, T. Nehrkorn, M. Mountain, M.L. Fischer, S.C. Biraud, H. Chen, and P.P. Tans, Considerable contribution of the Montreal Protocol to declining greenhouse gas emissions from the United States, *Geophys. Res. Lett.*, *44*, 8075–8083, doi:10.1002/2017GL074388, 2017.

Hu, L., S.A. Montzka, F. Moore, E. Hinsta, G. Dutton, M.C. Siso, K. Thoning, R.W. Portmann, K. McKain, C. Sweeney, I. Vimount, D. Nance, B. Hall, and S. Wofsy, Continental-scale contributions to the global CFC-11 emission increase between 2012 and 2017, *Atmos. Chem. Phys.*, *22* (4), 2891–2907, doi:10.5194/acp-2021-793, 2022.

Huang, X., Y. Zhang, L. Xue, J. Tang, W. Song, D.R. Blake, and X. Wang, Constraining emission estimates of CFC-11 in Eastern China based on local observations at Surface Stations and Mount Tai, *Environ. Sci. Technol. Lett.*, *8*, 940−946, doi:10.1021/acs.estlett.1c00539, 2021.

Inamdar, S., Tinel, L., Chance, R., Carpenter, L. J., Sabu, P., Chacko, R., Tripathy, S. C., Kerkar, A. U., Sinha, A. K., Bhaskar, P. V., Sarkar, A., Roy, R., Sherwen, T., Cuevas, C., Saiz-Lopez, A., Ram, K., and Mahajan, A. S.: Estimation of reactive inorganic iodine fluxes in the Indian and Southern Ocean marine boundary layer, *Atmos. Chem. Phys.*, 20, 12093–12114, https://doi.org/10.5194/acp-20-12093-2020, 2020.

IPCC (Intergovenmental Panel on Climate Change), ***Climate Change 2021: The Physical Science Basis. Contribution of Working Group I to the Sixth Assessment Report of the Intergovernmental Panel on Climate Change,*** edited by V. Masson-Delmotte, P. Zhai, A. Pirani, S.L. Connors, C. Péan, S. Berger, N. Caud, Y. Chen, L. Goldfarb, M.I. Gomis, M. Huang, K. Leitzell, E. Lonnoy, J.B.R. Matthews, T.K. Maycock, T. Waterfield, O. Yelekçi, R. Yu, and B. Zhou, Cambridge University Press, Cambridge, United Kingdom and New York, NY, USA, In press, doi:10.1017/9781009157896.

Ivy, D.J., T. Arnold, C.M. Harth, L.P. Steele, J. Mühle, M. Rigby, P.K. Salameh, M. Leist, P.B. Krummel, P.J. Fraser, R.F. Weiss, and R.G. Prinn, Atmospheric histories and growth trends of C_4F_{10}, C_5F_{12}, C_6F_{14}, C_7F_{16} and C_8F_{18}, *Atmos. Chem. Phys.*, *12* (9), 4313–4325, doi:10.5194/acp-12-4313-2012, 2012.

Jiao, Y., A. Ruecker, M.J. Deventer, A.T. Chow, and R.C. Rhew, Halocarbon emissions from a degraded forested wetland in coastal South Carolina impacted by sea level rise, *ACS Earth Space Chem.*, *2* (10), 955–967, doi:10.1021/acsearthspacechem.8b00044, 2018.

Jiao Y., J. Acdan, R. Xu, M.J. Deventer, W. Zhang, and R.C. Rhew, Global methyl halide emissions from rapeseed (Brassica napus) using life cycle measurements, *Geophys. Res. Lett.*, *47* (19), e2020GL089373, doi:10.1029/2020GL089373, 2020.

Jiao, Y., W. Zhang, J.Y.R. Kim, M.J. Deventer, J. Vollering, and R.C. Rhew, Application of copper (II)-based chemicals induces CH3Br and CH3Cl emissions from soil and seawater, *Nat. Commun.*, *13* (1), 1–8, doi:10.1038/s41467-021-27779-3, 2022.

Jones, C.E., S.J. Andrews, L.J. Carpenter, C. Hogan, F.E. Hopkins, J.C. Laube, A.D. Robinson, T.G. Spain, S.D. Archer, N.R.P. Harris, P.D. Nightingale, S.J. O'Doherty, D.E. Oram, J.A. Pyle, J.H. Butler, and B.D. Hall, Results from the first national UK inter-laboratory calibration for very short-lived halocarbons, *Atmos. Meas. Tech.*, *4* (5), 865–874, doi:10.5194/amt-4-865-2011, 2011.

Keber, T., H. Bönisch, C. Hartick, M. Hauck, F. Lefrancois, F. Obersteiner, A. Ringsdorf, N. Schohl, T. Schuck, R. Hossaini, P. Graf, P. Jöckel, and A. Engel, Bromine from short-lived source gases in the extratropical northern hemispheric upper troposphere and lower stratosphere (UTLS), *Atmos. Chem. Phys.*, *20* (7), 4105–4132, doi:10.5194/acp-20-4105-2020, 2020.

Keng, F.S.-L., S.-M. Phang, N. Abd Rahman, H.-Y. Yeong, G. Malin, E. Leedham Elvidge, W. Sturges, Halocarbon emissions by selected tropical seaweeds exposed to different temperatures, *Phytochemistry*, *190*, 112869, doi:10.1016/j.phytochem.2021.112869, 2021.

Kim, J., R. Thompson, H. Park, S. Bogle, J. Mühle, M. Park, Y. Kim, C.M. Harth, P.K. Salameh, R. Schmidt, D. Ottinger, S. Park, and R.F. Weiss, Emissions of tetrafluoromethane (CF4) and hexafluoroethane (C2F6) from East Asia: 2008 to 2019, *J. Geophys. Res. Atmos.*, *126* (16), doi:10.1029/2021jd034888, 2021.

Klobas, J.E., D.K. Weisenstein, R.J. Salawitch, and D.M. Wilmouth, Reformulating the bromine alpha factor and equivalent effective stratospheric chlorine (EESC): evolution of ozone destruction rates of bromine and chlorine in future climate scenarios, *Atmos. Chem. Phys.*, *20* (15), 9459–9471, doi:10.5194/acp-20-9459-2020, 2020.

Klobas, J.E., J. Hansen, D.K. Weisenstein, R.P. Kennedy, and D.M. Wilmouth, Sensitivity of iodine-mediated stratospheric ozone loss chemistry to future chemistry-climate scenarios, *Front. Earth Sci.*, *9*, 617586, doi:10.3389/feart.2021.617586, 2021.

Kloss, C., M.J. Newland, D.E. Oram, P.J. Fraser, C.A.M. Brenninkmeijer, T. Rockmann, and J.C. Laube, Atmospheric abundances, trends and emissions of CFC-216ba, CFC-216ca and HCFC-225ca, *Atmosphere*, *5* (2), 420–434, doi:10.3390/atmos5020420, 2014.

Ko, M.K.W., and G. Poulet (Lead Authors), D.R. Blake, O. Boucher, J.H. Burkholder, M. Chin, R.A. Cox, C. George, H.-F. Graf, J.R. Holton, D.J. Jacob, K.S. Law, M.G. Lawrence, P.M. Midgley, P.W. Seakins, D.E. Shallcross, S.E. Strahan, D.J. Wuebbles, and Y. Yokouchi, Very short-lived halogen and sulfur substances, Chapter 2 in ***Scientific Assessment of Ozone Depletion: 2002***, Global Ozone Research and Monitoring Project–Report No. 47, World Meteorological Organization, Geneva, Switzerland, 2003.

Koenig T.K., S. Baidar, P. Campuzano-Jost, C.A. Cuevas, B. Dix, R.P. Fernandez, H. Guo, S.R. Hall, D. Kinnison, B. Nault, K. Ullmann, J.L. Jimenez, S.-L. Alfonso, and R. Volkamer, Quantitative detection of iodine in the stratosphere, *Proc. Natl. Acad. Sci.*, *117* (4) 1860–1866; doi:10.1073/pnas.1916828117, 2020.

Koluso, S.R., S.H. Schlünzen, D. Grawe, and R. Seifert, Determination of chloromethane and dichloromethane in a tropical terrestrial mangrove forest in Brazil by measurements and modelling, *Atmos. Environ.*, *173*, 185–197, doi:10.1016/j.atmosenv.2017.10.057, 2018.

Kuyper, B., D. Say, C. Labuschagne, T. Lesch, W.R. Joubert, D. Martin, D. Young, M.A.H. Khan, M. Rigby, A.L. Ganesan, and M.F. Lunt, Atmospheric HCFC-22, HFC-125, and HFC-152a at Cape Point, South Africa, *Environ. Sci. Technol.*, *53* (15), 8967–8975, doi:10.1021/acs.est.9b01612, 2019.

Laube, J.C., P. Martinerie, E. Witrant, T. Blunier, J. Schwander, C.A.M. Brenninkmeijer, T.J. Schuck, M. Bolder, T. Röckmann, C. van der Veen, H. Bönisch, A. Engel, G.P. Mills, M.J. Newland, D.E. Oram, C.E. Reeves, and W.T. Sturges, Accelerating growth of HFC-227ea (1,1,1,2,3,3,3-heptafluoropropane) in the atmosphere, *Atmos. Chem. Phys.*, *10* (13), 5903–5910, doi:10.5194/acp-10-5903-2010, 2010.

Laube, J.C., M.J. Newland, C. Hogan, C.A.M. Brenninkmeijer, P.J. Fraser, P. Martinerie, D.E. Oram, C.E. Reeves, T. Rockmann, J. Schwander, E. Witrant, and W.T. Sturges, Newly detected ozone-depleting substances in the atmosphere, *Nat. Geosci.*, *7* (4), 266–269, doi:10.1038/ngeo2109, 2014.

Laube, J.C., N.M. Hanif, P. Martinerie, E. Gallacher, P.J. Fraser, R. Langenfelds, C.A.M. Brenninkmeijer, J. Schwander, E. Witrant, J.L. Wang, C.F. Ou-Yang, L.J. Gooch, C.E. Reeves, W.T. Sturges, and D.E. Oram, Tropospheric observations of CFC-114 and CFC-114a with a focus on long-term trends and emissions, *Atmos. Chem. Phys.*, *6* (23), 15,347–15,358, doi:10.5194/acp-16-15347-2016, 2016.

Laube, J.C., E.C.L. Elvidge, K.E. Adcock, B. Baier, C.A.M. Brenninkmeijer, H. Chen, E.S. Droste, J.-U. Grooß, P. Heikkinen, A.J. Hind, R. Kivi, A. Lojko, S.A. Montzka, D.E. Oram, S. Randall, T. Röckmann, W.T. Sturges, C. Sweeney, M. Thomas, E. Tuffnell, and F. Ploeger, Investigating stratospheric changes between 2009 and 2018 with halogenated trace gas data from aircraft, AirCores, and a global model focusing on CFC-11, *Atmos. Chem. Phys.*, *20* (16), 9771–9782, doi:10.5194/acp-20-9771-2020, 2020.

Lauther, V., B. Vogel, J. Wintel, A. Rau, P. Hoor, V. Bense, R. Müller, and C.M. Volk, In situ observations of CH_2Cl_2 and $CHCl_3$ show efficient transport pathways for very short-lived species into the lower stratosphere via the Asian and the North American summer monsoon, *Atmos. Chem. Phys.*, *22* (3), 2049–2077, doi:10.5194/acp-22-2049-2022, 2022.

Lawler, M.J., A.S. Mahajan, A. Saiz-Lopez, and E.S. Saltzman, Observations of I_2 at a remote marine site, ***Atmos. Chem. Phys.***, ***14*** (5), 2669–2678, doi:10.5194/acp-14-2669-2014, 2014.

Leedham, E.C., C. Hughes, F.S. L. Keng, S.-M. Phang, G. Malin, and W.T. Sturges, Emission of atmospherically significant halocarbons by naturally occurring and farmed tropical macroalgae, ***Biogeosciences***, ***10***, 3615–3633, doi:10.5194/bg-10-3615-2013, 2013.

Leedham Elvidge, E., H. Bönisch, C.A.M. Brenninkmeijer, A. Engel, P.J. Fraser, E. Gallacher, R. Langenfelds, J. Mühle, D.E. Oram, E.A. Ray, A.R. Ridley, T. Röckmann, W.T. Sturges, R.F. Weiss, and J.C. Laube, Evaluation of stratospheric age of air from CF_4, C_2F_6, C_3F_8, CHF_3, HFC-125, HFC-227ea and SF_6: Implications for the calculations of halocarbon lifetimes, fractional release factors and ozone depletion potentials, ***Atmos. Chem. Phys.***, ***18*** (5), 3369–3385, doi:10.5194/acp-18-3369-2018, 2018.

Legrand, M., J.R. McConnell, S. Preunkert, M. Arienzo, N. Chellman, K. Gleason, T. Sherwen, M.J. Evans, and L.J. Carpenter, Alpine ice evidence of a three-fold increase in atmospheric iodine deposition since 1950 in Europe due to increasing oceanic emissions, ***Proc. Natl. Acad. Sci.***, ***115*** (48), 12,136–12,141, doi:10.1073/pnas.1809867115, 2018.

Lelieveld, J., E. Bourtsoukidis, C. Brühl, H. Fischer, H., Fuchs, H. Harder, A. Hofzumahaus, F. Holland, D. Marno, M. Neumaier, A. Pozzer, H. Schlager, J. Williams, A. Zahn, and H. Ziereis, The South Asian monsoon—pollution pump and purifier, ***Science***, ***361*** (6399), 270–273, doi:10.1126/science.aar2501, 2018.

Lennartz, S.T., C.A. Marandino, M. von Hobe, P. Cortes, B. Quack, R. Simo, D. Booge, A. Pozzer, T. Steinhoff, D.L. Arevalo-Martinez, C. Kloss, A. Bracher, R. Röttgers, E. Atlas, and K. Krüger, Direct oceanic emissions unlikely to account for the missing source of atmospheric carbonyl sulfide, ***Atmos. Chem. Phys.***, ***17***, 385–402, doi:10.5194/acp-17-385-2017, 2017.

Li, Z., P. Bie, Z. Wang, Z. Zhang, H. Jiang, W. Xu, J. Zhang, and J. Hu, Estimated HCFC-22 emissions for 1990–2050 in China and the increasing contribution to global emissions, ***Atmos. Environ., 132***, 77–84, doi:10.1016/j.atmosenv.2016.02.038, 2016.

Li, S., M.-K. Park, C.O. Jo, and S. Park, Emission estimates of methyl chloride from industrial sources in China based on high frequency atmospheric observations, ***J. Atmos. Chem.***, ***74***, 227–243, doi:10.1007/s10874-016-9354-4, 2017.

Liang, Q., R.S. Stolarski, S.R. Kawa, J.E. Nielsen, J.M. Rodriguez, A.R. Douglass, J.M. Rodriguez, D.R. Blake, E.L. Atlas, and L.E. Ott, Finding the missing stratospheric Bry: A global modeling study of $CHBr_3$ and CH_2Br_2, ***Atmos. Chem. Phys.***, ***10*** (5), 2269–2286, doi:10.5194/acp-10-2269-2010, 2010.

Liang, Q., P.A. Newman, and S. Reimann, SPARC Report on the Mystery of Carbon Tetrachloride, SPARC Report No. 7, WCRP-13/2016, [available at: https://www.wcrp-climate.org/WCRP-publications/2016/SPARC_Report7_2016.pdf], 2016.

Lickley, M., S. Solomon, S. Fletcher, G.J.M. Velders, J. Daniel, M. Rigby, S.A. Montzka, L.J.M. Kuijpers, and K. Stone, Quantifying contributions of chlorofluorocarbon banks to emissions and impacts on the ozone layer and climate, ***Nat. Commun.***, ***11*** (1380), doi:10.1038/s41467-020-15162-7, 2020.

Lickley, M., S. Solomon, D. Kinnison, P. Krummel, J. Mühle, S, O'Doherty, S., R. Prinn, M. Rigby, K.A. Stone, P. Wang, R. Weiss, and D. Young , Quantifying the imprints of stratospheric contributions to interhemispheric differences in tropospheric CFC-11, CFC-12, and N_2O abundances, ***Geophys. Res. Lett.***, ***48*** (15), e2021GL093700, doi:10.1029/2021GL093700, 2021.

Lin, Y., D. Gong, S. Lv, Y. Ding, G. Wu, H. Wang, Y. Li, Y. Wang, L. Zhou, and B. Wang, Observations of high levels of ozone-depleting CFC-11 at a remote mountain-top site in Southern China, ***Environ. Sci. Technol. Lett.***, ***6*** (3), 114–118, doi:10.1021/acs.estlett.9b00022, 2019.

Lunt, M.F., S. Park, S. Li, S. Henne, A.J. Manning, A.L. Ganesan, I.J. Simpson, D.R. Blake, Q. Liang, S. O'Doherty, C.M. Harth, J. Mühle, P.K. Salameh, R.F. Weiss, P.B. Krummel, P.J. Fraser, R.G. Prinn, S. Reimann, and M. Rigby, Continued emissions of the ozone-depleting substance carbon tetrachloride from eastern Asia, ***Geophys. Res. Lett.***, ***45*** (20), 11,423–11,430, doi:10.1029/2018GL079500, 2018

Ma, J., L.M.J. Kooijmans, A. Cho, S.A. Montzka, N. Glatthor, J.R. Worden, L. Kuai, E.L. Atlas, and M.C. Krol, Inverse modelling of carbonyl sulfide: implementation, evaluation and implications for the global budget, ***Atmos. Chem. Phys.***, ***21*** (5), 3507–3529, doi:10.5194/acp-21-3507-2021, 2021.

Maas, J., S. Tegtmeier, B. Quack, A. Biastoch, J.V. Durgadoo, S. Rühs, S. Gollasch, and M. David, Simulating the spread of disinfection by-products and anthropogenic bromoform emissions from ballast water discharge in Southeast Asia, ***Ocean Sci.***, ***15*** (4), 891–904, doi:10.5194/os-15-891-2019, 2019.

Maas, J., S. Tegtmeier, Y. Jia, B. Quack, J.V. Durgadoo, and A. Biastoch, Simulations of anthropogenic bromoform indicate high emissions at the coast of East Asia, ***Atmos. Chem. Phys.***, 21, 4103–4121, doi:10.5194/acp-21-4103-2021, 2021.

Mahieu, E., M.P. Chipperfield, J. Notholt, T. Reddmann, J. Anderson, P.F. Bernath, T. Blumenstock, M.T. Coffey, S.S. Dhomse, W. Feng, B. Franco, L. Froidevaux, D.W.T. Griffith, J.W. Hannigan, F. Hase, R. Hossaini, N.B. Jones, I. Morino, I. Murata, H. Nakajima, M. Palm, C. Paton-Walsh, J.M. Russell, M. Schneider, C. Servais, D. Smale, and K.A. Walker, Recent Northern Hemisphere stratospheric HCl increase due to atmospheric circulation changes, ***Nature***, ***515*** (7525), 104–107, doi:10.1038/nature13857, 2014a.

Mahieu, E., R. Zander, G.C. Toon, M.K. Vollmer, S. Reimann, J. Mühle, W. Bader, B. Bovy, B. Lejeune, C. Servais, P. Demoulin, G. Roland, P.F. Bernath, C.D. Boone, K.A. Walker, and P. Duchatelet, Spectrometric monitoring of atmospheric carbon tetrafluoride (CF_4) above the Jungfraujoch station since 1989: evidence of continued increase but at a slowing rate, ***Atmos. Meas. Tech.***, ***7*** (1), 333–344, doi:10.5194/amt-7-333-2014, 2014b.

Mahieu, E., B. Lejeune, B. Bovy, C. Servais, G.C. Toon, P.F. Bernath, C.D. Boone, K.A. Walker, S. Reimann, M.K. Vollmer, and S. O'Doherty, Retrieval of HCFC-142b (CH_3CClF_2) from ground-based high-resolution infrared solar spectra: Atmospheric increase since 1989 and comparison with surface and satellite measurements, ***J. Quant. Spectrosc. Radiat. Trans.***, ***186***, 96–105, doi:10.1016/j.jqsrt.2016.03.017, 2017.

Macdonald, M.L., J.L. Wadham, D. Young, C.R. Lunder, O. Hermansen, G. Lamarche-Gagnon, and S. O'Doherty, Consumption of CH_3Cl, CH_3Br, and CH_3I and emission of $CHCl_3$, $CHBr_3$, and CH_2Br_2 from the forefield of a retreating Arctic glacier, ***Atmos. Chem. Phys.***, ***20*** (12), 7243–7258, doi:10.5194/acp-20-7243-2020, 2020.

MacDonald, S.M., J.C. Gómez Martín, R. Chance, S. Warriner, A. Saiz-Lopez, L.J. Carpenter, and J.M.C. Plane, A laboratory characterisation of inorganic iodine emissions from the sea surface: dependence on oceanic variables and parameterisation for global modelling, ***Atmos. Chem. Phys.***, ***14*** (11), 5841–5852, doi:10.5194/acp-14-5841-2014, 2014.

Maione, M., F. Graziosi, J. Arduini, F. Furlani, U. Giostra, D.R. Blake, P. Bonasoni, X. Fang, X., S.A. Montzka, S.J. O'Doherty, S. Reimann, A. Stohl, and M.K. Vollmer, Estimates of European emissions of methyl chloroform using a Bayesian inversion method, ***Atmos. Chem. Phys.***, ***14***, 9755–9770, doi:10.5194/acp-14-9755-2014, 2014.

Manley, S.L., N.-Y. Wang, M.L. Walser, and R.J. Cicerone, Methyl halide emissions from greenhouse-grown mangroves, ***Geophys. Res. Lett.***, ***34*** (1), doi:10.1029/2006GL027777, 2007.

McCulloch, A., Chloroform in the environment: occurrence, sources, sinks and effects, ***Chemosphere***, ***50*** (10), 1291–1308, doi:10.016/S0045-6535(02)00697-5, 2003.

Mead, M.I., M.A.H. Khan, I.R. White, G. Nickless, D.E. Shallcross, Methyl halide emission estimates from domestic biomass burning in Africa, ***Atmos. Environ.***, ***42*** (21), 5241–5250, doi:10.1016/j.atmosenv.2008.02.066, 2008.

Miller, B.R., R.F. Weiss, P.K. Salameh, T. Tanhua, B.R. Greally, J. Muhle, and P.G. Simmonds, Medusa: A sample preconcentration and GC/MS detector system for ***in situ*** measurements of atmospheric trace halocarbons, hydrocarbons, and sulfur compounds, ***Anal. Chem.***, ***80*** (5), 1536–1545, doi:10.1021/ac702084k, 2008.

Montzka, S.A., J.H. Butler, B.D. Hall, D.J. Mondeel, and J.W. Elkins, A decline in tropospheric organic bromine, ***Geophys. Res. Lett.***, ***30*** (15), 1826–1826, doi:10.1029/2003GL017745, 2003.

Montzka, S.A., and P.J. Fraser (Lead Authors), J.H. Butler, P.S. Connell, D.M. Cunnold, J.S. Daniel, R.G. Derwent, S. Lal, A. McCulloch, D.E. Oram, C.E. Reeves, E. Sanhueza, L.P. Steele, G.J.M. Velders, R.F. Weiss, and R.J. Zander, Controlled substances and other source gases, Chapter 1 in Scientific Assessment of Ozone Depletion: 2002, Global Ozone Research and Monitoring Project–Report No. 47, Geneva, Switzerland, 2003.

Montzka, S.A., and S. Reimann, (Coordinating Lead Authors) A. Engel, K. Krüger, S. O`Doherty, and W.T. Sturges, Ozone-Depleting Substances (ODSs) and Related Chemicals, Chapter 1 in ***Scientific Assessment of Ozone Depletion: 2010***, Global Ozone Research and Monitoring Project–Report No. 52, World Meteorological Organization, Geneva, Switzerland, 2010.

Montzka, S.A., M. McFarland, S.O. Andersen, B.R. Miller, D.W. Fahey, B.D. Hall, L. Hu, C. Siso, and J.W. Elkins, Recent trends in global emissions of hydrochlorofluorocarbons and hydrofluorocarbons: Reflecting on the 2007 adjustments to the Montreal Protocol, ***J. Phys. Chem. A***, ***119*** (19), 4439–4449, doi:10.1021/jp5097376, 2015.

Montzka, S.A., G.S. Dutton, P. Yu, E. Ray, R.W. Portmann, J.S. Daniel, L. Kuijpers, B.D. Hall, D. Mondeel, C. Siso, J.D. Nance, M. Rigby, A.J. Manning, L. Hu, F. Moore, B.R. Miller, and J.W. Elkins, An unexpected and persistent increase in global emissions of ozone-depleting CFC-11, ***Nature, 557***, 413–417, doi:10.1038/s41586-018-0106-2, 2018.

Montzka, S.A., G.S. Dutton, R.W. Portmann, M.P. Chipperfield, S. Davis, W. Feng, A.J. Manning, E. Ray, M. Rigby, B.D. Hall, C. Siso, J.D. Nance, P.B. Krummel, J. Mühle, D. Young, S. O'Doherty, P.K. Salameh, C.M. Harth, R.G. Prinn, R.F. Weiss, J. W. Elkins, H. Walter-Terrinoni, and C. Theodoridi, A decline in global CFC-11 emissions during 2018–2019, ***Nature, 590***, 428–432, doi:10.1038/s41586-021-03260-5, 2021.

Mühle, J., J. Huang, R.F. Weiss, R.G. Prinn, B.R. Miller, P.K. Salameh, C.M. Harth, P.J. Fraser, L.W. Porter, B.R. Greally, S. O'Doherty, and P.G. Simmonds, Sulfuryl fluoride in the global atmosphere, ***J. Geophys. Res. Atmos.***, ***114*** (D5), doi:10.1029/2008JD011162, 2009.

Mühle, J., C.M. Trudinger, L.M. Western, M. Rigby, M.K. Vollmer, S. Park, A.J. Manning, D. Say, A. Ganesan, L.P. Steele, D.J. Ivy, T. Arnold, S. Li, A. Stohl, C.M. Harth, P.K. Salameh, A. McCulloch, S. O'Doherty, M.-K. Park, C.O. Jo, D. Young, K.M. Stanley, P.B. Krummel, B. Mitrevski, O. Hermansen, C. Lunder, N. Evangeliou, B. Yao, J. Kim, B. Hmiel, C. Buizert, V.V. Petrenko, J. Arduini, M. Maione, D.M. Etheridge, E. Michalopoulou, M. Czerniak, J.P. Severinghaus, S. Reimann, P.G. Simmonds, P.J. Fraser, R.G. Prinn, and R.F. Weiss, Perfluorocyclobutane (PFC-318, c-C_4F_8) in the global atmosphere, ***Atmos. Chem. Phys.***, ***19*** (15), 10,335–10,359, doi:10.5194/acp-19-10335-2019, 2019.

Mühle, J., L.J.M. Kuijpers, K.M. Stanley, M. Rigby, L.M. Western, J. Kim, S. Park, C.M. Harth, P.B. Krummel, P.J. Fraser, S. O'Doherty, P.K. Salameh, R. Schmidt, D. Young, R.G. Prinn, R.H.J. Wang, and R.F. Weiss, Global emissions of perfluorocyclobutane (PFC-318, c-C4F8) resulting from the use of hydrochlorofluorocarbon-22 (HCFC-22) feedstock to produce polytetrafluoroethylene (PTFE) and related fluorochemicals, ***Atmos. Chem. Phys.***, ***22***, 3371–3378, doi:10.5194/acp-22-3371-2022, 2022.

Müller, R., The impact of the rise in atmospheric nitrous oxide on stratospheric ozone, ***Ambio***, ***50***, 35–39, doi:10.1007/s13280-020-01428-3, 2021

Navarro, M.A., E.L. Atlas, A. Saiz-Lopez, X. Rodriguez-Lloveras, D.E. Kinnison, J.F. Lamarque, S. Tilmes, M. Filus, N.R.P. Harris, E. Meneguz, M.J. Ashfold, A.J. Manning, C.A. Cuevas, S.M. Schauffler, and V. Donets, Airborne measurements of organic bromine compounds in the Pacific tropical tropopause layer, ***Proc. Natl. Acad. Sci.***, ***112*** (45), 13,789–13,793, doi:10.1073/pnas.1511463112, 2015.

Newland, M.J., C.E. Reeves, D.E. Oram, J.C. Laube, W.T. Sturges, C. Hogan, P. Begley, and P.J. Fraser, Southern hemispheric halon trends and global halon emissions, 1978–2011, ***Atmos. Chem. Phys.***, ***13*** (11), 5551–5565, doi:10.5194/acp-13-5551-2013, 2013.

Newman, P.A., J.S. Daniel, D.W. Waugh, and E.R. Nash, A new formulation of equivalent effective stratospheric chlorine (EESC), ***Atmos. Chem. Phys.***, ***7*** (17), 4537–4552, doi:10.5194/acp-7-4537-2007, 2007.

Nicewonger, M. R., E.S. Saltzman, and S. A. Montzka, ENSO-driven fires cause large interannual variability in the naturally emitted, ozone-depleting trace gas CH_3Br, ***Geophys. Res. Lett.***, 49, e2021GL094756, doi:10.1029/2021GL094756, 2022.

O'Doherty, S., D.M. Cunnold, A. Manning, B.R. Miller, R.H.J. Wang, P.B. Krummel, P.J. Fraser, P.G. Simmonds, A. McCulloch, R.F. Weiss, P. Salameh, L.W. Porter, R.G. Prinn, J. Huang, G. Sturrock, D. Ryall, R.G. Derwent, and S.A. Montzka, Rapid growth of hydrofluorocarbon 134a and hydrochlorofluorocarbons 141b, 142b, and 22 from advanced global atmospheric gases experiment (AGAGE) observations at Cape Grim, Tasmania, and Mace Head, Ireland, ***J. Geophys. Res.***, ***109*** (D6), D06310, doi:10.1029/2003JD004277, 2004.

Oram, D.E., F.S. Mani, J.C. Laube, M.J. Newland, C.E. Reeves, W.T. Sturges, S.A. Penkett, C.A.M. Brenninkmeijer, T. Rockmann, and P.J. Fraser, Long-term tropospheric trend of octafluorocyclobutane (c-C_4F_8 or PFC-318), ***Atmos. Chem. Phys.***, ***12*** (1), 261–269, doi:10.5194/acp-12-261-2012, 2012.

Ordóñez, C., J.-F. Lamarque, S. Tilmes, D.E. Kinnison, E.L. Atlas, D.R. Blake, G. Sousa Santos, G. Brasseur, and A. Saiz-Lopez, Bromine and iodine chemistry in a global chemistry-climate model: Description and evaluation of very short-lived oceanic sources, ***Atmos. Chem. Phys.***, ***12*** (3), 1423-1447, doi:10.5194/acp-12-1423-2012, 2012.

Orkin, V.L., M.J. Kurylo, and E.L. Fleming, Atmospheric lifetimes of halogenated hydrocarbons: Improved estimations from an analysis of modeling results, ***J. Geophys. Res.***, ***125*** (16), e2019JD032243, doi:10.1029/2019JD032243, 2020.

Ostermöller, J., H. Bönisch, P. Jöckel, and A. Engel, A new time-independent formulation of fractional release, ***Atmos. Chem. Phys.***, ***17 (***6), 3785–3797, doi:10.5194/acp-17-3785-2017, 2017.

Pan, L.L., E.L. Atlas, R.J. Salawitch, S.B. Honomichl, J.F. Bresch, W.J. Randel, E.C. Apel, R.S. Hornbrook, A J. Weinheimer, D.C. Anderson, S.J. Andrews, S. Baidar, S.P. Beaton, T.L. Campos, L.J. Carpenter, D. Chen, B. Dix, V. Donets, S.R. Hall, T.F. Hanisco, C.R. Homeyer, L.G. Huey, J.B. Jensen, L. Kaser, D.E. Kinnison, T.K. Koenig, J.F. Lamarque, C. Liu, J. Luo, Z.J. Luo, D.D. Montzka, J.M. Nicely, R.B. Pierce, D.D. Riemer, T. Robinson, P. Romashkin, A. Saiz-Lopez, S. Schauffler, O. Shieh, M.H. Stell, K. Ullmann, G. Vaughan, R. Volkamer, and G. Wolfe, The convective transport of active species in the tropics (CONTRAST) experiment, ***Bull. Am. Meteorol. Soc.***, ***98*** (1), 106–128, doi:10.1175/bams-d-14-00272.1, 2017.

Park, S., L.M. Western, T. Saito, A.L. Redington, S. Henne, X. Fang, R.G. Prinn, A.J. Manning, S.A. Montzka, P.J. Fraser, A.L. Ganesan, C.M. Harth, J. Kim, P.B. Krummel, Q. Liang, J. Mühle, S. O'Doherty, H. Park, M.-K. Park, S. Reimann, P.K. Salameh, R.F. Weiss, and M. Rigby, A decline in emissions of CFC-11 and related chemicals from eastern China, ***Nature, 590***, 433–437, doi:10.1038/s41586-021-03277, 2021.

Parrella, J.P., K. Chance, R.J. Salawitch, T. Canty, M. Dorf, and K. Pfeilsticker, New retrieval of BrO from SCIAMACHY limb: an estimate of the stratospheric bromine loading during April 2008, ***Atmos. Meas. Tech.***, ***6*** (10), 2549–2561, doi:10.5194/amt-6-2549-2013, 2013.

Patterson, J.D., M. Aydin, A.M. Crotwell, G. Pétron, J.P. Severinghaus, and E.S. Saltzman, Atmospheric history of H_2 over the past century reconstructed from South Pole firn air, ***Geophy. Res. Lett.***, ***47*** (14), e2020GL087787, doi:10.1029/2020GL087787, 2020.

Patterson, J.D., M. Aydin, A.M. Crotwell, G. Pétron, J.P. Severinghaus, P.B. Krummel, R.L. Langenfelds, and E.S. Saltzman, H_2 in Antarctic firn air: atmospheric reconstructions and implications for anthropogenic emissions, ***Proc. Natl. Acad. Sci.***, ***118*** (36), e2103335118, doi:10.1073/pnas.2103335118, 2021.

Pisso, I., P.H. Haynes, and K.S. Law, Emission location dependent ozone depletion potentials for very short-lived halogenated species, ***Atmos. Chem. Phys.***, ***10***, 12,025–12,036, doi:10.5194/acp-10-12025-2010, 2010.

Ploeger, F., P. Konopka, K. Walker, and M. Riese: Quantifying pollution transport from the Asian monsoon anticyclone into the lower stratosphere, ***Atmos. Chem. Phys.***, 17, 7055–7066, doi:10.5194/acp-17-7055-2017, 2017.

Prados-Roman, C., C.A. Cuevas, R.P. Fernandez, D.E. Kinnison, J.-F. Lamarque, and A. Saiz-Lopez, A negative feedback between anthropogenic ozone pollution and enhanced ocean emissions of iodine, ***Atmos. Chem. Phys.***, ***15*** (4), 2215–2224, doi:10.5194/acp-15-2215-2015, 2015.

Prignon, M., S. Chabrillat, D. Minganti, S. O'Doherty, C. Servais, G. Stiller, G.C. Toon, M.K. Vollmer, and E. Mahieu, Improved FTIR retrieval strategy for HCFC-22 (CHClF 2), comparisons with in situ and satellite datasets with the support of models, and determination of its long-term trend above Jungfraujoch, ***Atmos. Chem. Phys.***, ***19*** (19), 12,309–12,324, doi:10.5194/acp-19-12309-2019, 2019.

Prignon, M., S. Chabrillat, M. Friedrich, D. Smale, S.E. Strahan, P.F. Bernath, M.P. Chipperfield, S.S. Dhomse, W. Feng, D. Minganti, C. Servais, and E. Mahieu, Stratospheric fluorine as a tracer of circulation changes: Comparison between infrared remote-sensing observations and simulations with five modern reanalyses, ***J. Geophys. Res.***, ***126*** (19), e2021JD034995. doi:10.1029/2021JD034995, 2021.

Prinn, R.G., R.F. Weiss, P.J. Fraser, P.G. Simmonds, D.M. Cunnold, F.N. Alyea, S. O'Doherty, P. Salameh, B.R. Miller, J. Huang, R.H.J. Wang, D.E. Hartley, C. Harth, L.P. Steele, G. Sturrock, P.M. Midgley, and A. McCulloch, A history of chemically and radiatively important gases in air deduced from ALE/GAGE/AGAGE, ***J. Geophys. Res.***, ***105*** (D14), 17,751–17,792, doi:10.1029/2000JD900141, 2000.

Prinn, R.G., R.F. Weiss, J. Arduini, T. Arnold, H.I. DeWitt, P.J. Fraser, A.L. Ganesan, J. Gasore, C.M. Harth, O. Hermansen, J. Kim, P.B. Krummel, S. Li, Z. M. Loh, C.R. Lunder, M. Maione, A.J. Manning, B.R. Miller, B. Mitrevski, J. Mühle, S. O'Doherty, S. Park, S. Reimann, M. Rigby, T. Saito, P.K. Salameh, R. Schmidt, P.G. Simmonds, L.P. Steele, M.K. Vollmer, R.H. Wang, B. Yao, Y. Yokouchi, D. Young, and L. Zhou, History of chemically and radiatively important atmospheric gases from the Advanced Global Atmospheric Gases Experiment (AGAGE), ***Earth Syst. Sci. Data***, ***10*** (2), 985–1018, doi:10.5194/essd-10-985-2018, 2018.

Quivet, E., P. Höhener, B. Temime-Roussel, J. Dron, G. Revenko, M. Verlande, K. Lebaron, C. Demelas, L. Vassalo, and J.-L. Boudenne, Underestimation of anthropogenic bromoform released into the environment?, ***Environ. Sci. Technol.***, ***56*** (3), 1522–1533, doi:10.1021/acs.est.1c05073, 2022.

Ramaswamy, V., O. Boucher, J.D. Haigh, D.A. Hauglustaine, J.M. Haywood, G. Myrhe, T. Nakajima, G.Y. Shi, and S. Solomon, Radiative Forcing of Climate Change, Chapter 6, in ***Climate Change 2001: The Scientific Basis, Contribution of Working Group I to the Third Assessment Report of the Intergovernmental Panel on Climate Change***, edited by F. Joos, and J. Srinivasan, Cambridge University Press,

Cambridge, United Kingdom and New York, NY, 68 pp., [available at: https://www.ipcc.ch/site/assets/uploads/2018/03/TAR-06.pdf], 2001.

Ravishankara, A.R., J.S. Daniel, and R.W. Portmann, Nitrous oxide (N2O): The dominant ozone-depleting substance emitted in the 21st century, ***Science***, ***326***, 123–125, doi:10.1126/science.1176985, 2009.

Ray, E.A., R.W. Portmann, P. Yu, J. Daniel, S.A. Montzka, G.S. Dutton, B.D. Hall, F.L. Moore, and K.H. Rosenlof, The influence of the stratospheric Quasi-Biennial Oscillation on trace gas levels at the Earth's surface, ***Nat. Geosci.***, ***13***, 22–27, doi:10.1038/s41561-019-0507-3, 2020.

Read, K.A., A.S. Mahajan, L.J. Carpenter, M.J. Evans, B.V.E. Faria, D.E. Heard, J.R. Hopkins, J.D. Lee, S.J. Moller, A.C. Lewis, L.M. Mendes, J.B. McQuaid, H. Oetjen, A. Saiz-Lopez, M.J. Pilling, and J.M.C. Plane, Extensive halogen-mediated ozone destruction over the tropical Atlantic Ocean, ***Nature***, ***453***, 1232–1235, doi:10.1038/nature07035, 2008.

Revell, L.E., Tummon, F., Salawitch, R.J., Stenke, A., and T. Peter, The changing ozone depletion potential of N_2O in a future climate, ***Geophys. Res. Lett.***, ***42***, 10,047–10,055, doi:10.1002/2015GL06570, 2015.

Rex, M., I. Wohltmann, T. Ridder, R. Lehmann, K. Rosenlof, P. Wennberg, D. Weisenstein, J. Notholt, K. Kruger, V. Mohr, and S. Tegtmeier, A tropical West Pacific OH minimum and implications for stratospheric composition, ***Atmos. Chem. Phys.***, ***14*** (9), 4827–4841, doi:10.5194/acp-14-4827-2014, 2014.

Rigby, M., A.L. Ganesan, and R.G. Prinn, Deriving emissions time series from sparse atmospheric mole fractions, ***J. Geophys. Res.***, ***116*** (D8), D08306, doi:10.1029/2010jd015401, 2011.

Rigby, M., R.G. Prinn, S. O'Doherty, S.A. Montzka, A. McCulloch, C.M. Harth, J. Mühle, P.K. Salameh, R.F. Weiss, D. Young, P.G. Simmonds, B.D. Hall, G.S. Dutton, D. Nance, D.J. Mondeel, J.W. Elkins, P.B. Krummel, L.P. Steele, and P.J. Fraser, Re-evaluation of the lifetimes of the major CFCs and CH_3CCl_3 using atmospheric trends, ***Atmos. Chem. Phys.***, ***13*** (5), 2691–2702, doi:10.5194/acp-13-2691-2013, 2013.

Rigby, M., R.G. Prinn, S. O'Doherty, B.R. Miller, D. Ivy, J. Mühle, C.M. Harth, P.K. Salameh, T. Arnold, R.F. Weiss, P.B. Krummel, L.P. Steele, P.J. Fraser, D. Young, and P.G. Simmonds, Recent and future trends in synthetic greenhouse gas radiative forcing, ***Geophys. Res. Lett.***, ***41*** (7), 2623–2630, doi:10.1002/2013GL059099, 2014.

Rigby, M., S. Park, T. Saito, L.M. Western, A.L. Redington, X. Fang, S. Henne, A.J. Manning, R.G. Prinn, G.S. Dutton, P.J. Fraser, A.L. Ganesan, B.D. Hall, C.M. Harth, J. Kim, K.-R. Kim, P.B. Krummel, T. Lee, S. Li, Q. Liang, M.F. Lunt, S.A. Montzka, J. Mühle, S. O'Doherty, M.-K. Park, S. Reimann, P.K. Salameh, P. Simmonds, R.L. Tunnicliffe, R.F. Weisse, Y. Yokouchi, and D. Young, Increase in CFC-11 emissions from eastern China based on atmospheric observations, ***Nature***, ***569***, 546–550, doi:10.1038/s41586-019-1193-4, 2019.

Rinsland, C.P., E. Mahieu, P. Demoulin, R. Zander, C. Servais, and J.-M. Hartmann, Decrease of the carbon tetrachloride (CCl_4) loading above Jungfraujoch, based on high resolution infrared solar spectra recorded between 1999 and 2011, ***J. Quant. Spectrosc. Radiat. Trans.***, ***113*** (11), 1322–1329, doi:10.1016/j.jqsrt.2012.02.016, 2012.

Rollins, A.W., T.D. Thornberry, L.A. Watts, P. Yu, K.H. Rosenlof, M.J. Mills, E. Baumann, F.R. Giorgetta, T.V. Bui, M. Höpfner, K.A. Walker, C. Boone, P.F. Bernath, P.R. Colarco, P.A. Newman, D.W. Fahey, and R.S. Gao, The role of sulfur dioxide in stratospheric aerosol formation evaluated by using ***in situ*** measurements in the tropical lower stratosphere, ***Geophy. Res. Lett.***, ***44*** (9), 4280–4286, doi:10.1002/2017GL072754, 2017.

Rollins, A.W., T.D. Thornberry, E. Atlas, M. Navarro, S. Schauffler, F. Moore, J.W. Elkins, E. Ray, K. Rosenlof, V. Aquila, and R.-S. Gao, SO_2 observations and sources in the western Pacific tropical tropopause region, ***J. Geophys. Res. Atmos.***, ***123*** (23), 13,549–13,559, doi:10.1029/2018JD029635, 2018.

Rotermund, M.K., V. Bense, M.P. Chipperfield, A. Engel, J.-U. Grooß, P. Hoor, T. Hüneke, T., Keber, F. Kluge, B. Schreiner, T. Schuck, B. Vogel, A. Zahn, and K. Pfeilsticker, Organic and inorganic bromine measurements around the extratropical tropopause and lowermost stratosphere: Insights into the transport pathways and total bromine, ***Atmos. Chem. Phys.***, ***21***, 15,375–15,407, doi:10.5194/acp-21-15375-2021, 2021.

Ruiz, D.J., M.J. Prather, S.E. Strahan, R.L. Thompson, L. Froidevaux, and S.D. Steenrod, How atmospheric chemistry and transport drive surface variability of N_2O and CFC-11, ***J. Geophys. Res. Atmos.***, ***126*** (8), e2020JD033979, doi:10.1029/2020JD033979, 2021.

Rust, D., I. Katharopoulos, M.K. Vollmer, S. Henne, S. O'Doherty, D. Say, L. Emmenegger, R. Zenobi, and S. Reimann, Swiss halocarbon emissions for 2019 to 2020 assessed from regional atmospheric observations, ***Atmos. Chem. Phys.***, ***22*** (4), 2447–2466, doi:10.5194/acp-2021-633, 2022.

Saito, T., Y. Yokouchi, A. Stohl, S. Taguchi, and H. Mukai, Large emissions of perfluorocarbons in East Asia deduced from continuous atmospheric measurements, ***Environ. Sci. Technol.***, ***44*** (11), 4089–4095, doi:10.1021/es1001488, 2010.

Saiz-Lopez, A., S. Baidar, C.A. Cuevas, T.K. Koenig, R.P. Fernandez, B. Dix, D.E. Kinnison, J.F. Lamarque, X. Rodriguez-Lloveras, T.L. Campos, and R. Volkamer, Injection of iodine to the stratosphere, ***Geophys. Res. Lett.***, ***42*** (16), 6852–6859, doi:10.1002/2015GL064796, 2015.

Sala, S., H. Bonisch, T. Keber, D.E. Oram, G. Mills, and A. Engel, Deriving an atmospheric budget of total organic bromine using airborne ***in situ*** measurements from the western Pacific area during SHIVA, ***Atmos. Chem. Phys.***, ***14*** (13), 6903–6923, doi:10.5194/acp-14-6903-2014, 2014.

Saltzman, E.S., M. Aydin, W.J. De Bruyn, D.B. King, and S.A. Yvon-Lewis, Methyl bromide in preindustrial air: Measurements from an Antarctic ice core, ***J. Geophys. Res.***, ***109***, D05301, doi:10.1029/2003JD004157. 2004.

Saltzman, E.S., M. Aydin, C. Tatum, and M.B. Williams, 2,000-year record of atmospheric methyl bromide from a South Pole ice core, ***J. Geophys. Res.***, ***113***, D05304, doi:10.1029/2007JD008919. 2008.

Saltzman, E.S., M.R. Nicewonger, S.A. Montzka, and S.A. Yvon-Lewis, A post-phase-out retrospective reassessment of the global methyl bromide budget, ***J. Geophys. Res.***, ***127*** (3), e2021JD035567 doi:10.1029/2021JD035567, 2022.

Say, D., A.L. Ganesan, M.F. Lunt, M. Rigby, S. O'Doherty, C. Harth, A.J. Manning, P.B. Krummel, and S. Bauguitte, Emissions of halocarbons from India inferred through atmospheric measurements, ***Atmos. Chem. Phys.***, ***19*** (15), 9865–9885, doi:10.5194/acp-19-9865-2019, 2019.

Say D., B. Kuyper, L. Western, M.A.H. Khan, T. Lesch, C. Labuschagne, D. Martin, D. Young, A.J. Manning, S. O'Doherty, M. Rigby, P.B. Krummel, M.T. Davies-Coleman, A.L. Ganesan, and D.E. Shallcross, Emissions and marine boundary layer concentrations of unregulated chlorocarbons measured at Cape Point, South Africa, ***Environ. Sci. Technol.***, ***54*** (17), 10,514–10,523, doi:10.1021/acs.est.0c02057, 2020.

Say, D., A.J. Manning, L.M. Western, D. Young, A. Wisher, M. Rigby, S. Reimann, M.K. Vollmer, M. Maione, J. Arduini, P.B. Krummel, J. Mühle, C.M. Harth, B. Evans, R.F. Weiss, R.G. Prinn, and S. O'Doherty, Global trends and European emissions of tetrafluoromethane (CF_4), hexafluoroethane (C_2F_6) and octafluoropropane (C_3F_8), ***Atmos. Chem. Phys.***, ***21***, 2149–2164, 2021 doi:10.5194/acp-21-2149-2021, 2021.

Schultz, M.G., T. Diehl, G.P. Brasseur, and W. Zittel, Air pollution and climate-forcing impacts of a global hydrogen economy, ***Science***, ***302*** (5645), 624–627, doi:10.1126/science.1089527, 2003.

Shechner, M., A. Guenther, R. Rhew, A. Wishkerman, Q. Li, D. Blake, G. Lerner, and E. Tas, Emission of volatile halogenated organic compounds over various Dead Sea landscapes, ***Atmos. Chem. Phys.***, ***19***, 7667–7690, doi:10.5194/acp-19-7667-2019, 2019.

Sherwen, T., J.A. Schmidt, M.J. Evans, L.J. Carpenter K. Großmann, S.D. Eastham, D.J. Jacob, B. Dix, T.K. Koenig, R. Sinreich, I. Ortega, R. Volkamer, A. Saiz-Lopez, C. Prados-Roman, A.S. Mahajan, and C. Ordóñez, Global impacts of tropospheric halogens (Cl, Br, I) on oxidants and composition in GEOS-Chem, ***Atmos. Chem. Phys.***, ***16*** (18), 12,239–12,271, doi:10.5194/acp-16-12239-2016, 2016.

Sherwen T., R.J. Chance, L. Tinel, D. Ellis, M.J. Evans, and L.J. Carpenter, A machine learning-based global sea-surface iodide distribution, ***Earth Syst. Sci. Data, 11*** (3), 1239–1262, doi:10.5194/essd-11-1239-2019, 2019.

Shine, K.P., and G. Myhre, The spectral nature of stratospheric temperature adjustment and its application to halocarbon radiative forcing, ***J. Adv. Model. Earth Syst.***, ***12*** (3), e2019MS001951, doi:10.1029/2019MS001951, 2020.

Simmonds, P.G., M. Rigby, A. McCulloch, S. O'Doherty, D. Young, J. Mühle, P.B. Krummel, P. Steele, P.J. Fraser, A.J. Manning, R.F. Weiss, P.K. Salameh, C.M. Harth, R.H.J. Wang, and R.G. Prinn, Changing trends and emissions of hydrochlorofluorocarbons (HCFCs) and their hydrofluorocarbon (HFCs) replacements, ***Atmos. Chem. Phys.***, ***17*** (7), 4641–4655, doi:10.5194/acp-17-4641-2017, 2017.

Simmonds, P.G., M. Rigby, A.J. Manning, S. Park, K.M. Stanley, A. McCulloch, S. Henne, F. Graziosi, M. Maione, J. Arduini, S. Reimann, M.K. Vollmer, J. Mühle, S. O'Doherty, D. Young, P.B. Krummel, P.J. Fraser, R.F. Weiss, P.K. Salameh, C.M. Harth, M.-K. Park, H. Park, T. Arnold, C. Rennick, L.P. Steele, B. Mitrevski, R.H.J. Wang, and R.G. Prinn, The increasing atmospheric burden of the greenhouse gas sulfur hexafluoride (SF_6), ***Atmos. Chem. Phys.***, ***20*** (12), 7271–7290, doi:10.5194/acp-20-7271-2020, 2020.

Simpson, I.J., N.J. Blake, D.R. Blake, S. Meinardi, M.P.S. Andersen, and F.S. Rowland, Strong evidence for negligible methyl chloroform (CH_3CCl_3) emissions from biomass burning, ***Geophys. Res. Lett.***, ***34*** (10), doi:10.1029/2007GL029383, 2007.

Sinnhuber, B.-M., and I. Folkins, Estimating the contribution of bromoform to stratospheric bromine and its relation to dehydration in the tropical tropopause layer, ***Atmos. Chem. Phys.***, ***6*** (12), 4755–4761, doi:10.5194/acp-6-4755-2006, 2006.

Sinnhuber, B.-M., N. Sheode, M. Sinnhuber, M.P. Chipperfield, and W. Feng, The contribution of anthropogenic bromine emissions to past stratospheric ozone trends: A modelling study, ***Atmos. Chem. Phys.***, 9, 2863–2871, doi:10.5194/acp-9-2863-2009, 2009.

Smith, C., Z.R.J. Nicholls, K. Armour, W. Collins, P. Forster, M. Meinshausen, M.D. Palmer, and M. Watanabe, The Earth's Energy Budget, Climate Feedbacks, and Climate Sensitivity Supplementary Material, Chapter 7, in ***Climate Change 2021: The Physical Science Basis, Contribution of Working Group I to the Sixth Assessment Report of the Intergovernmental Panel on Climate Change*** edited by V. Masson-Delmotte, P. Zhai, A. Pirani, S.L. Connors, C. Péan, S. Berger, N. Caud, Y. Chen, L. Goldfarb, M.I. Gomis, M. Huang, K. Leitzell, E. Lonnoy, J.B.R. Matthews, T.K. Maycock, T. Waterfield, O. Yelekçi, R. Yu, and B. Zhou, Cambridge University Press, Cambridge, United Kingdom and New York, NY, USA, [available at: https://www.ipcc.ch/], 2021.

SPARC (Stratosphere-troposphere Processes And their Role in Climate), ***SPARC Report on the Lifetimes of Stratospheric Ozone-Depleting Substances, Their Replacements, and Related Species***, edited by M.K.W. Ko, P.A. Newman, S. Reimann, and S.E. Strahan, SPARC Report No. 6, WCRP-15/2013, 255 pp., [available at: https://www.sparc-climate.org/fileadmin/customer/6_Publications/SPARC_reports_PDF/6_SPARC_LifetimeReport_Web.pdf], 2013.

SPARC (Stratosphere-troposphere Processes And their Role in Climate), ***SPARC Report on the Mystery of Carbon Tetrachloride***, edited by Q. Liang, P.A. Newman, and S. Reimann, SPARC Report No. 7, WCRP-13/2016, 67 pp., [available at: https://www.wcrp-climate.org/WCRP-publications/2016/SPARC_Report7_2016.pdf], 2016.

Stanley, K.M., D. Say, J. Mühle, C.M. Harth, P.B. Krummel, D. Young, S.J. O'Doherty, P.K. Salameh, P.G. Simmonds, R.F. Weiss, R.G. Prinn, P.J. Fraser, and M. Rigby, Increase in global emissions of HFC-23 despite near-total expected reductions, ***Nat. Commun.***, ***11*** (397), doi:10.1038/s41467-019-13899-4, 2020.

Steffen, J., P.F. Bernath, and C.D. Boone, Trends in halogen-containing molecules measured by the Atmospheric Chemistry Experiment (ACE) satellite, ***J. Quant. Spectrosc. Radiat. Transf.***, ***238***, 106619, doi:10.1016/j.jqsrt.2019.106619, 2019.

Strahan, S.E., D. Smale, A.R. Douglass, T. Blumenstock, J.W. Hannigan, F. Hase, N.B. Jones, E. Mahieu, J. Notholt, L.D. Oman, I. Ortega, M. Palm, M. Prignon, J. Robinson, M. Schneider, R. Sussmann, and V.A. Velazco, Observed hemispheric asymmetry in stratospheric transport trends from 1994 to 2018, ***Geophys. Res. Lett.***, ***47*** (17), e2020GL088567, doi:10.1029/2020GL088567, 2020.

Sturges, W.T., D.E. Oram, J.C. Laube, C.E. Reeves, M.J. Newland, C. Hogan, P. Martinerie, E. Witrant, C.A.M. Brenninkmeijer, T.J. Schuck, and P.J. Fraser, Emissions halted of the potent greenhouse gas SF_5CF_3, ***Atmos. Chem. Phys.***, ***12*** (8), 3653–3658, doi:10.5194/acp-12-3653-2012, 2012.

Suntharalingam, P., E. Buitenhuis, L.J. Carpenter, J.H. Butler, M.J. Messias, S.J. Andrews, and S.C. Hackenberg, Evaluating oceanic uptake of atmospheric CCl_4: A combined analysis of model simulations and observations, ***Geophys. Res. Lett.***, ***46*** (1), 472–482, doi:10.1029/2018GL080612, 2019.

Tegtmeier, S., E. Atlas, B. Quack, F. Ziska, and K. Krüger, Variability and past long-term changes of brominated very short-lived substances at the tropical tropopause, Atmos. Chem. Phys., 20(11), 7103–7123, doi:10.5194/acp-20-7103-2020, 2020.

Tegtmeier, S., F. Ziska, I. Pisso, B. Quack, G. J. M. Velders, X. Yang, and K. Krüger, Oceanic bromoform emissions weighted by their ozone depletion potential, Atmos. Chem. Phys., 15, 13647–13663, doi:10.5194/acp-15-13647-2015, 2015.

Tegtmeier, S., K. Kruger, B. Quack, E. Atlas, D. R. Blake, H. Boenisch, A. Engel, H. Hepach, R. Hossaini, M. A. Navarro, S. Raimund, S. Sala, Q. Shi, and F. Ziska, The contribution of oceanic methyl iodide to stratospheric iodine, Atmos. Chem. Phys., 13(23), 11869–11886, doi:10.5194/acp-13-11869-2013, 2013.

Tegtmeier, S., K. Kruger, B. Quack, E. L. Atlas, I. Pisso, A. Stohl, and X. Yang, Emission and transport of bromocarbons: From the West Pacific Ocean into the stratosphere, Atmos. Chem. Phys., 12(22), 10633–10648, doi:10.5194/acp-12-10633-2012, 2012.

Thompson, R.L., L. Lassaletta, P.K. Patra, C. Wilson, K.C. Wells, A. Gressent, E.N. Koffi, M.P. Chipperfield, W. Winiwarter, E.A. Davidson, H. Tian, and J.G. Canadell, Acceleration of global N_2O emissions seen from two decades of atmospheric inversion, ***Nat. Clim. Change***, ***9***, 993–998, doi:10.1038/s41558-019-0613-7, 2019.

Tian, H., R. Xu, J.G. Canadell, R.L. Thompson, W. Winiwarter, P. Suntharalingam, E.A. Davidson, P. Ciais, R.B. Jackson, G. Janssens-Maenhout, M.J. Prather, P. Regnier, N. Pan, S. Pan, G.P. Peters, H. Shi, F.N. Tubiello, S. Zaehle, F. Zhou, A. Arneth, G. Battaglia, S. Berthet, L. Bopp, A.F. Bouwman, E.T. Buitenhuis, J. Chang, M.P. Chipperfield, S.R.S. Dangal, E. Dlugokencky, J.W. Elkins, B.D. Eyre, B. Fu, B. Hall, A. Ito, F. Joos, P.B. Krummel, A. Landolfi, G.G. Laruelle, R. Lauerwald, W. Li, S. Lienert, T. Maavara, M. MacLeod, D.B. Millet, S. Olin, P.K. Patra, R.G. Prin, P.A. Raymond, D.J. Ruiz, G.R. van der Werf, N. Vuichard, J. Wang, R.F. Weiss, K.C. Wells, C. Wilson, J. Yang, and Y. Yao, A comprehensive quantification of global nitrous oxide sources and sinks, ***Nature***, ***586***, 248–256, doi:10.1038/s41586-020-2780-0, 2020.

Tinel, L., T.J. Adams, L.D. J. Hollis, A.J.M. Bridger, R.J. Chance, M.W. Ward, S.M. Ball, and L.J. Carpenter, Influence of the sea surface microlayer on oceanic iodine emissions, ***Environ. Sci. Technol.***, ***54*** (20), 13,228–13,237, doi: 10.1021/acs.est.0c02736, 2020.

Tromp, T.K., R.-L. Shia, M. Allen, J.M. Eiler, and Y.L. Yung, Potential environmental impact of a hydrogen economy on the stratosphere, ***Science***, ***300***, 1740–1722, doi:10.1126/science.1085169, 2003.

Trudinger, C.M., D.M. Etheridge, G.A. Sturrock, P.J. Fraser, P.B. Krummel, and A. McCulloch, Atmospheric histories of halocarbons from analysis of Antarctic firn air: Methyl bromide, methyl chloride, chloroform, and dichloromethane, ***J. Geophys. Res.***, ***109***, D22310, doi:10.1029/2004JD004932, 2004.

Trudinger, C.M., P.J. Fraser, D.M. Etheridge, W.T. Sturges, M.K. Vollmer, M. Rigby, P. Martinerie, J. Mühle, D.R. Worton, P.B. Krummel, L.P. Steele, B.R. Miller, J. Laube, F.S. Mani, P.J. Rayner, C.M. Harth, E. Witrant, T. Blunier, J. Schwander, S. O'Doherty, and M. Battle, Atmospheric abundance and global emissions of perfluorocarbons CF_4, C_2F_6 and C_3F_8 since 1800 inferred from ice core, firn, air archive and ***in situ*** measurements, ***Atmos. Chem. Phys.***, ***16*** (18), 11,733–11,754, doi:10.5194/acp-16-11733-2016, 2016.

Umezawa, T., A.K. Baker, D. Oram, C. Sauvage, D. O'Sullivan, A. Rauthe-Schöch, S.A. Montzka, A. Zahn, and C.A.M. Brenninkmeijer, Methyl chloride in the upper troposphere observed by the CARIBIC passenger aircraft observatory: Large-scale distributions and Asian summer monsoon outflow, ***J. Geophys. Res. Atmos.***, ***119*** (9), 5542–5558, doi:10.1002/2013JD021396, 2014.

Umezawa, T., A.K. Baker, C.A.M. Brenninkmeijer, A. Zahn, D.E. Oram, and P.F.J. van Velthoven, Methyl chloride as a tracer of tropical tropospheric air in the lowermost stratosphere inferred from IAGOS-CARIBIC passenger aircraft measurements, ***J. Geophys. Res. Atmos.***, ***120*** (23), doi:10.1002/2015JD023729, 2015.

UNEP (United Nations Environment Programme), Report of the Methyl Bromide Technical Options Committee, United Nations Environment Programme, Ozone Secretariat, Nairobi, Kenya, 2006.

UNEP (United Nations Environment Programme), data from Ozone Secretariat Country Data Centre, United Nations Environment Programme, Nairobi, Kenya [available at: https://ozone.unep.org/countries/data-table], 2022.

U.S. EPA (U.S. Environmental Protection Agency), ***Inventory of U.S. Greenhouse Gas Emissions and Sinks: 1990-2019***, U.S. Environmental Protection Agency, [available at: https://www.epa.gov/ghgemissions/inventory-us-greenhouse-gas-emissions-and-sinks-1990-2019], 2021.

Vogel, B., T. Feck, and J.-U. Grooß, Impact of stratospheric water vapor enhancements caused by CH_4 and H_2O increase on polar ozone loss, ***J. Geophys. Res. Atmos.***, ***116*** (D5), doi:10.1029/2010JD014234, 2011.

Vollmer, M.K., B.R. Miller, M. Rigby, S. Reimann, J. Mühle, P.B. Krummel, S. O'Doherty, J. Kim, T.S. Rhee, R.F. Weiss, P.J. Fraser, P.G. Simmonds, P.K. Salameh, C.M. Harth, R.H.J. Wang, L.P. Steele, D. Young, C.R. Lunder, O. Hermansen, D. Ivy, T. Arnold, N. Schmidbauer, K.-R. Kim, B.R. Greally, M. Hill, M. Leist, A. Wenger, and R.G. Prinn, Atmospheric histories and global emissions of the anthropogenic hydrofluorocarbons HFC-365mfc, HFC-245fa, HFC-227ea, and HFC-236fa, ***J. Geophys. Res.***, ***116*** (D8), D08304, doi:10.1029/2010JD015309, 2011.

Vollmer, M.K., S. Reimann, M. Hill, and D. Brunner, First observations of the fourth generation synthetic halocarbons HFC-1234yf, HFC-1234ze(E), and HCFC-1233zd(E) in the atmosphere, ***Environ. Sci. Technol.***, ***49*** (5), 2703–2708, doi:10.1021/es505123x, 2015a.

Vollmer, M.K., M. Rigby, J.C. Laube, S. Henne, T.S. Rhee, L.J. Gooch, A. Wenger, D. Young, L.P. Steele, R.L. Langenfelds, C.A.M. Brenninkmeijer, J.L. Wang, C.F. Ou-Yang, S.A. Wyss, M. Hill, D.E. Oram, P.B. Krummel, F. Schoenenberger, C. Zellweger, P.J. Fraser, W.T. Sturges, S. O'Doherty, and S. Reimann, Abrupt reversal in emissions and atmospheric abundance of HCFC-133a (C_3FCH_2Cl), ***Geophys. Res. Lett.***, ***42*** (20), 8702–8710, doi:10.1002/2015GL065846, 2015b.

Vollmer, M.K., T.S. Rhee, M. Rigby, D. Hofstetter, M. Hill, F. Schoenenberger, and S. Reimann, Modern inhalation anesthetics: Potent greenhouse gases in the global atmosphere, ***Geophys. Res. Lett.***, ***42*** (5), 1606–1611, doi:10.1002/2014GL062785, 2015c.

Vollmer, M.K., J. Mühle, C.M. Trudinger, M. Rigby, S.A. Montzka, C.M. Harth, B.R. Miller, S. Henne, P.B. Krummel, B.D. Hall, D. Young, J. Kim, J. Arduini, A. Wenger, B. Yao., S. Reimann., S. O'Doherty, M. Maione, D.M. Etheridge, S. Li, D.P. Verdonik, S. Park, G.S. Dutton, L.P. Steele, C.P. Lunder, T.S. Rhee, O. Hermansen, N. Schmidbauer , R.H.J. Wang, M. Hill, P.K. Salameh, R.L. Langenfelds, Z.L.X. Zhou, T. Blunier, J. Schwander, J.W. Elkins, J.H. Butler, P.G. Simmonds, R.F. Weiss, R.G. Prinn, and P.J. Fraser, Atmospheric histories and global emissions of halons H-1211 ($CBrClF_2$), H-1301 ($CBrF_3$), and H-2402 ($CBrF_2CBrF_2$), ***J. Geophys. Res. Atmos.***, ***121***, 3663–3686, doi:10.1002/2015JD0024488, 2016.

Vollmer, M.K., D. Young, C.M. Trudinger, J. Mühle, S. Henne, M. Rigby, S. Park, S. Li, M. Guillevic, B. Mitrevski, C.M. Harth, B.R. Miller, S. Reimann, B. Yao, L.P. Steele, S.A. Wyss, C.R. Lunder, J. Arduini, A. McCulloch, S. Wu, T.S. Rhee, R.H.J. Wang, P.K. Salameh, O. Hermansen, M. Hill, R.L. Langenfelds, D. Ivy, S. O'Doherty, P.B. Krummel, M. Maione, D.M. Etheridge, L. Zhou, P.J. Fraser, R.G. Prinn, R.F. Weiss, and P.G. Simmonds, Atmospheric histories and emissions of chlorofluorocarbons CFC-13 ($CClF_3$), ΣCFC-114 ($C_2Cl_2F_4$), and CFC-115 (C_2ClF_5), ***Atmos. Chem. Phys.***, ***18*** (2), 979–1002, doi:10.5194/acp-18-979-2018, 2018.

Vollmer, M.K., F. Bernard, B. Mitrevski, L.P. Steele, C.M. Trudinger, S. Reimann, R.L. Langenfelds, P.B. Krummel, P.J. Fraser, D.M. Etheridge, M.A.J. Curran, and J.B. Burkholder, Abundances, emissions, and loss processes of the long-lived and potent greenhouse gas octafluorooxolane (octafluorotetrahydrofuran, c-C_4F_8O) in the atmosphere, ***Atmos. Chem. Phys.***, ***19*** (6), 3481–3492, doi:10.5194/acp-19-3481-2019, 2019.

Vollmer, M.K., J. Mühle, S. Henne, D. Young, M. Rigby, B. Mitrevski, S. Park, C.R. Lunder, T.S. Rhee, C.M. Harth, M. Hill, R.L. Langenfelds, M. Guillevic, P.M. Schlauri, O. Hermansen, J. Arduini, R.H.J. Wang, P.K. Salameh, M. Maione, P.B. Krummel, S. Reimann, S. O'Doherty, P.G. Simmonds, P.J. Fraser, R.G. Prinn, R.F. Weiss, and L.P. Steele, Unexpected nascent atmospheric emissions of three ozone-depleting hydrochlorofluorocarbons, ***Proc. Natl. Acad. Sci.***, ***118*** (5), doi:10.1073/pnas.2010914118, 2021.

Wadley, M.R., D.P. Stevens, T.D. Jickells, C. Hughes, R. Chance, H. Hepach, L. Tinel, and L.J. Carpenter, A global model for iodine speciation in the upper ocean, ***Global Biogeochem. Cycles***, ***34*** (9), doi:10.1029/2019GB006467, 2020.

Waggoner, M., H.D. Ohr, C. Adams, J.J. Sims, and D. Gonzalez, Methyl iodide: an alternative to methyl bromide for insectary fumigation, ***J. Appl. Entomol.***, ***124*** (2), 113–117, doi:10.1046/j.1439-0418.2000.00437.x, 2000.

Wahner, A., A.R. Ravishankara, S.P. Sander, and R.R. Friedl, Absorption cross section of BrO between 312 and 385 nm AT 298 and 223 K, ***Chem. Phys. Lett.***, ***152***, 507–510, doi:10.1016/0009-2614(88)80450-0, 1988.

Wang, Z.Y., H.H. Yan, X.K. Fang, L.Y. Gao, Z.H. Zhai, J.X. Hu, B.Y. Zhang, and J.B. Zhang, Past, present, and future emissions of HCFC-141b in China, ***Atmos. Environ.***, ***109***, 228–233, doi:10.1016/j. atmosenv.2015.03.019, 2015.

Wang, S., D. Kinnison, S.A. Montzka, E.C. Apel, R.S. Hornbrook, A.J. Hills, D.R. Blake, B. Barletta, S. Meinardi, C. Sweeney, F. Moore, M. Long, A. Saiz-Lopez, R.P. Fernandez, S. Tilmes, L.K. Emmons, and J.-F. Lamarque, Ocean biogeochemistry control on the marine emissions of brominated very short-lived ozone-depleting substances: a machine-learning approach, ***J. Geophys. Res. Atmos.***, ***124*** (22), 12,319–12,339, doi:10.1029/2019JD031288, 2019.

Wang, P., J.R. Scott, S. Solomon, J. Marshall, A.R. Babbin, M. Lickley, D.W.J. Thompson, T. DeVries, Q. Liang, and R.G. Prinn, On the effects of the ocean on atmospheric CFC-11 lifetimes and emissions, ***Proc. Natl. Acad. Sci.***, ***118*** (12), doi:10.1073/pnas.2021528118, 2021.

Wales, P.A., R.J. Salawitch, J.M. Nicely, D.C. Anderson, T.P. Canty, S. Baidar, B. Dix, T.K. Koenig, R. Volkamer, D. Chen, L.G. Huey, D.J. Tanner, C.A. Cuevas, R.P. Fernandez, D.E. Kinnison, J.-F Lamarque, A. Saiz-Lopez, E.L. Atlas, S.R. Hall, M.A. Navarro, L.L. Pan, S.M. Schauffler, M. Stell, S. Tilmes, K. Ullmann, A.J. Weinheimer, H. Akiyoshi, M.P. Chipperfield, M. Deushi, S.S. Dhomse, W. Feng, P. Graf, R. Hossaini, P. Jöckel, E. Mancini, M. Michou, O. Morgenstern, L.D. Oman, G. Pitari, D.A. Plummer, L.E. Revell, E. Rozanov, D. Saint-Martin, R. Schofield, A. Stenke, K.A. Stone, D. Visioni, Y. Yamashita, and G. Zeng, Stratospheric injection of brominated very short-lived substances: Aircraft observations in the Western Pacific and representation in global models, ***J. Geophys. Res. Atmos.***, ***123*** (10), 5690–5719, doi:10.1029/2017JD027978, 2018.

Whelan, M.E., S.T. Lennartz, T.E. Gimeno, R. Wehr, G. Wohlfahrt, Y. Wang, L.M.J. Kooijmans, T.W. Hilton, S. Belviso, P. Peylin, R. Commane, W. Sun, H. Chen, L. Kuai, I. Mammarella, K. Maseyk, M. Berkelhammer, K.-F. Li, D. Yakir, A. Zumkehr, Y. Katayama, J. Ogée, F.M. Spielmann, F. Kitz, B. Rastogi, J. Kesselmeier, J. Marshall, K.-M. Erkkilä, L. Wingate, L.K. Meredith, W. He, R. Bunk, T. Launois, T. Vesala, J.A. Schmidt, C.G. Fichot, U. Seibt, S. Saleska, E.S. Saltzman, S.A. Montzka, J.A. Berry, and J.E. Campbell, Reviews and syntheses: Carbonyl sulfide as a multi-scale tracer for carbon and water cycles, ***Biogeosciences***, ***15***, 3625–3657, doi:10.5194/bg-15-3625-2018, 2018.

Weiss, R.F., A.R. Ravishankara, and P.A. Newman, Huge gaps in detection networks plague emissions monitoring, ***Nature***, ***595*** (7868), 491–493, doi:10.1038/d41586-021-01967-z, 2021.

Werner, B., J. Stutz, M. Spolaor, L. Scalone, R. Raecke, J. Festa, S.F. Colosimo, R. Cheung, C. Tsai, R. Hossaini, M.P. Chipperfield, G.S. Taverna, W. Feng, J.W. Elkins, D.W. Fahey, R.-S. Gao, E.J. Hintsa, T.D. Thornberry, F.L. Moore, M.A. Navarro, E. Atlas, B.C. Daube, J. Pittman, S. Wofsy, and K. Pfeilsticker, Probing the subtropical lowermost stratosphere and the tropical upper troposphere and tropopause layer for inorganic bromine, ***Atmos. Chem. Phys.***, ***17*** (2), 1161–1186, doi:10.5194/acp-17-1161-2017, 2017.

Wilmouth, D.M., T.F. Hanisco, N.M. Donahue, and J.G. Anderson, Fourier transform ultraviolet spectroscopy of the A 2Π3/2← X 2Π3/2 transition of BrO, ***J. Phys. Chem. A***, ***103*** (45), 8935–8945, doi:10.1021/jp991651o, 1999.

WMO (World Meteorological Organization), ***Scientific Assessment of Ozone Depletion: 2018***, Global Ozone Research and Monitoring Project–Report No. 58, 588 pp., Geneva, Switzerland, 2018.

Wofsy, S.C., HIAPER Pole-to-Pole Observations (HIPPO): fine-grained, global-scale measurements of climatically important atmospheric gases and aerosols, ***Philos. Trans. R. Soc. A***, ***369*** (1943), 2073–2086, doi:10.1098/rsta.2010.0313, 2011.

Worton, D.R., W.T. Sturges, J. Schwander, R. Mulvaney, J.-M. Barnola, and J. Chappellaz, 20th century trends and budget implications of chloroform and related tri-and dihalomethanes inferred from firn air, ***Atmos. Chem. Phys.***, ***6*** (10), 2847–2863, doi:10.5194/acp-6-2847-2006, 2006.

Wuebbles, D.J., Ozone Depletion and Related Topics | Ozone Depletion Potentials, ***Encycl. Atmos. Sci. (2nd Ed.)***, 364–369, doi:10.1016/B978-0-12-382225-3.00293-0, 2015.

Yang, M., F. Yang, H. Li, T. Li, F. Cao, X. Nie, J. Zhen, P. Li, and Y. Wang, CFCs measurements at high altitudes in northern China during 2017–2018: concentrations and potential emission source regions, ***Sci. Tot. Environ.***, ***754*** (17), 142290, doi:10.1016/j.scitotenv.2020.142290, 2021.

Yi, L., J. Wu, M. An, W. Xu, X. Fang, B. Yao, Y. Li, D. Gao, X. Zhao, and J. Hu, The atmospheric concentrations and emissions of major halocarbons in China during 2009–2019, ***Environ. Pollut.***, ***284***, 117190, doi:10.1016/j.envpol.2021.117190, 2021.

Yokouchi, Y., S. Taguchi, T. Saito, Y. Tohjima, H. Tanimoto, and H. Mukai, High frequency measurements of HFCs at a remote site in east Asia and their implications for Chinese emissions, ***Geophys. Res. Lett.***, ***33*** (21), doi:10.1029/2006GL026403, 2006.

Yokouchi, Y., Y. Nojiri, D. Toom-Sauntry, P. Fraser, Y. Inuzuka, H. Tanimoto, H. Nara, R. Murakami, and H. Mukai, Long-term variation of atmospheric methyl iodide and its link to global environmental change, ***Geophys. Res. Lett.***, ***39*** (23), doi:10.1029/2012GL053695, 2012.

Yu, D., B. Yao, W. Lin, M.K. Vollmer, B. Ge, G. Zhang, Y. Li, H. Xu, S. O'Doherty, L. Chen, and S. Reimann, Atmospheric CH_3CCl_3 observations in China: Historical trends and implications, ***Atmos. Res.***, 231, 104658, doi:10.1016/j.atmosres.2019.104658, 2020.

Yvon-Lewis, S.A., and J.H. Butler, Effect of oceanic uptake on atmospheric lifetimes of selected trace gases, ***J. Geophys. Res.***, ***107*** (D20), 4414, doi:10.1029/2001JD001267, 2002.

Yvon-Lewis, S.A., E.S. Saltzman, and S.A. Montzka, Recent trends in atmospheric methyl bromide: analysis of post-Montreal Protocol variability, ***Atmos. Chem. Phys.***, ***9***, 5963–5974, doi:10.5194/acp-9-5963-2009, 2009.

Zander R., E. Mahieu, P. Demoulin, P. Duchatelet, G. Roland, C. Servais, M. De Mazière, S. Reimann, and C.P. Rinsland, Our changing atmosphere: evidence based on long-term infrared solar observations at the Jungfraujoch since 1950, ***Sci. Tot. Environ.***, ***391*** (1-2), 184–195, doi:10.1016/j.scitotenv.2007.10.018, 2008.

Zeng, L., J. Dang, H. Guo, X. Lyu, I.J. Simpson, S. Meinardi, Y. Wang, L. Zhang, and D.R. Blake, Long-term temporal variations and source changes of halocarbons in the Greater Pearl River Delta region, China, ***Atmos. Environ.***, ***234*** (40), 117550, doi:10.1016/j.atmosenv.2020.117550, 2020.

Zhang, J., D.J. Wuebbles, D.E. Kinnison, and A. Saiz-Lopez, Revising the ozone depletion potentials metric for short-lived chemicals such as CF_3I and CH_3I, ***J. Geophys. Res. Atmos.***, ***125*** (9), e2020JD032414, doi:10.1029/2020JD032414, 2020.

Zhang, W., Y. Jiao, R. Zhu, and R.C. Rhew, Methyl chloride and methyl bromide production and consumption in coastal Antarctic tundra soils subject to sea animal activities, ***Environ. Sci. Technol.***, ***54***, 13354–13363, 2020.

Zhang, W., Y. Jiao, R. Zhu, R.C. Rhew, B. Sun, and H. Dai, Chloroform ($CHCl_3$) emissions from coastal Antarctic tundra, ***Geophys. Res. Lett.***, ***48*** (18), e2021GL093811, doi:10.1029/2021GL093811, 2021.

Zhao, X., X. Hou, and W. Zhou, Atmospheric iodine (127I and 129I) record in spruce tree rings in the northeast Qinghai–Tibet Plateau, ***Environ. Sci. Technol.***, ***53*** (15), 8706–8714, doi:10.1021/acs.est.9b01160, 2019.

Ziska, F., B. Quack, K. Abrahamsson, S.D. Archer, E. Atlas, T. Bell, J.H. Butler, L.J. Carpenter, C.E. Jones, N.R.P. Harris, H. Hepach, K.G. Heumann, C. Hughes, J. Kuss, K. Kruger, P. Liss, R.M. Moore, A. Orlikowska, S. Raimund, C.E. Reeves, W. Reifenhauser, A.D. Robinson, C. Schall, T. Tanhua, S. Tegtmeier, S. Turner, L. Wang, D. Wallace, J. Williams, H. Yamamoto, S. Yvon-Lewis, and Y. Yokouchi, Global sea-to-air flux climatology for bromoform, dibromomethane and methyl iodide, ***Atmos. Chem. Phys.***, ***13*** (17), 8915–8934, doi:10.5194/acp-13-8915-2013, 2013.

Zgonnik, V., The occurrence and geoscience of natural hydrogen: A comprehensive review, ***Earth Sci. Rev.***, ***203***, 103140, doi:10.1016/j.earscirev.2020.103140, 2020.